Naval Information Warfare Center PACIFIC

Technical Report 3218
November 2020

Analysis of Collaborative Beamforming for Circularly Bound Random Antenna Array Distributions

Kristopher R. Buchanan
Sara Wheeland
Carlos Flores-Molina
Timi Adeyemi
Drew Overturf
Oren Sternberg
Michelle Rodriguez
Vincent P. Acevedo
Gregory H. Huff

NIWC Pacific

Naval Information Warfare Center Pacific (NIWC Pacific)
San Diego, CA 92152-5001

This page is intentionally blank.

Technical Report 3218
November 2020

Analysis and Discussion of Circularly Bound Random Antenna Array Distributions

Kristopher R. Buchanan
Sara Wheeland
Carlos Flores-Molina
Timi Adeyemi
Drew Overturf
Oren Sternberg
Michelle Rodriguez
Vincent P. Acevedo
Gregory H. Huff

NIWC Pacific

Administrative Notes:
This report was approved through the Release of Scientific and Technical Information (RSTI) process in October 2019 and formally published in the Defense Technical Information Center (DTIC) in November 2020.

NIWC Pacific
San Diego, CA 92152-5001

NIWC Pacific
San Diego, California 92152-5001

A. D. Gainer, CAPT, USN
Commanding Officer

W. R. Bonwit
Executive Director

ADMINISTRATIVE INFORMATION

This report was prepared by the Electromagnetics Technology Branch of the Electromagnetics and Advanced Technology Division, Naval Information Warfare Center Pacific (NIWC Pacific). The NIWC Pacific Naval Innovative Science and Engineering (NISE) Program provided funding for this Basic Applied Research project.

Released by
M. Osburn, Branch Head
Electromagnetics Technology Branch

Under authority of
J. McGee, Division Head
Electromagnetics and Advanced Technology Division

Edited by:
Robert J. Price

EXECUTIVE SUMMARY

This report provides a theoretical feasibility study to investigate the performance of circular antenna arrays. The radiation performance of circularly bound random arrays with various distributions is analyzed statistically to identify deterministic, transitional, and random behavior regions. Isotropic radiators are preferred in this analysis because they provide relevant information on the fundamental beamforming behavior and can be applied to provide practical estimates and ideal limitations on the maximum peaking sidelobe located in the stochastically described 3 dB sidelobe region since this regime tends to behave non-deterministically. The mathematical process required for this analysis includes a statistical formulation of the array factor, including the mean, or expected value, and the variance. Rigorous analysis from prior works on random arrays provides the framework for this work and develops into accurate estimates of the maximum peaking sidelobe behavior in a volumetric scan region. Numerical results are included to illustrate scanning from zenith to meridian elevation angles to evaluate the theory and compare the behavior of both planar circular and volumetric spherical arrays.

This page is intentionally blank.

CONTENTS

EXECUTIVE SUMMARY ..... **v**

1. INTRODUCTION **1**

2. STATISTICAL PROBLEM FORMULATION AND ANALYSIS OF A CIRCULARLY DISTRIBUTED RANDOM ANTENNA ARRAY **3**

2.1 FORMULATION OF THE EXACT ARRAY FACTOR 3

2.2 PROBABILITY AND CUMULATIVE DENSITY FUNCTIONS OF A CIRCULARLY DISTRIBUTED ELEMENT POPULATION 4

2.3 PROBABILITY MOMENTS OF THE CIRCULARLY DISTRIBUTED ELEMENT POPULATION 5

2.4 FORMULATION OF THE ARRAY FACTOR 5

2.5 FORMULATION OF THE MEAN VALUED ARRAY FACTOR 6

2.6 FORMULATION OF THE MEAN VALUED RADIATION PATTERN 7

2.6.1 Mean pattern 7

2.6.2 Mean pattern in complex psi space 14

2.6.3 Mean pattern in angular space 15

2.6.4 Comparison to prior work [15] 18

2.7 SIMPLIFICATION ZENITH AND MERIDIAN SCAN BEHAVIOR ERRORS 18

2.8 ANALYSIS OF RADIATION FROM SUBARRAYS 19

2.9 DIRECTIVITY IN PSI SPACE 27

3. STATISTICAL ANALYSIS **29**

3.1.1 Explanation of the Physical Process 29

3.2 PROBABILITY MOMENTS OF THE MEAN VALUED ARRAY FACTOR AND MEAN VALUED RADIATION PATTERN 29

3.2.1 Array Factor Moments 29

3.2.2 Power Pattern Moments 32

3.3 ARRAY FACTOR PROBABILITY AND JOINT DENSITY FUNCTIONS 33

3.3.1 Joint Distribution Function of the Array Factor Amplitude and Phase 33

3.3.2 Probability Distribution Function of the Array Factor Amplitude 33

4. PEAK SIDELOBE ESTIMATOR B **37**

4.1 3DB SIDELOBE REGION 37

4.2 AUTO-COVARIANCE 37

4.3 CROSS-COVARIANCE, JOINT MEAN AND PATTERN COVARIANCE 38

4.4 PDF OF THE PROBABILITY NO SIDELOBE EXCEEDS THE THRESHOLD 38

4.5 PDF, MEAN AND VARIANCE OF B (THRESHOLD POWER LEVEL TO THE THEORETICAL SIDELOBE LEVEL) 39

4.6 PEAK SIDELOBE ESTIMATOR B_P 39

4.7 MINIMUM NUMBER OF ELEMENTS 40

4.8 MEAN VALUE OF THE PEAKING SIDELOBE IN THE 3DB SIDELOBE REGION IN ANGULAR SPACE 40
4.9 MEAN STATISTICS ANGULAR SPACE 40
4.10 NON-ISOTROPIC ELEMENTS 43
4.11 WIDEBAND SIGNALS 44
4.12 PERIODIC VS. CONFORMAL, PLANAR AND VOLUMETRIC ARRAY NUMBER OF ELEMENT COMPARISON 45
5. MUTUAL COUPLING 47
5.1 GRAPH THEORY 47
6. ORTHOGONAL SETS AND AMPLITUDE DISTRIBUTIONS 49
6.1 N-SPHERE AMPLITUDE TAPERS USING THE JACOBI AND GEGENBAUER POLYNOMIALS (HYPERGEOMETRIC POLYNOMIALS) 49
6.2 HARDY DISTRIBUTION 50
6.3 BABINET'S PRINCIPLE 51
6.3.1 Green's Function of an Infinite Planar Screen 51
6.3.2 Radiation from a Finite Source 52
6.4 COMPLEMENTARY SCREENS 53
6.5 BABINET'S PRINCIPLE USING COMPLEMENTARY TOPOLOGY 53
7. FREQUENCY-RANGE BEAMSTEERING 55
8. MOBILE DISTRIBUTION (RANGE-DOPPLER) 57
8.1 STATIONARY DISTRIBUTION 57
8.2 MOBILE DISTRIBUTION 57
8.2.1 First-order phase variations 57
8.3 STOP AND HOP APPROXIMATION 58
8.4 HIGHER ORDER PHASE VARIATIONS 58
8.4.1 Expansion of the range-velocity kernel 59
9. RADAR CROSS SECTION 61
9.1 EXPERIMENTAL RESULTS 61
10. POINT SPREAD FUNCTION 63
10.1 PROBLEM FORMULATION 63
10.2 CONCLUSION 65
11. TURNTABLE ISAR 67
11.1 INTRODUCTION 67
11.2 PROBLEM FORMULATION 67
11.3 TURNTABLE ISAR IMAGING 67
11.4 TURNTABLE BEAMSTEERING 69
12. CONCLUSION 71
REFERENCES 73

APPENDICES

A: SPHERICAL HARMONIC SOLUTIONS FOR THE HOMOGENOUS HELMHOLTZ EQUATION **A-1**
B: FINITE SPHERICAL POINT SOURCE GREENS FUNCTION **B-1**
C: DIFFERENTIAL EQUATIONS SOLUTION WITH CONTOUR INTEGRALS..... **C-1**

Figures

Figure 1. Pattern Multiplication of a directional (left) and omnidirectional pattern (right). 7

Figure 2. Comparison of even mode total pattern through the summation of directional element patterns (top left), pattern multiplication (bottom left), the summation of omnidirectional element patterns (top right), and pattern multiplication (bottom right). 9

Figure 3. Comparison of the total pattern antimodal odd mode through the summation of directional element patterns (top left) and pattern multiplication (bottom left), the summation of omnidirectional element patterns (top right), and pattern multiplication (bottom right). 9

Figure 4. Comparison of the total pattern antiphase odd modes; a summation of omnidirectional element patterns (top left) and pattern multiplication (bottom left), the summation of omnidirectional element patterns (top right), and pattern multiplication (bottom right). 9

Figure 5. Mean radiation pattern (A), and cartesian coordinate distribution functions (B), of a volumetric antenna array, scanned from zenith to the meridian elevation angle (C). 10

Figure 6. Meridian sum beam results and comparisons. Computational HFSS -top left with Matlab topographical patterns – top center and - top right. The bottom row provides an overlay of the ϕ – cut plane, bottom left, and θ – cut plane bottom right. 11

Figure 7. Top left, *X*-axis (antiphase) and HFSS 3d patterns, top-left center. The *Y*-axis (antimodal) difference beam results are top-right with HFSS 3d Pattern top-right center. Comparisons with relative HFSS, Matlab, and mean valued ϕ and θ – cut planes are provided on the bottom row for a full comparison of simulated HFSS results. 12

Figure 8. Sum – difference beam expected value (mean – odd columns) versus numerical (even-columns) pattern results: UV – space top and angular space bottom. 12

Figure 9. Distributions of the Sinc modes. 13

Figure 10. Sinc characteristic functions (top-left dB, top-right magnitude) and Cosinc characteristic function (top-right dB and bottom-right magnitude). 14

Figure 11. Characteristic functions of Beta distributions of continuous n; Even-(left) and odd-(right). 14

Figure 12. Distributions of a ring, line, circle, and sphere (left); characteristic functions (right). 16

Figure 13. Distributions of the apeirogon, ring, line, circle, shell, and sphere (left); characteristic functions (right). 16

Figure 14. Engineering Design Flow. 16

Figure 15. Sum-difference beampatterns of the circular canonical family distributions, meridian scans (left), and zenith scans (right). 17

Figure 16. Circular element population polymorphic swarm behavior and sum-difference beampattern generation. 17

Figure 17. SRA pattern broadside (zenith) and endfire (meridian) comparisons from [14] (left) and by (33) (middle – left) (Figures 17 – 18 of [15]) and at the meridian (zenith) scan angle with (θ, ϕ) –cut planes from [14] (middle – right) and by (33) right. 18

Figure 18. CRA pattern broadside and endfire comparisons from [14] (left) and by (34) (middle – left) (Figure19 of [15]) and at endfire in the θ, ϕ –cut planes from [14] (middle – right) and by (34) right (Figures 20 – 21 of [15]). 18

Figure 19. Analytical comparison of (33) – (34) and (42) – (43) at the meridian elevation angle (Figure 41 of [14]), left and zenith elevation angle (Figure 42 of 14]), right. The area in yellow shows a comparison of the first peak and null of (33) – (34) and (42) – (43). 19

Figure 20. Computational HFSS simulations of thirty-two element patch configurations of a CARA (M = 1, A/λ=2.778, ϕ*=7.74°) – left and SARA (M = 1, A/λ = 1.69, ϕ* = 15°) – right. 20

Figure 21. Computational simulations of a Cara (M=1, ϕ*=25°) with comparison its mean value (even-columns), angular space (second row), and UV-space (first row). A comparison of a singular ring Cara (M=1, ϕ*=25°) and (*M*=8, *ϕ**=25°) - right are provided on row three and four to demonstrate the convergence of the solutions. 21

Figure 22. Incremental nullsteering sum beam results and comparisons using N = 32 monopole element distribution-top row. Computational meridian 3D patterns middle row and ϕ – cut plane bottom left; (θ – cut plane bottom right)..... 22

Figure 23. Incremental compound nullsteering (M = 1 – 6) results and comparisons using N=32 monopole element distribution-top row. Computational meridian 3D patterns middle row and ϕ – cut plane bottom row; θ – cut plane second from the bottom row. 23

Figure 24. Incremental compound nullsteering (M = 7) designs using N = 32. 23

Figure 25. Compound nullsteering (M = 1 – 9) simulated designs with N = 32. Element distributions are provided top – left, probability distributions top – middle, three-dimensional patterns, top – rights. The phi – cut plane (right-side) and theta (left side) cut plane is provided on the bottom three rows..... 24

Figure 26. Comparisons of incremental compound nullsteering *CARA* angular (r, θ, ϕ) and UV pattern simulations, M = 1 – 9, with ϕ^* = 25°. 24

Figure 27. Ring distributed monopole array pattern comparison of the theoretical-mean value, numerical-MATLAB, simulated-HFSS and measured results (A/λ = 2.77, ϕ^*= 7.74, N = 18 and M = 1). 25

Figure 28. SARA steered at the meridian elevation angle θ_0 = 90°, ϕ_0 = 0° (ϕ^*=9.0°, 16 monopoles, A/λ = 2.77 and M=1); test setup (left), and SARA steered at the zenith elevation angle θ_0 = 0°, ϕ_0 = 0° (ϕ^* = 9.0°, 32 dipoles, A/λ = 2.77 and M = 1), right..... 25

Figure 29. Measured CRA aperture in four phasing scenarios: full sum (lower-left), full difference (top-left), interior sum (lower-middle) with exterior difference (top-middle), exterior sum (lower-right) with interior difference (top-right). 26

Figure 30. Directivity in Ψ-space is approximately equal for all n..... 27

Figure 31. Superposition diagram (left) converges to a continuous aperture distribution as $N\rightarrow\infty$ (right). 30

Figure 32. Comparison of the Fast Fourier Transform and Expected value of the common distributions, n = 0 ring, n = 1 line, n = 2 circle, and n = 3 sphere. 30

Figure 33. Probability moments of the array factors of a ring, line, circle, and spherical distributions, (left) and notional example of the monotonically decaying radiation pattern (right) [3]. 32

Figure 34. Total even / odd variance. Variance =0 at $\Psi_0 = \delta_0$ = 0° [31], which means the target is fully resolved and deterministically tracked. 32

Figure 35. Comparisons of the radiation pattern variance and mean power (left) and probability moments of the array factor (right). 33

Figure 36. Comparison of the probability distribution of (62)– left and (63) – middle and (64) – right in angular space of an SRA, N=32, A/λ = 2.778. 34

Figure 37. The probability distribution function of the N – element unnormalized complex radiation pattern amplitude. 35

Figure 38. SRA statistics with N = 1000, and A / λ = 1; ϕ – cut plane, left and θ – cut plane right. 40

Figure 39. Ideal statistics for a sparse random array (invariant to distribution or topology – left) and gain of a periodic linear array (meridian scan – right). [39]. 41

Figure 40. Statistics of 1, 2, and 3 dimensional random arrays (zenith – left, meridian theta cut plane – middle & phi cut plane – right). 42

Figure 41. Statistics of a spherical array with fixed aperture size in ϕ and θ – cut planes versus element population N and statistics of a linear periodic array scanned at broadside and meridian. 42

Figure 42. Ideal rectangular element pattern $G(\Psi)$ - left. Non-ideal smoothly varying element pattern – middle and non- ideal smoothly varying element pattern right. 43

Figure 43. Statistical comparisons of a circular (left) and spherical (right) distributed array in zenith scan with patch element factor. 44

Figure 44. Array factors at two slightly different, slightly different wavelengths. 44

Figure 45. Relation to the characteristic polynomial. 48

Figure 46. Characteristic amplitude modes (n = 0 – 5) for a ring random array steered at endfire; Bessel modes (top); Weber modes (bottom). 49

Figure 47. Characteristic amplitude modes (n =1) for a linear random array steered at endfire; theta cut plane shown in the two charts left; phi cut plane middle; HFSS simulations of modes 0 – 2 right. 50

Figure 48. Characteristic amplitude modes (n = 2) for a circular random array steered at endfire (left); Bessel modes 0 – 8 (middle) and modal analysis 0 – 25 (right). 50

Figure 49. EulerSinc, Sinc, and Cosinc modes comparison (left). First n = 12 EulerSinc modes (right). 51

Figure 50. Bessel-Weber modal comparison, (left) and first ten modes superimposed (right). 51

Figure 51. The volume of a source and infinite planar screen (left) and aperture excitation from an isotropic point source (right). 52

Figure 52. Complimentary screens. 53

Figure 53. Complementary triangular topologies (left) and characteristic functions (right). 54

Figure 54. CRA steered at r_0 / 10 (left); r_0 (middle) and r_0 x 10 (right). 55

Figure 55. Doppler shift becomes a function of the scan angle. [43] (top) and an illustration of an approaching target (bottom) [43]. 58

Figure 56. Beampattern of the circular distributed antenna array two-way array factor. Demonstration of the point scatters – left, and mean valued radiation formulation, right. 61

Figure 57. Pulse behavior with N = 5, d = 5 (left) and experimental diagram (right). 62

Figure 58. Mean and numerical pattern comparisons of two rings moving radially and outward with constant velocity. 62

Figure 59. The distribution of 200-point scatters is uniformly distributed and split equally amongst each ring. 64

Figure 60. Imaging of two circularly distributed rings of variable radii, A_1 = 1 and A_2 =3. Equation (148) – left three images and equations (147) – the second image from the right and (150) – right. 65

Figure 61. Uniform amplitude distribution, top, and parabolic amplitude distribution, bottom. 65

Figure 62. Turntable inverse synthetic aperture radar scanning system. 68

This page is intentionally blank.

1. INTRODUCTION

Aperiodic antenna arrays offer a number of potential performance benefits for remotely-deployed ad hoc Wireless Sensor Networks (WSN). On condition that the nodes of the WSN have a level synchronization and geospatial awareness that can facilitate the required amplitude and phase control at each of the WSN nodes, they can utilize collaborative beamforming techniques for long haul communication and back-end relay of information which has been passed throughout the appropriate beamforming nodes of the WSN. The concept of aperture partitioning then plays a significant role in determining which nodes should participate in a given beamforming operation. Developing metrics that can be used to select beamforming nodes in the WSN represents a key step in enabling this type of opportunistic behavior.

One of the steps in developing decisional metrics in this distributed framework requires the assumption that the placement of nodes in the WSN are explicitly for sensing. From a collaborative perspective, where analog beamforming for both transmit and receive is the explicit goal, the unconstrained distribution of these nodes in three-dimensional space may result in sparse or dense arrangements with no apparent lattice or other geometric order. Determining the optimum (or best achievable) complex array weightings for the WSN nodes represents a significant challenge in light of this geometric uncertainty, so it can be advantageous to consider this aperiodic arrangement of radiating elements as a random array since grating lobes are statistically minimized due to the lack of symmetry or periodicity.

This limitation may not be the case for every given physical instantiation of the aperiodic array. However, the stochastic analysis provides estimates on beamforming metrics that can inform the WSN on the probability of these outliers and allow it to factor this into its global decision-making process. It is then logical to develop insight into a random array's properties in a probabilistic manner. Such an approach yields important statistical averages of the radiation pattern, namely, mainbeam behavior, three dB beamwidth, directivity, and sidelobe mean null and peak locations.

The maximum peaking sidelobe behavior is critical in this context since the discrepancy between the peaking sidelobes, and the average sidelobe can be significant if the array is sparse for its electrical dimensions. Inaccurate prediction of this behavior can lead to interference with other systems, susceptibility to jamming, and an overall reduction in the security of the WSN and its information. Hence, an estimator of the peaking sidelobe behavior is a necessity of random arrays. Specifically, this indicator should confine the sidelobe behavior in terms of a probability or confidence interval of which some predicted value will not be exceeded. This threshold is a pertinent characteristic for the WSN, and it is the motivation of this work, which uses circular and spherical topologies of various distributions. These are also used as demonstration vehicles for mathematical development since they do not place restrictions on the resulting array's scan volume.

The paper's organization begins with historical work of the exact array factor of a spherical array and expands to approximations. A derivation of the probability density function of circular antenna arrays in one, two, and three-dimensional space follows the formulation of respective array factors and mean valued radiation patterns for volumetric, planar, and linear environments. Afterward, the maximum peaking sidelobe (MPS) is inspected using the array factor determined from a Gaussian distribution. A correlation-based method for finding the MPS follows this since greater accuracy is necessary to identify maximum peaking sidelobes in either the mainlobe region or environments of elements populations. Follow on sections present orthogonality of beampatterns with multi beams, frequency range, and doppler effects introduced in beamsteering of mobile distributions and introductions to inverse synthetic aperture radar. A short conclusion ends this paper.

This page is intentionally blank.

2. STATISTICAL PROBLEM FORMULATION AND ANALYSIS OF A CIRCULARLY DISTRIBUTED RANDOM ANTENNA ARRAY

Circular and spherical random arrays were first analyzed by Panicali and Lo using the variance, mean, and the correlation between elements [1]. A further and insightful analysis was considered by [2] approximately a decade later with examinations of circular [3 – 4] and spherical [5 – 15] array geometries.

2.1 FORMULATION OF THE EXACT ARRAY FACTOR

The exact array factor can be shown as

$$F\left(\theta,\phi\middle|R_n\right)=\sum_{n=1}^{N}e^{jkR_n}\Big/N=\sum_{n=1}^{N}e^{jkr\sqrt{1+x^2-2x\cos\psi_n}}\Big/N,x=r_n/r$$
$$\cos\theta\equiv\cos\psi_n=\sin\theta\sin\theta_n\cos\left(\phi-\phi_n\right)+\cos\theta\cos\theta_n=\hat{r}\cdot\hat{r}_n \tag{1}$$

Since r is not a part of the integration it is placed into the term β (4, [16]]) such that $\beta = 2\ \pi\ \Delta f\ r\ /\ c$. Next, integration is done over the spherical volume of an isotropic point source located on the z-axis by (2), and (3). [1 – 17] Likewise, due to the change of variables ($x = r_n / r$), one obtains the multiplication of r^3 in (4) and reduces to (5) over its circularly symmetric ϕ integration.

$$\cos\theta\equiv\left(\cos\psi_n\middle|\theta_n=0^\circ\right)=\hat{r}\cdot\hat{r}_n=\cos\theta \tag{2}$$

$$\int_0^{r_n}\int_0^{\pi}\int_0^{2\pi}\exp\left[-j\beta\sqrt{1+\left(r_n/r\right)^2-2\left(r_n/r\right)\cos\theta}\right]r_n^2dr_n\sin\theta d\theta d\phi \tag{3}$$

$$r^3\int_0^{A/r}\int_0^{\pi}\int_0^{2\pi}\exp\left[-j\beta\sqrt{1+x^2-2x\cos\theta}\right]x^2dxd\Omega, \tag{4}$$

$$2\pi r^3\int_0^{x'}\int_0^{\pi}\exp\left[-j\beta\sqrt{1+x^2-2x\cos\theta}\right]x^2dx\sin\theta d\theta,\quad d\Omega=\sin\theta d\theta d\phi, x=r_n/r, dx=dr_n/r,\{r\equiv R_A, x'\equiv A/r\} \tag{5}$$

Substituting $u = [1+x^2 – 2x \cos \theta]^{½}$, $u\ du = x \sin \theta d\theta$ into the θ integration simplifies (5) to (6) and reduces to (7). [17]

$$2\pi r^3\int_0^{x'}xdx\int_{|1-x|}^{1+x}\exp\left[-j\beta u\right]udu \tag{6}$$

$$\pi r^3\int_0^{x'}xdx\left\{e^{\left(-j\beta(1+x)\right)\left[1+j\beta(1+x)\right]}-e^{\left(-j\beta|1-x|\right)\left[1+j\beta|1-x|\right]}\right\}\Big/\beta^2 \tag{7}$$

The final integration is divided into two regions (8) due to the absolute value of (7) and reduces to (9) for $x' > 1$ and $\theta = \beta x'$.

$$\frac{\pi r^3}{\beta^2}\left(\int_0^1 xdx\left\{e^{\left(-j\beta(1+x)\right)\left[1+j\beta(1+x)\right]}-e^{\left(-j\beta|1-x|\right)\left[1+j\beta|1-x|\right]}\right\}+\int_1^{x'} xdx\left\{e^{\left(-j\beta(1+x)\right)\left[1+j\beta(1+x)\right]}-e^{\left(-j\beta|1-x|\right)\left[1+j\beta|1-x|\right]}\right\}\right) \tag{8}$$

$$\bar{F}_{x'>1}=4\pi j\left(r/\beta\right)^3 e^{-j\theta}\left\{2e^{j\theta}j\theta+\left(1+j\theta-\theta^2/2\right)\left(\cos\beta-3\mathrm{sinc}\beta\right)+\theta^2\left(\cos\beta-\mathrm{sinc}\beta\right)/2\right\} \tag{9}$$

Otherwise for $x' < 1$ the term $|1 - x|$ simplifies to $(1 - x)$ and provides

$$\bar{F}_{x'<1}=2\pi r^3\left(2j\,e^{-j\beta}/\beta^3\right)\left\{\sin\theta\left[\theta^2/\beta-j-3/\beta\right]+\theta\cos\theta\left(j+3/\beta\right)\right\} \tag{10}$$

In the two-extremes of large and small x', (9) reduces to (11) and (10) to (12), respectively.

$$\bar{F}_{x'\gg1}=6\sqrt{\left(\theta-\sin\theta\right)^2+\left(1-\theta^2/2-\cos\theta\right)^2}\Big/\theta^3 \tag{11}$$

$$\bar{F}_{x'\ll1}=\frac{-3\theta\cos\theta+3\sin\theta}{\theta^3}=3\mathrm{tinc}\left(\theta\right)=3\mathrm{tinc}\left(\Psi\right) \tag{12}$$

where $\Psi = \theta = \beta x' = \beta A/r = kA$, is taken over all angular space (θ, ϕ). This result also validates Figure 5 of [15] and yields a graphical solution of 1.815, with an agreement to historical work of with the analysis in Figure 3 of [2]. Expansions of this work in the Fresnel region were investigated in [6 – 7].

We diverge by the approximation since we do not take an integral over Rn's exact space, but its expansion of (1). What is odd about this solution is the lack of multiplication of pattern multiplication. There is no pattern multiplication due to the substitution from angular space to Ψ – space. Therefore (12) , the solution to a spherical random array in the far-field is missing information about the sphere's surface area. [18] Hence, the total solution to a spherical random array in the far-field for transmitting is given by pattern multiplication. [6 – 15]

This new method of using compound random variables has helped unleash the total solution to a spherical random array, a product of pattern multiplication of the symmetries encountered in three dimensions, which differs from historical works of [19 – 20]. We also note corrections to works of [3 – 4] and [15] in figures 17 – 21 and figures 41 – 42 of [14].

2.2 PROBABILITY AND CUMULATIVE DENSITY FUNCTIONS OF A CIRCULARLY DISTRIBUTED ELEMENT POPULATION

The probability density function (*PDF*) of a uniformly distributed circular canonical family (*CCF-PDF*) (13) is derived from the joint density function of (14) and renormalized by that of (15) such that dimensional topology increases by order of *n*. E.g., the ring, line, circle, and spherical geometrical distributions are generated by substitution of *n = 0*, 1, 2, and 3 respectively. The corresponding cumulative density function of a circularly distributed (*CCF – CDF*) element population (*CCF-PDF*) is provided in (16) for completeness and peaks to unity in two ways. It approximates a Gaussian distribution centered at *x* = .5 for large *n,* and for small *n,* the distribution is sparse and peaks at the edges of the distribution |*x*| = 1.

$$f_X\left(x\right)=\left(\left(1-x^2\right)\Gamma\left(5/2+n\right)\right)\Big/\left(\sqrt{\pi}\Gamma\left(\left(1+n\right)/2\right)\right) \tag{13}$$

$$\int_{-\sqrt{1-y^2-z^2}}^{\sqrt{1-y^2-z^2}} \int_{-\sqrt{1-y^2}}^{\sqrt{1-y^2}} \int_{-1}^{1} f_{\mathrm{X,Y,Z}}(\mathrm{x},\mathrm{y},\mathrm{z})\left(\sqrt{1-x^2-y^2-z^2}\right)^n dxdydz = 1$$
$$\Rightarrow f_{\mathrm{X,Y,Z}}(\mathrm{x},\mathrm{y},\mathrm{z})\big|_{A=1} = \left((1+n)\Gamma(5/2+n)\right)\Big/\left(\pi^{3/2}\Gamma(2+n)\right) \tag{14}$$

$$f_E(x;n) = \left(1-x^2\right)^{\frac{n-1}{2}}\Gamma(1+n/2)\Big/\left(\sqrt{\pi}\Gamma\left((n+1)/2\right)\right), \qquad f_O(x;n) = f_E(x;n)\,\mathrm{sgn}(x) \quad \neg(n \geq -1) \tag{15}$$

$$F_X(x) = \frac{2x\Gamma(1+n/2)\,{}_2F_1\left(1/2,(1-n)/2;3/2;x^2\right)}{\sqrt{\pi}\Gamma\left((1+n)/2\right)} \tag{16}$$

2.3 PROBABILITY MOMENTS OF THE CIRCULARLY DISTRIBUTED ELEMENT POPULATION

The mean, variance, skewness, kurtosis, and excess kurtosis are provided by the probability moments of (17) and are found from the raw and central moments of (18) – (19). The mean and skew are equal to zero since the element distribution is circularly symmetric. On the other hand, the variance converges to zero for large values of x as the element population clusters towards the center of the element population, providing lower kurtosis values.

$$\begin{aligned} &\mu = \mu'_1 = 0, && \sigma^2 = \mu'_2 - \mu^2 = 1/(2+n), && \gamma_1 = \mu_3/\mu_2^{3/2} = 0 \\ &\beta_2 = \mu_4/\mu_2^2 = 3(2+n)/(4+n), && \gamma_2 = \mu_4/\mu_2^2 - 3 = -6/(4+n) \end{aligned} \tag{17}$$

$$\mu'_N = \int_{-1}^{1} x^N f_E(x;n)\,dx = \frac{\left(1+(-1)^N\right)\Gamma(1+n/2)}{2\sqrt{\pi}\Gamma\left((2+n+N)/2\right)} \tag{18}$$

$$\begin{aligned} &\mu_0 = 1, && \mu_1 = \mu'_1, && \mu_2 = \mu'_2 - \mu'^2_1 \\ &\mu_3 = 2\mu'^3_1 - 3\mu'_1\mu'_2 + \mu'_3, && \mu_4 = -3\mu'^4_1 + 6\mu'^2_1\mu'_2 - 4\mu'_1\mu'_3 + \mu'_4 \end{aligned} \tag{19}$$

2.4 FORMULATION OF THE ARRAY FACTOR

The array factor of a volumetric antenna array of *independent and identically distributed* (i.i.d.) isotropic radiators is provided (20) with spherical random variables (21) and steering functions (22).

$$F(\theta,\phi|\mathrm{x}_n,\mathrm{y}_n,\mathrm{z}_n) = \sum_{n=1}^{N} e^{j(uX+vY+wZ)}\Big/N \tag{20}$$

$$\begin{aligned} &X = \tilde{r}_n \sin\theta_n \cos\phi_n, Y = \tilde{r}_n \sin\theta_n \sin\phi_n, Z = \tilde{r}_n \cos\theta_n, \\ &\mathrm{X} \triangleq \langle \mathrm{X},\mathrm{Y},\mathrm{Z} \rangle, -1 \leq \mathrm{X} \leq 1, \tilde{r}_n = r_n/A, \tilde{A} = A/\lambda \end{aligned} \tag{21}$$

$$\begin{aligned} &u = \hat{\mathrm{x}}\cdot\cos\bar{\psi}, v = \hat{y}\cdot\cos\bar{\psi}, w = \hat{z}\cdot\cos\bar{\psi}, 1 = \sqrt{u^2+v^2+w^2} \\ &\cos\bar{\psi} = kA\left(\hat{\mathrm{r}}(\theta,\phi) - \hat{\mathrm{r}}(\theta_0,\phi_0)\right) \end{aligned} \tag{22}$$

Simplification of the direction cosines in (21) – (22) provides Psi space (Ψ)[1], which is taken over all angular space (θ, ϕ), similar to u, v, and w space of traditional array theory [19] as shown in (23).

$$\Psi = \cos\left(\vec{\psi}\right) = kA\left(\hat{\mathrm{r}}\left(\theta,\phi\right) - \hat{\mathrm{r}}\left(\theta_0,\phi_0\right)\right) = \cos^{-1}\left[u \quad v \quad w\right]. \tag{23}$$

Likewise, the random variables are also compacted such that $X = \{X, Y, \text{and } Z\}$.

Moreover, the complex array factor of the random array may be expanded into real (even) and imaginary (odd) components (Euler's identity) as F (Ψ)=S (Ψ) + j D(Ψ). The functions *S (sum-beam)* and *D (difference-beam)* are, for each value of Ψ, sums of large numbers of independent random variables with S ($\Psi \mid X_n$) = cos ($X_n \Psi$) and D ($\Psi \mid X_n$) = sin ($X_n \Psi$). These functions are random variables because the X_n are random, and they are independent because of assumed independence of X_n. Furthermore, no one of them can be so large as to dominate the sum, and according to the central limit theorem, these properties of the constituents of S and D are enough to ensure that each sum's pdf is a Gaussian or normal distribution.

2.5 FORMULATION OF THE MEAN VALUED ARRAY FACTOR

The ensemble average of the array factor is shown by assuming the overbar representation of

$$\overline{F}\left(\theta,\phi\right) = \frac{1}{N}\sum_{n=1}^{N} e^{jkr_n \cos\Psi_n} \tag{24}$$

[1] Ψ-space provides patterns that are invariant to scan behavior. Hence, final patterns should always be converted back to angular (θ, ϕ) – space for associated variances arising from changes in the overall effective volumetric aperture induced from scanning. Also, conversion to Ψ – space is useful for its utmost compactness and complete mathematical convenience when attempting to understand the complex environment of {u, v, w} – space.

This result is recognized as the characteristic function of $r_n \cos \Psi_n$ in angular space and can then be integrated against a given probability element distribution function (pdf) $f_X(x)$, yielding it has associated characteristic function $\Lambda(\Psi)$ in closed form.

$$\Lambda(\Psi) = \bar{F}(\Psi) = \bar{S}(\Psi) + \bar{D}(\Psi) = \oint f(x)\, e^{j\Psi x} dx \tag{25}$$

This result is recognized as the characteristic function of Ψ space Where $\bar{S}(\Psi)$ and $\bar{D}(\Psi)$ are the corresponding even and odd modes of the designated design pattern $\bar{F}(\Psi)$; also related to the quadrature components in digital signal processing. Furthermore, it is well known from [19 – 29] that the complex radiation mean-valued radiation pattern can be matched to any desired radiation pattern by selecting the *pdf* of element location accordingly. This approach is analogous to using the far field-transform relationships of aperture theory and makes the random array capable of being drastically thinned without altering its average pattern behavior.

2.6 FORMULATION OF THE MEAN VALUED RADIATION PATTERN

2.6.1 Mean pattern

The radiation pattern of array theory is traditionally described by the total radiation pattern (TP). This result is expressed as the multiplication of two factors, describing the individual antenna element contribution (EF) multiplied by the array factor (AF). Conventional representation of this is provided in Figure 1 for a directional and omnidirectional pattern. A second method is to sum all of the element patterns. Examples of the total pattern of these two methods are provided in Figure 2 – Figure 5.

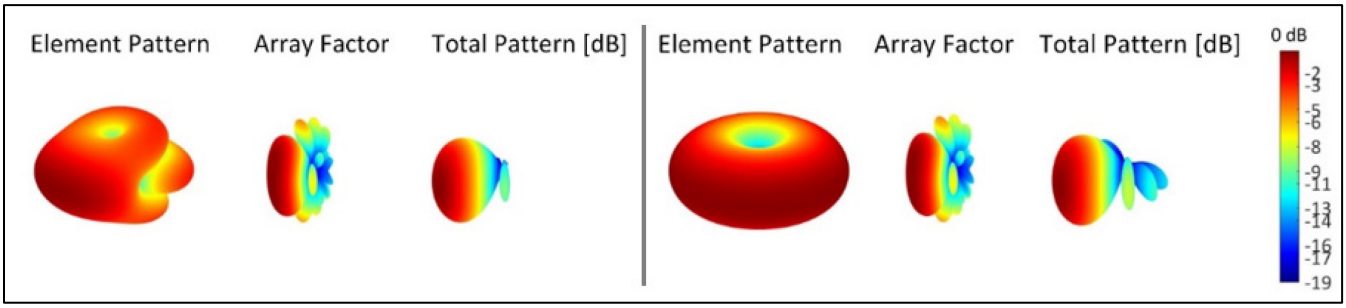

Figure 1. Pattern Multiplication of a directional (left) and omnidirectional pattern (right).

When discussing aperiodic (random) arrays, it is of interest to characterize its mean or expected beampattern for any geometrically bound topology to better its relative radiative characteristics. This process has been shown in [3 – 15] by taking the expected value of the power pattern $|\bar{F}(\Psi)^2|$ across the unit interval [-1, 1]. Hence, for a volumetric random variable *x,* this provides one with a general theory towards obtaining characteristic functions orthogonal in all three axes and uncorrelated.

$$\bar{U} = 1/N + (1-1/N)\,\Lambda|u|^2\,\Lambda|v|^2\,\Lambda|w|^2 = 1/N + (1-1/N)\,\Lambda\left|\bar{\Psi}\right|^2, \tag{26}$$

Moreover, the term $1/N$ separates from the expression since integration is done over the entire distribution space. In other words, the cumulative distribution over the entire space is equal to one. This first term in equation (26) is a characteristic pedestal that conveniently describes mean sidelobe behavior; note that it is independent of scan angle. The Λ terms are the characteristic functions of the probability distribution (Fourier transform) [20]. Beamsteering of the main beam is accomplished in the kernel of each characteristic function directional cosine. We observe that the square magnitude of the characteristic function must then describe the array's main-lobe behavior. Hence, analysis of the radiation characteristics of random arrays comes down to finding the aperture distribution's characteristic functions [3 – 15], [19 – 25]. An example of the characteristic functions of (26) is illustrated in Figure 5.

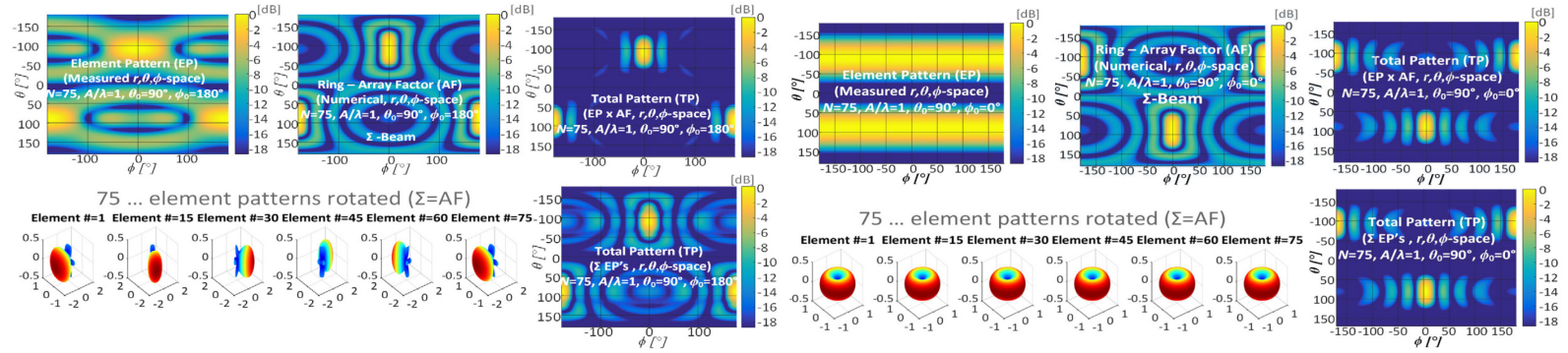

Figure 2. Comparison of even mode total pattern through the summation of directional element patterns (top left), pattern multiplication (bottom left), the summation of omnidirectional element patterns (top right), and pattern multiplication (bottom right).

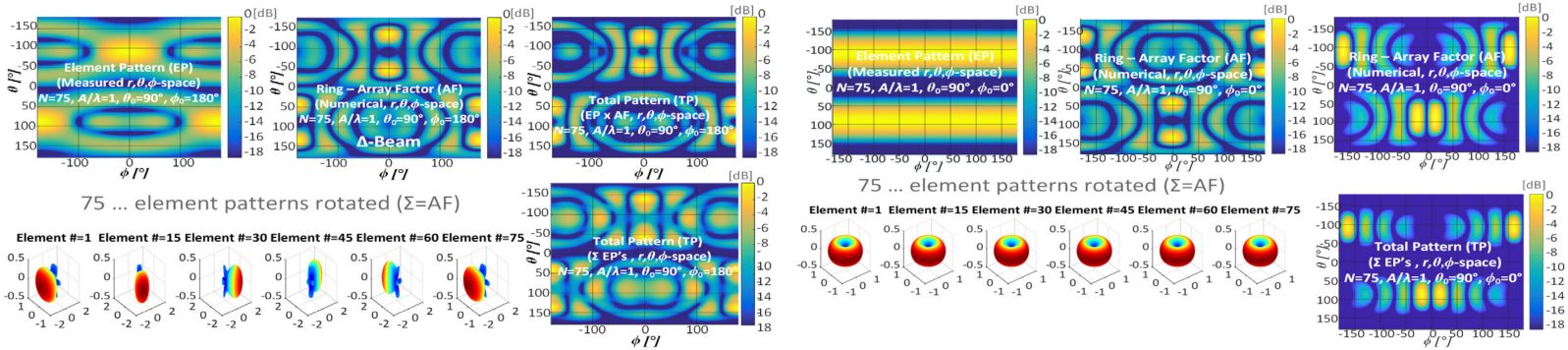

Figure 3. Comparison of the total pattern antimodal odd mode through the summation of directional element patterns (top left) and pattern multiplication (bottom left), the summation of omnidirectional element patterns (top right), and pattern multiplication (bottom right).

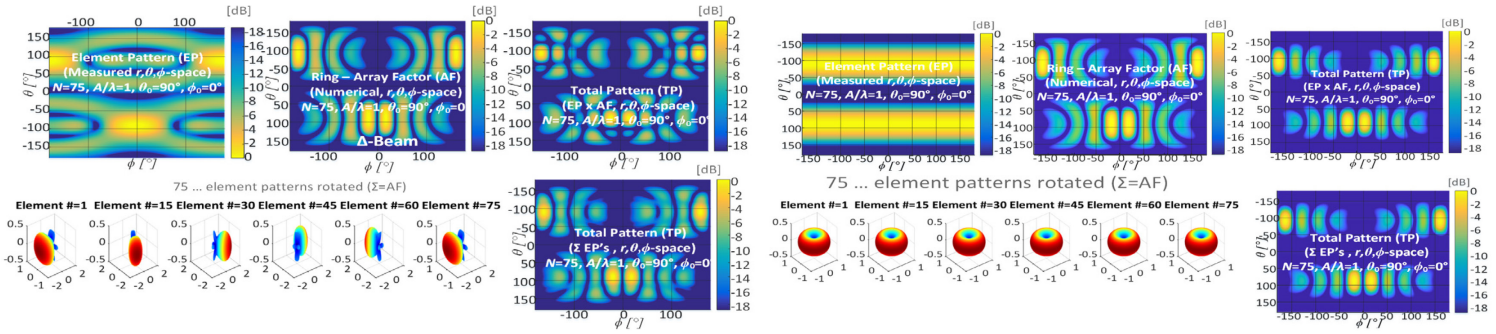

Figure 4. Comparison of the total pattern antiphase odd modes; a summation of omnidirectional element patterns (top left) and pattern multiplication (bottom left), the summation of omnidirectional element patterns (top right), and pattern multiplication (bottom right).

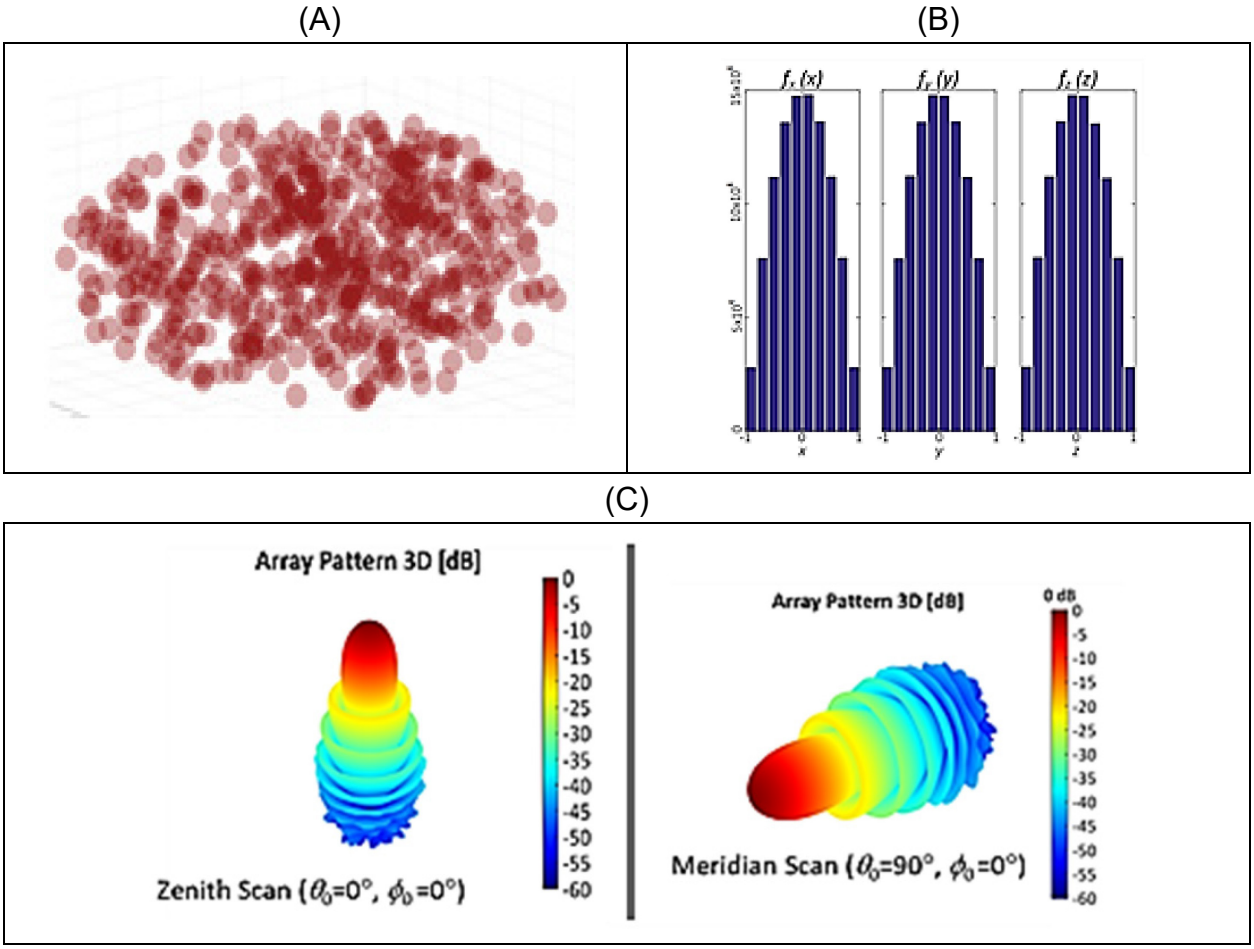

- Zenith to the meridian elevation angle is shown in two views.

Figure 5. Mean radiation pattern (A), and cartesian coordinate distribution functions (B), of a volumetric antenna array, scanned from zenith to the meridian elevation angle (C).

Applying the equation's distribution (13) generalizes the expected radiation pattern for an arbitrary array and can be extended to yield two sets of characteristic functions: an even set for sum beams (27) and an odd set for difference beams (28).[2] Examples of the three-dimensional simulated HFSS versus analytical, sum, and difference beams are provided in Figure 6 – Figure 8 for $n = 0$.

$$\Lambda_E(\Psi;n)=\int_{-1}^{1} f_E(x;n)\,e^{jx\Psi}=\mathrm{Sinc}_n(\Psi) \qquad \neg\mathrm{Sinc}(\Psi;n)=\Gamma(n/2+1)J_{n/2}(\Psi)/(\Psi/2)^{n/2} \tag{27}$$

$$\Lambda_O(\Psi;n)=\int_{-1}^{1} f_O(x;n)\,e^{jx\Psi}=\mathrm{CoSinc}_n(\Psi;n) \qquad \neg\mathrm{CoSinc}(\Psi;n)=\Gamma(n/2+1)H_{n/2}(\Psi)/(\Psi/2)^{n/2} \tag{28}$$

[2] The result of (28) can also be found in the Fourier domain by taking the Hilbert Transform of Sinc (Ψ;n).

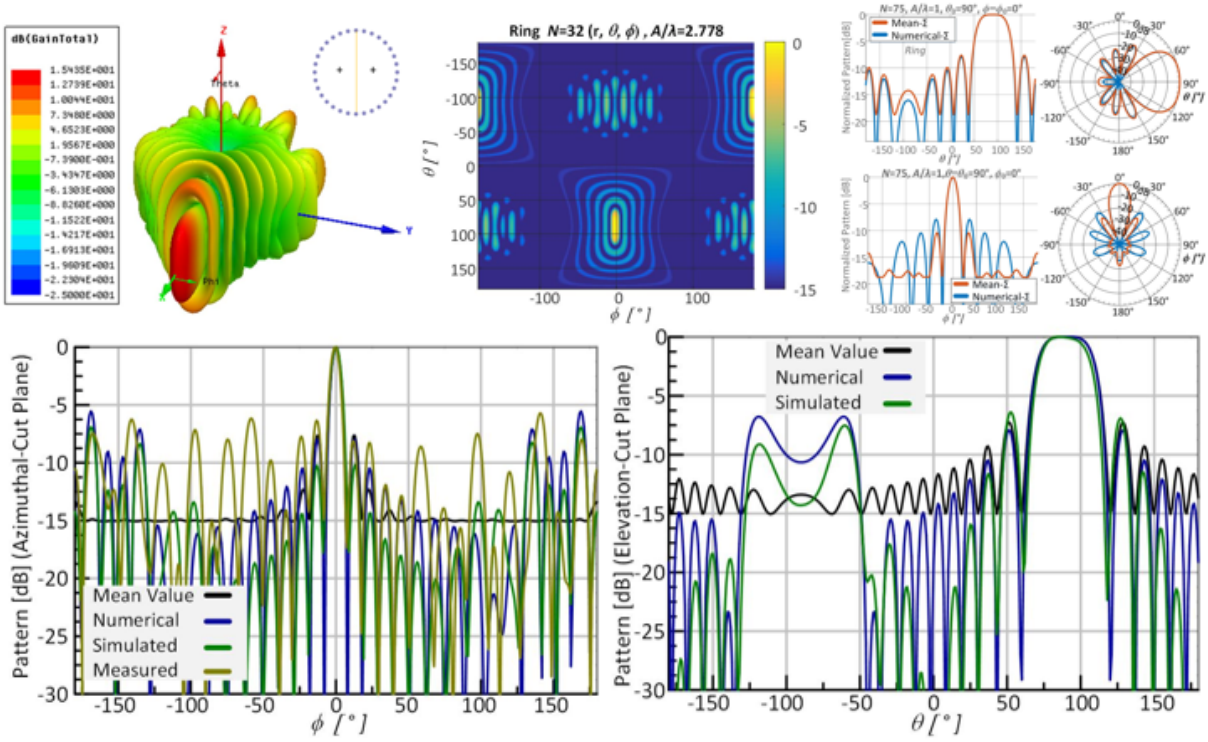

Figure 6. Meridian sum beam results and comparisons. Computational HFSS -top left with Matlab topographical patterns – top center and - top right. The bottom row provides an overlay of the ϕ – cut plane, bottom left, and θ – cut plane bottom right.

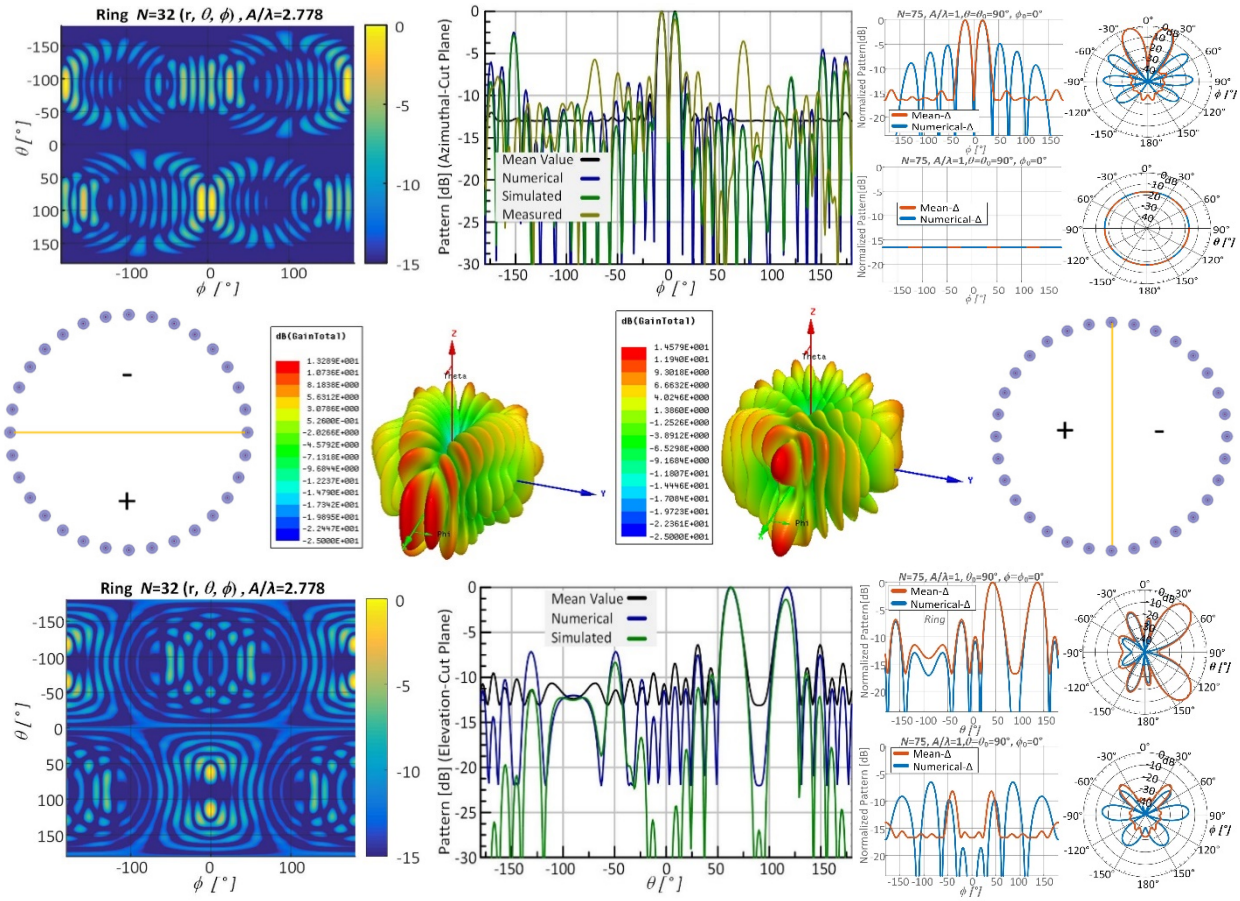

Figure 7. Top left, *X*-axis (antiphase) and HFSS 3d patterns, top-left center. The *Y*-axis (antimodal) difference beam results are top-right with HFSS 3d Pattern top-right center. Comparisons with relative HFSS, Matlab, and mean valued ϕ and θ – cut planes are provided on the bottom row for a full comparison of simulated HFSS results.

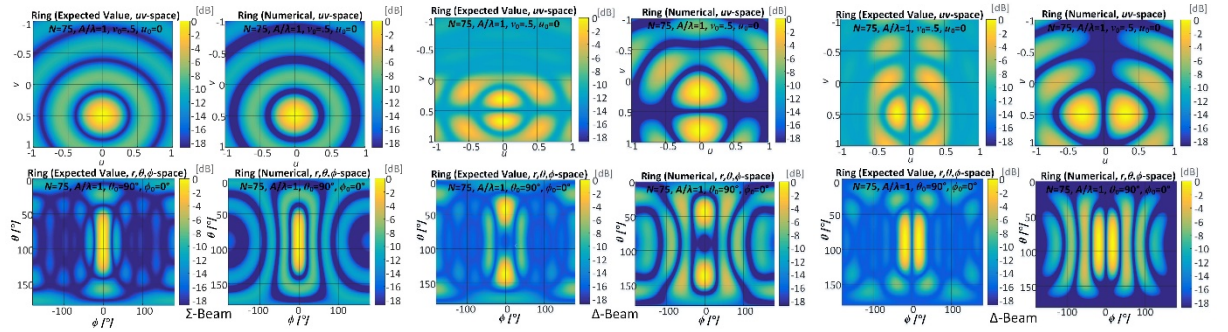

Figure 8. Sum – difference beam expected value (mean – odd columns) versus numerical (even-columns) pattern results: UV – space top and angular space bottom.

By analyzing the respective Sinc_n and CoSinc_n tapers of equations (27) and (28) one can identify that the solution sets alternate between Bessel/Struve and spherical Bessel/Struve functions. Secondly, the Sinc_n, family derived in this work is weighted amongst the interval [-1, 1], whereas the well-known Beta distribution is weighted amongst an interval of [0, 1] with symmetric degrees of

freedom (29). By coincidence, it has been determined that there is no fundamental difference in relations except that the Beta distribution is only half the effective aperture since hence, Ψ is divided by a factor of two (shown in curly braces in (29)). Finally, the characteristic function of the *Beta* distribution is commonly referred to as the confluent hypergeometric function, as shown below.

$$ {}_1F_1\left(\alpha;\alpha+\beta;\mathrm{j}\Psi/\{2\}\right) = {}_1F_1\left(n/2;n;\mathrm{j}\Psi/\{2\}\right)_{\alpha=\beta=n/2} \tag{29} $$

In total, the solutions set of the Sinc_n tapers are generalizations of the *Beta* distribution. For instance, the probability density functions described in this analysis are equivalent when $\alpha = \beta$. Thus, for this type, β (0,0) is Haldane's prior probability and describes the apeirogon. β (½, ½) is the arcsine distribution and represents the horocycle. Following this sequence, β (1, 1) is the Wigner semicircle distribution and represents the circle, and β (3/2, 3/2) is the parabolic distribution and represents the sphere. Other solutions of half-integer order represent Gaussian tapers of the circle and sphere. A complete illustration of the beta distribution (circular canonical family, CCF) is provided below in Figure 9 to illustrate the characteristic function of discrete *n*, Figure 10, and continuous *n,* Figure 11.

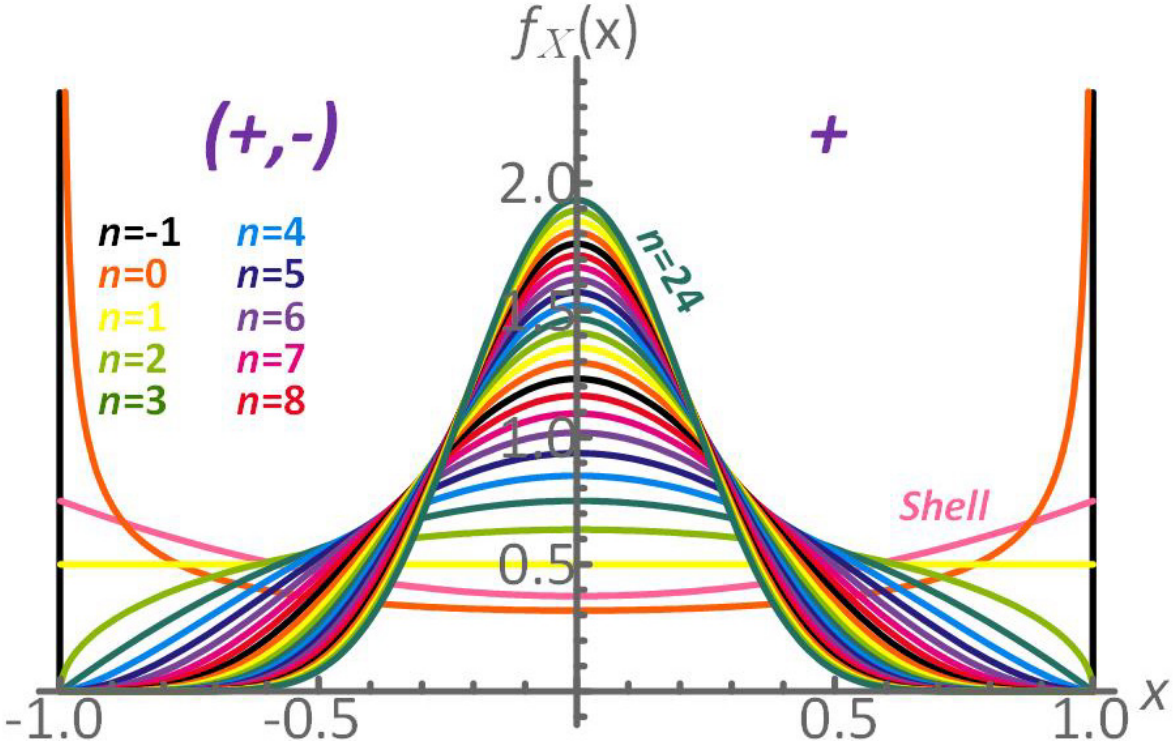

Figure 9. Distributions of the Sinc modes.

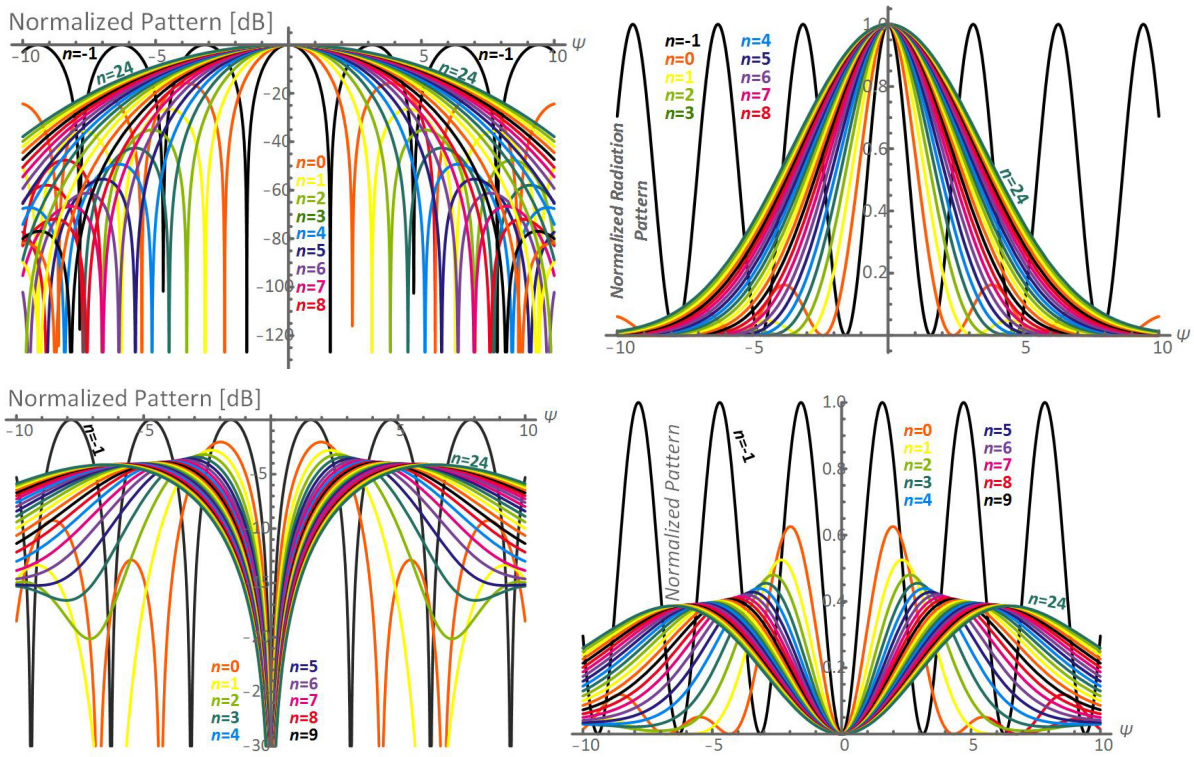

Figure 10. Sinc characteristic functions (top-left dB, top-right magnitude) and Cosinc characteristic function (top-right dB and bottom-right magnitude).

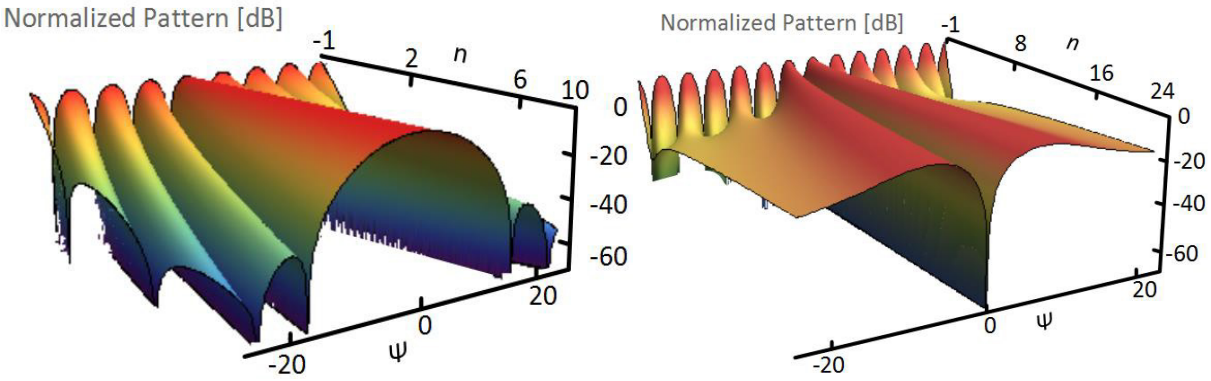

Figure 11. Characteristic functions of Beta distributions of continuous n; Even-(left) and odd-(right).

2.6.2 Mean pattern in complex psi space

The characteristic function approach (Fourier analysis) can be further generalized by finding the moment-generating function (MGF) for this probability distribution. In probability theory, the MGF (when it exists) provides an alternative description to a random system and can be used to compute successive probability moments quickly. Mathematically, it closely resembles the bilateral Laplace transform [23].

$$M(\Psi)=\Lambda(\Psi)=\int_{-\infty}^{\infty} f_X(x)e^{\Psi x}dx \qquad =\left(\bar{S}(\alpha)+\bar{S}(j\beta)\right)+\left(\bar{D}(\alpha)+\bar{D}(j\beta)\right) \tag{30}$$

If $\Psi = \alpha + \mathrm{j}\,\beta$ were taken to be a complex variable, the real part α can be thought of as attenuation in the array factor. The moment generating function evaluated along the imaginary axis ($\alpha = 0$) is the characteristic function (Fourier transform) inside a lossless medium. Therefore, evaluating the moment generating function along contours in the complex plane can account for differing environmental impacts on the array factor. Physically, α should be taken to be negative to represent attenuation properly. Hence, similar to (27) – (28) the lossy mean valued characteristic functions are

$$M_E(\Psi;n) = \mathrm{Sinhc}(\Psi;n) = \Gamma(n/2+1) I_{n/2}(\Psi) / (\Psi/2)^{n/2} \tag{31}$$

$$M_O(\Psi;n) = \mathrm{CoSinhc}(\Psi;n) = \Gamma(n/2+1) L_{n/2}(\Psi) / (\Psi/2)^{\frac{n}{2}} \tag{32}$$

The special functions $I_n(\Psi)$ and $L_n(\Psi)$ are the modified Bessel and Struve functions [30], respectively. Since these functions are closely related to the hyperbolic sines and cosines (mathematical generalizations), the n^{th} mode solutions in Equations (31) and (32) form a family of Sinhc (Even) and CoSinhc (Odd) characteristic modes for the circular distribution of (13). Comparisons of Psi space are provided in Figure 12 for *n=0* – 3 and Figure 13 for *n= -1 – 3* and includes a shell for completeness of circularly symmetric topology [8], [14], and [18].

2.6.3 Mean pattern in angular space

Examples of the mean-valued beam patterns (27) are illustrated in angular space for a *SRA, n=3* (33) , and *CRA, n=2* (34), *RRA, n=0* (35), and *LRA*, *n = 1* (36) to demonstrate spatial variations of the effective aperture and pattern variation outside of the circularly symmetric Psi space. Examples of angular space beampatterns are illustrated in Figures 14 – 16.

$$\bar{U}(\theta,\phi) \overset{Sph}{=} \begin{matrix} 1/N + (1-1/N) \\ \neg\left\{ \mathrm{tinc}(x) = \dfrac{j_1(x)}{x} \right\} \end{matrix} \begin{bmatrix} 3\mathrm{tinc}\left|kA(\hat{x}\cdot\hat{r})\right|^2 \\ 3\mathrm{tinc}\left|kA(\hat{y}\cdot\hat{r})\right|^2 \\ 3\mathrm{tinc}\left|kA(\hat{z}\cdot\hat{r})\right|^2 \end{bmatrix} = 1/N + (1-1/N)3^3 \begin{bmatrix} |\mathrm{tinc}\,u|^2 \\ |\mathrm{tinc}\,v|^2 \\ |\mathrm{tinc}\,w|^2 \end{bmatrix} \tag{33}$$

$$\bar{U}(\theta,\phi) \overset{Cir}{=} \begin{matrix} 1/N + (1-1/N) \\ \neg\left\{ \mathrm{jinc}(x) = \dfrac{J_1(x)}{x} \right\} \end{matrix} \left[2\mathrm{jinc}\left|kA(\hat{x}\cdot\hat{r})\right|^2 \, 2\mathrm{jinc}\left|kA(\hat{y}\cdot\hat{r})\right|^2 \right] = 1/N + (1-1/N)2^2 \left[\left|\mathrm{jinc}(u)\right|^2 \left|\mathrm{jinc}(v)\right|^2 \right] \tag{34}$$

$$\bar{U}(\theta,\phi) \overset{Ring}{=} \begin{matrix} 1/N + (1-1/N) \\ \neg\{\mathrm{rinc}(x) = J_0(x)\} \end{matrix} \left[\mathrm{rinc}\left|kA(\hat{x}\cdot\hat{r})\right|^2 \mathrm{rinc}\left|kA(\hat{y}\cdot\hat{r})\right|^2 \right] = 1/N + (1-1/N) \left[\left|\mathrm{rinc}(u)\right|^2 \left|\mathrm{rinc}(v)\right|^2 \right] \tag{35}$$

$$\bar{U}(\theta,\phi) \overset{Line}{=} \begin{matrix} 1/N + (1-1/N) \\ \neg\{\mathrm{sinc}(x) = j_0(x)\} \end{matrix} \left[\mathrm{sinc}\left|kA(\hat{x}\cdot\hat{r})\right|^2 \right] = 1/N + (1-1/N) \left[\left|\mathrm{sinc}(u)\right|^2 \right] \tag{36}$$

Moreover, the spatially damped oscillatory sinusoids, rinc, sinc, jinc, and tinc completely characterizes the beampattern for a ring, line, circular and spherical distribution. Finally, these results follow differently from previous works in angular space since the total pattern is a combination of pattern multiplication composed of the directional cosine in *x*, *y,* and *z* [29].

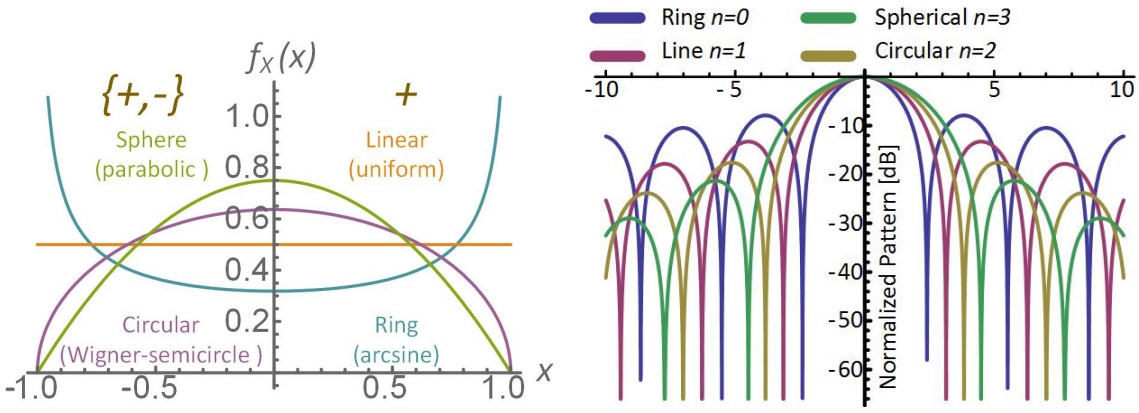

Figure 12. Distributions of a ring, line, circle, and sphere (left); characteristic functions (right).

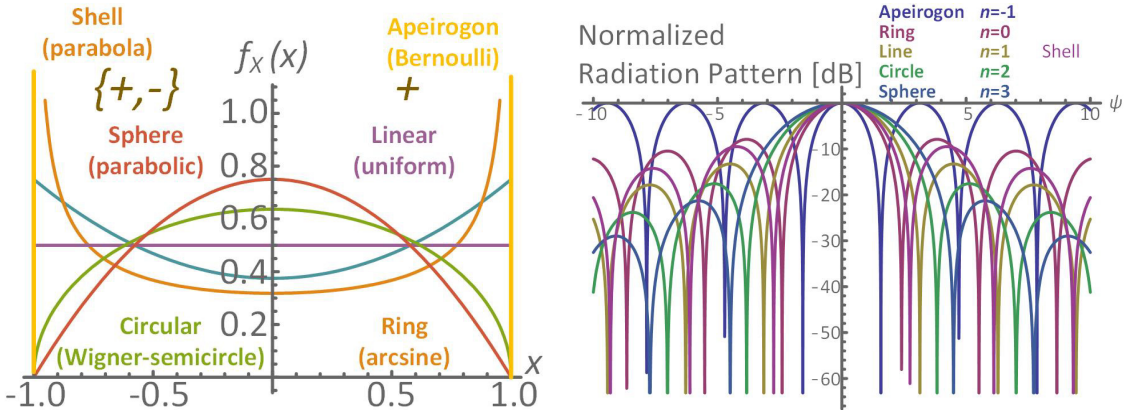

Figure 13. Distributions of the apeirogon, ring, line, circle, shell, and sphere (left); characteristic functions (right).

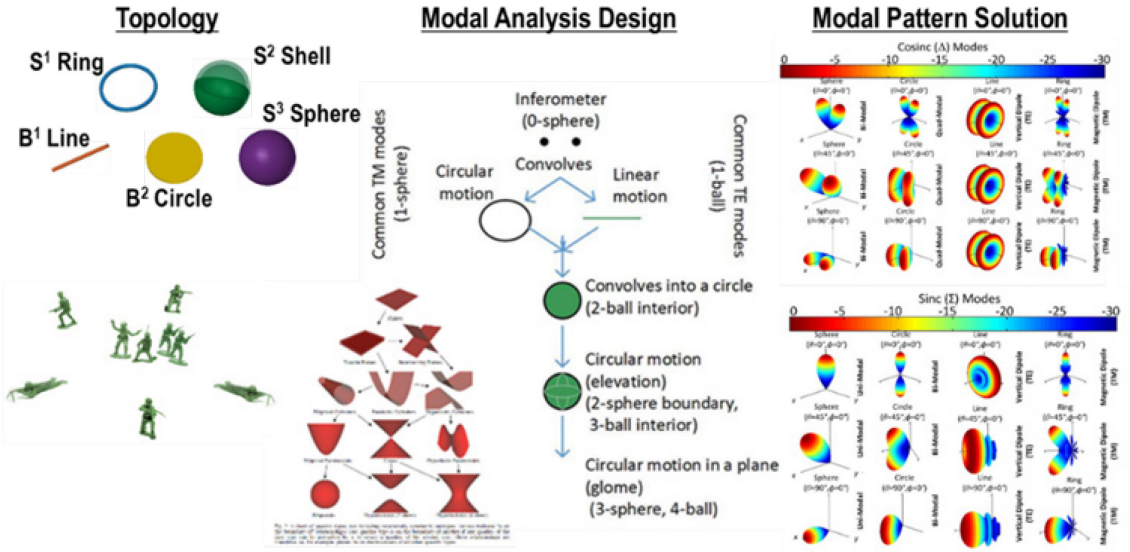

Figure 14. Engineering Design Flow.

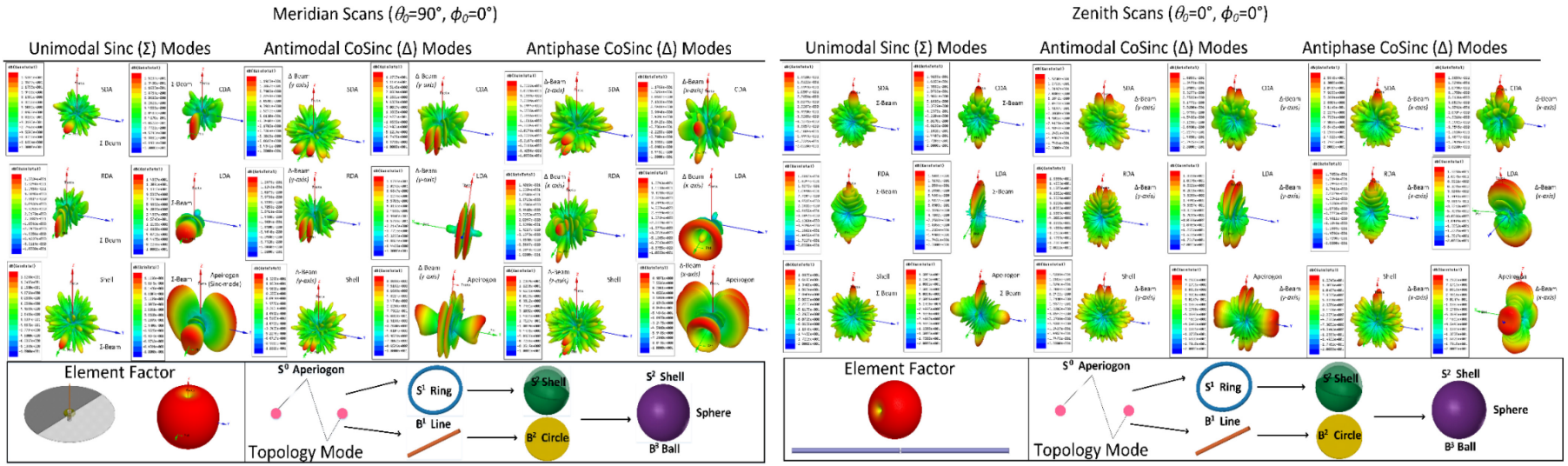

Figure 15. Sum-difference beampatterns of the circular canonical family distributions, meridian scans (left), and zenith scans (right).

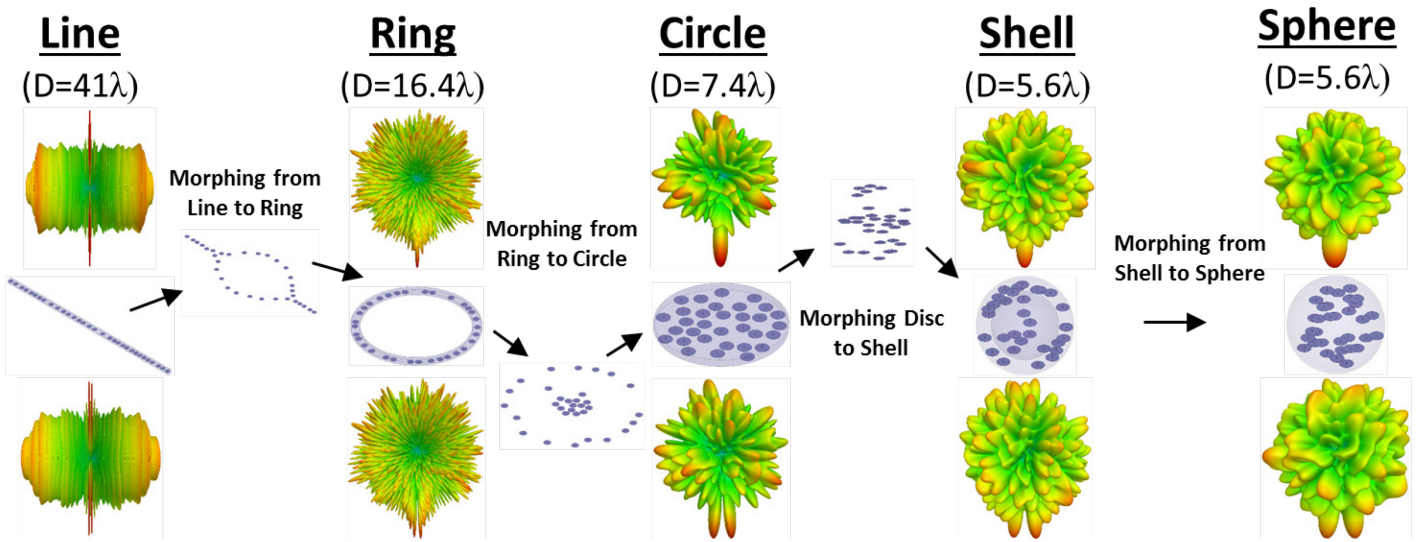

Figure 16. Circular element population polymorphic swarm behavior and sum-difference beampattern generation.

2.6.4 Comparison to prior work [15]

Reflection of (33) presents several unique features of the array. First, there should be no fundamental difference in the radiation pattern whether it is steered at broadside (zenith elevation angle $\theta_0 = 0°$) or endfire (meridian elevation angle $\theta_0 = 90°$). Second, the array is spherically symmetric and orientation agnostic such that the notation should lose a sense of physical meaning for the *SRA* except when suggested mathematically. Figure 17 verifies the first observation and compares it to previous analysis [15] and also demonstrates that the pattern has symmetric properties at endfire.

Similarly, Figure 18 demonstrates the pattern in (34) of a *CRA* pattern with normalized aperture $A/\lambda = 2$ has inconsistent sidelobe behavior during scanning from broadside through endfire as expected. I.e., the *CRA* is bimodal at broadside but unimodal at endfire such that the main and alias beams adjoin together. This observation validates the concept of its variant effective aperture induced from scanning. Finally, the fan-shaped beam produced at the endfire is attractive for applications requiring scanning of large spaces.

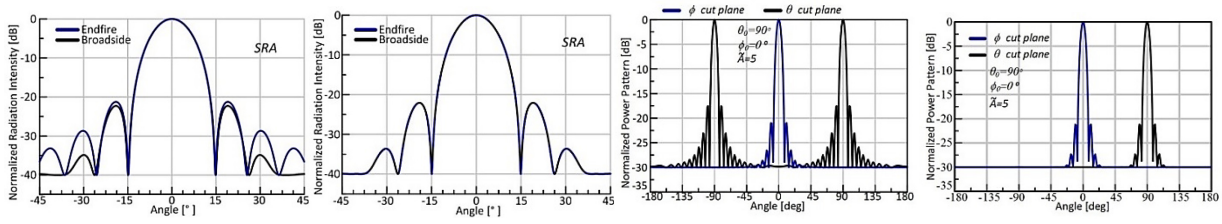

Figure 17. SRA pattern broadside (zenith) and endfire (meridian) comparisons from [14] (left) and by (33) (middle – left) (Figures 17 – 18 of [15]) and at the meridian (zenith) scan angle with (θ, ϕ) –cut planes from [14] (middle – right) and by (33) right.

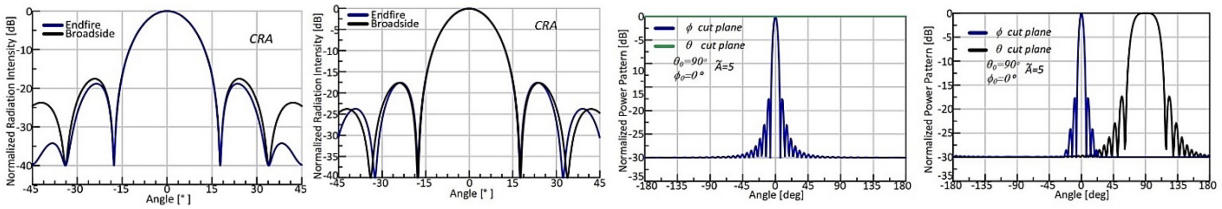

Figure 18. CRA pattern broadside and endfire comparisons from [14] (left) and by (34) (middle – left) (Figure19 of [15]) and at endfire in the θ, ϕ –cut planes from [14] (middle – right) and by (34) right (Figures 20 – 21 of [15]).

2.7 SIMPLIFICATION ZENITH AND MERIDIAN SCAN BEHAVIOR ERRORS

Two beamforming scenarios are covered to understand the error in expected beampatterns of [3 – 4], [13], [15], and [21]. Broadside (zenith) and endfire (meridian) scans are observed for the overwhelming simplification that exists of circular.

Steering at the meridian elevation angle with azimuthal cut-plane Ψ (ϕ, $\theta = 90°$) and elevation cut – plane Ψ (θ, ϕ=0°) simplifies the steering vectors of (33) and (34) to (37) in the ϕ – cut plane and (38) – (39) in the θ – cut plane for either *SRA* or *CRA*, respectively where bracket notation refers to the unit vectors $\hat{x}$, $\hat{y}$, and $\hat{z}$.

$$\Psi_{Endfire}^{SRA,CRA}(\phi) = 2\pi\tilde{A}\langle\cos\phi - 1, \sin\phi, 0\rangle = 2\pi\tilde{A}\left(\left(\cos\phi - 1\right)\hat{x} + \sin\phi\hat{y} + 0\hat{z}\right) \tag{37}$$

$$\Psi_{Endfire}^{SRA}(\theta) = 2\pi\tilde{A}\langle \sin\theta - 1, 0, \cos\theta \rangle \tag{38}$$

$$\Psi_{Endfire}^{CRA}(\theta) = 2\pi\tilde{A}\langle \sin\theta - 1, 0 \rangle \tag{39}$$

At the zenith (broadside) elevation scan angle, the steering function reduces to (40) – (41). The result (41) differs from that of (40) since the random variable $z_n = 0$.

$$\Psi_{Broadside}^{Sph}(\theta, \phi = 0°) = 2\pi\tilde{A}\langle \sin\theta, 0, \cos\theta - 1 \rangle, \qquad \Psi_{Broadside}^{Sph}(\theta, \phi = 90°) = 2\pi\tilde{A}\langle 0, \sin\theta, \cos\theta - 1 \rangle \tag{40}$$

$$\Psi_{Broadside}^{Cir}(\theta, \phi = 0°) = 2\pi\tilde{A}\langle \sin\theta, 0, 0 \rangle, \qquad \Psi_{Broadside}^{Cir}(\theta, \phi = 90°) = 2\pi\tilde{A}\langle 0, \sin\theta, 0 \rangle \tag{41}$$

Unlike previous work [21], the mean pattern contains multiplication amongst orthogonal solutions composed of an orthonormal steering vector set. Therefore, the mean pattern of a *CRA* and *SRA* proceeds upon non-linear solution sets. This result causes overwhelming difficulty in analysis when solving for mean peak and null locations. Hence, the alternative approach in this work follows similar to works of [3 – 4], [13], [15], and [21]. These unknowingly simplified the patterns of (33) – (34) to (42) – (43) where $\Psi = 4\pi A/\lambda \sin(\phi / 2)$. E.g., for small-angle approximations, Ψ becomes $2\pi A\phi / \lambda$. In other words, the dominant term of cos ϕ – 1, and sin ϕ is the latter term of the correct pattern calculations of (33) – (34). Thus, the expressions of (42) – (43) are not precise, but no loss in generality exists when locating mean peak and null locations (in a neighborhood of the mainbeam region). These are verified, as shown in Figure 19 (Figure 41 – 42 of [14]).

$$\bar{U}(\theta, \phi) \approx 1/N + (1 - 1/N)\left|3\,\mathrm{tinc}\Psi\right|^2 \tag{42}$$

$$\bar{U}(\theta, \phi) \overset{Cir}{=} 1/N + (1 - 1/N)\left|2\,\mathrm{jinc}\Psi\right|^2 \tag{43}$$

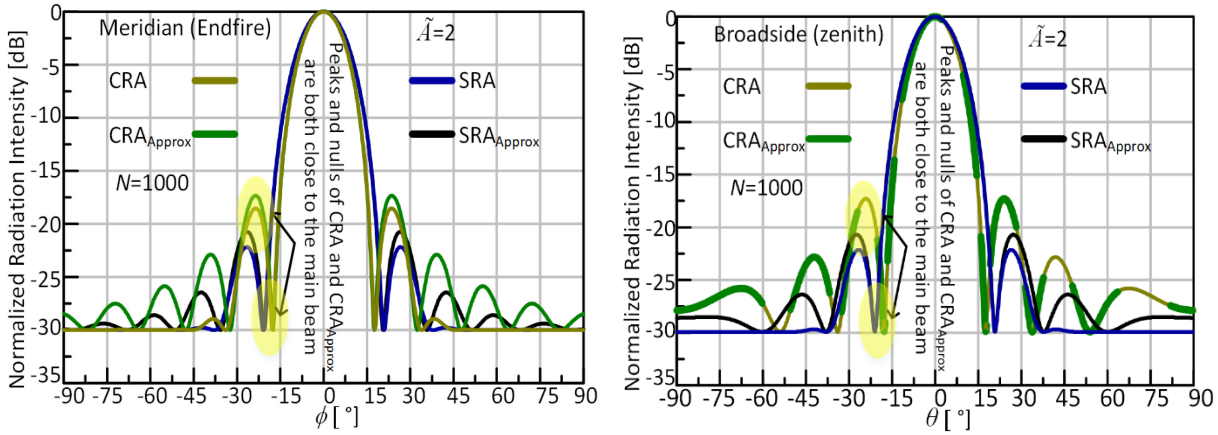

Figure 19. Analytical comparison of (33) – (34) and (42) – (43) at the meridian elevation angle (Figure 41 of [14]), left and zenith elevation angle (Figure 42 of 14]), right. The area in yellow shows a comparison of the first peak and null of (33) – (34) and (42) – (43).

2.8 ANALYSIS OF RADIATION FROM SUBARRAYS

Derivative topologies of the SRA and CRA, respectively, provide a shell annular random array (SARA) and circular annular random array (CARA). We assume that inner radius $A_{i,s}$ in (164) of [14]

converges in the limit to the outer radius $A_{o,s}$ such that either SARA (0, $A_{i,s}$, $A_{0,s}$) or CARA (0, $A_{i,s}$, $A_{0,s}$) has an area large enough to include at least N elements, where K elements are inside of the shell or ring and L elements are outside so that $K + L = N$.

Characteristic functions of the CARA and SARA were thoroughly derived in [14] and [22] and are shown in (44) – (45) for completeness with M=1 and illustrated in Figure 20. When multiple rings or shells are compounded as a function of M (the number of rings or shells), the kernel of these characteristic functions (46) – (47) can be found for each aperture radii factor to compound each subarray factor in its total pattern, broadening the effective null depth for a designed spatial angle. Examples of mean and numerical pattern comparisons are provided in Figure 21.

$$U_{av}(\theta,\phi) \overset{Ring}{\approx} U_{av}(\phi) \overset{CARA}{=} \frac{1}{K} + \left(1-\frac{1}{K}\right)\left|\frac{1}{M}\sum_{m=1}^{M} J_0\left(\tilde{A}_{o,s}^{(m)}\zeta(\phi)\right)\right|^2 \tag{44}$$

$$U_{av}(\phi) \overset{SARA}{\approx} \frac{1}{K} + \left(1-\frac{1}{K}\right)\left|\frac{1}{M}\sum_{m=1}^{M} \frac{3}{2}\left(\operatorname{sinc}\left(\tilde{A}_{o,s}^{(m)}\zeta(\phi)\right) - \operatorname{tinc}\left(\tilde{A}_{o,s}^{(m)}\zeta(\phi)\right)\right)\right|^2 \tag{45}$$

$$\tilde{A}_{o,s}^{(m)} = \lambda\left(m-1/4\right)\Big/2\sin\left(\phi^*\right),\ m=1,\ldots,M \tag{46}$$

$$\tilde{A}_{o,s}^{(m)} = \lambda(.875)\Big/2\sin\left(\phi^*\right),\ m=0, \qquad \tilde{A}_{o,s}^{(m)} = \lambda m\Big/2\sin\left(\phi^*\right),\ m=1,\ldots,M \tag{47}$$

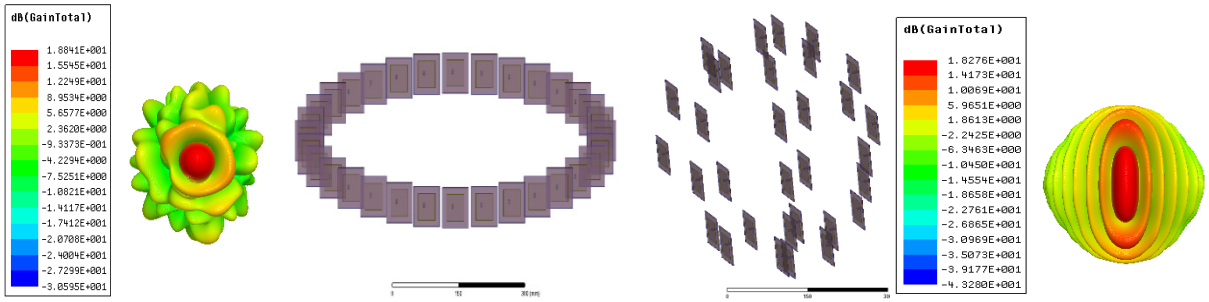

Figure 20. Computational HFSS simulations of thirty-two element patch configurations of a CARA (M = 1, A/λ=2.778, ϕ*=7.74°) – left and SARA (M = 1, A/λ = 1.69, ϕ* = 15°) – right.

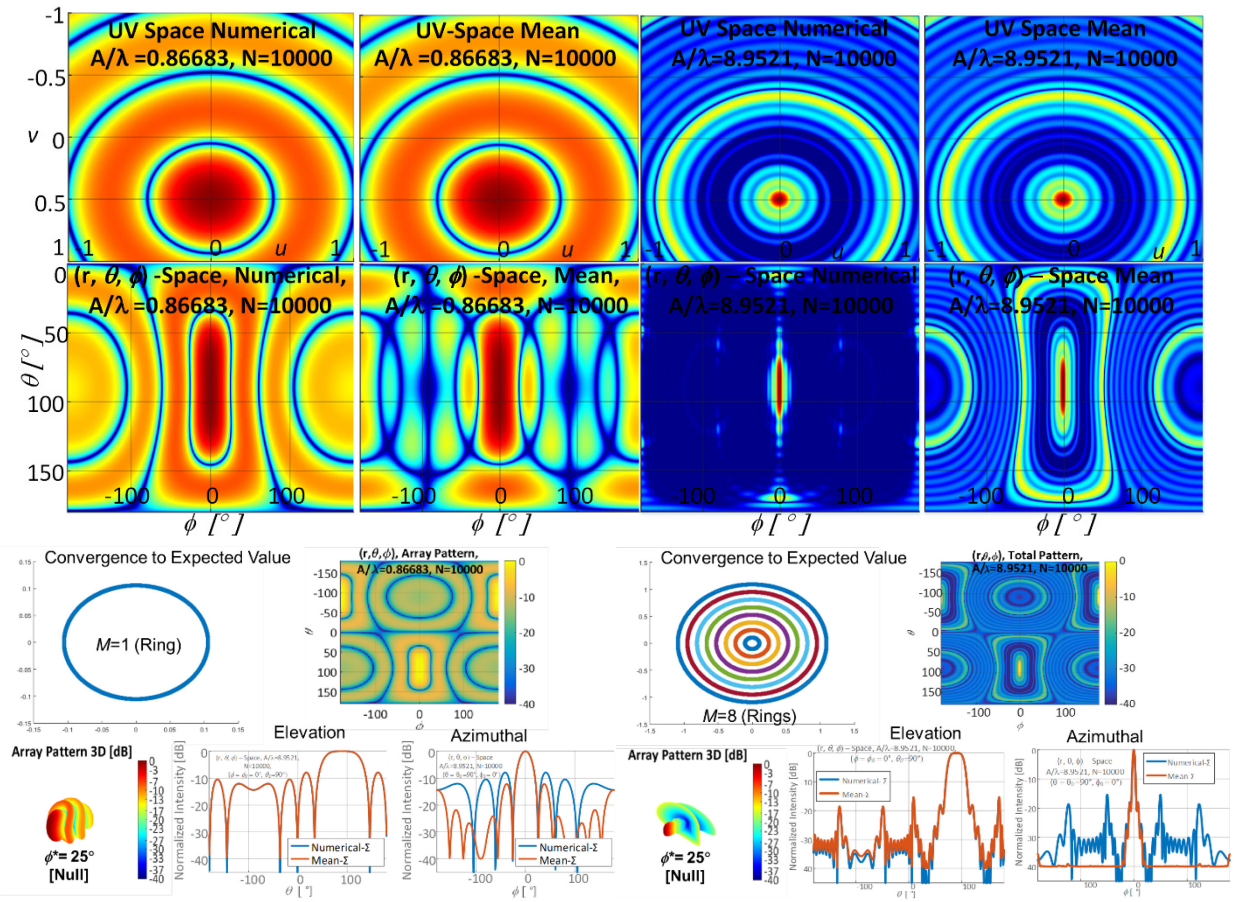

Figure 21. Computational simulations of a Cara (M=1, ϕ*=25°) with comparison its mean value (even-columns), angular space (second row), and UV-space (first row). A comparison of a singular ring Cara (M=1, ϕ*=25°) and (*M*=8, *ϕ**=25°) -right are provided on row three and four to demonstrate the convergence of the solutions.

A comparison of the distributed ring is provided in Figure 22 that null-steers at designed spatial angles $\varphi^* = \{3°, 4°, 5°, 6°\}$ by modulating its unit less or normalized aperture size $2A/\lambda = \{14.33, 10.75, 8.6, 7.17\}$. The scan is nullsteered in the azimuthal angle at endfire; however, the same result could be produced in the elevation angle using the same procedures described in [21] – [22].

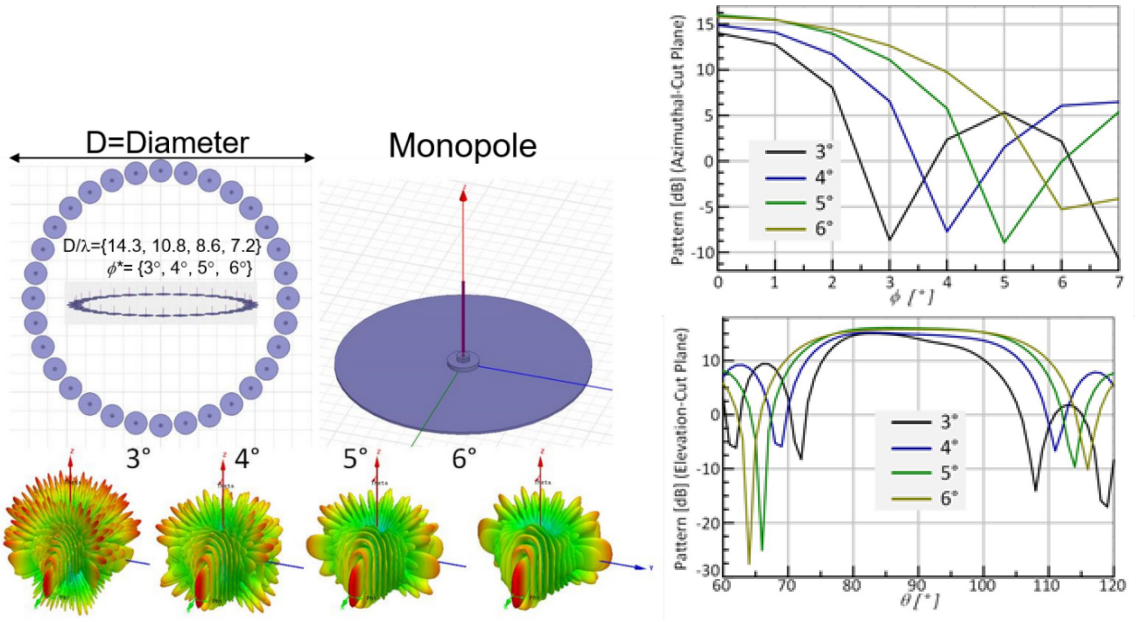

Figure 22. Incremental nullsteering sum beam results and comparisons using N = 32 monopole element distribution-top row. Computational meridian 3D patterns middle row and ϕ – cut plane bottom left; (θ – cut plane bottom right).

In Figure 23 – 25, simulated results demonstrate the null deepening for both the SARA and CARA topologies as the order of the subarray increases in angular space. A comparison of radiation patterns in *UV – space* is provided in Figure 26.

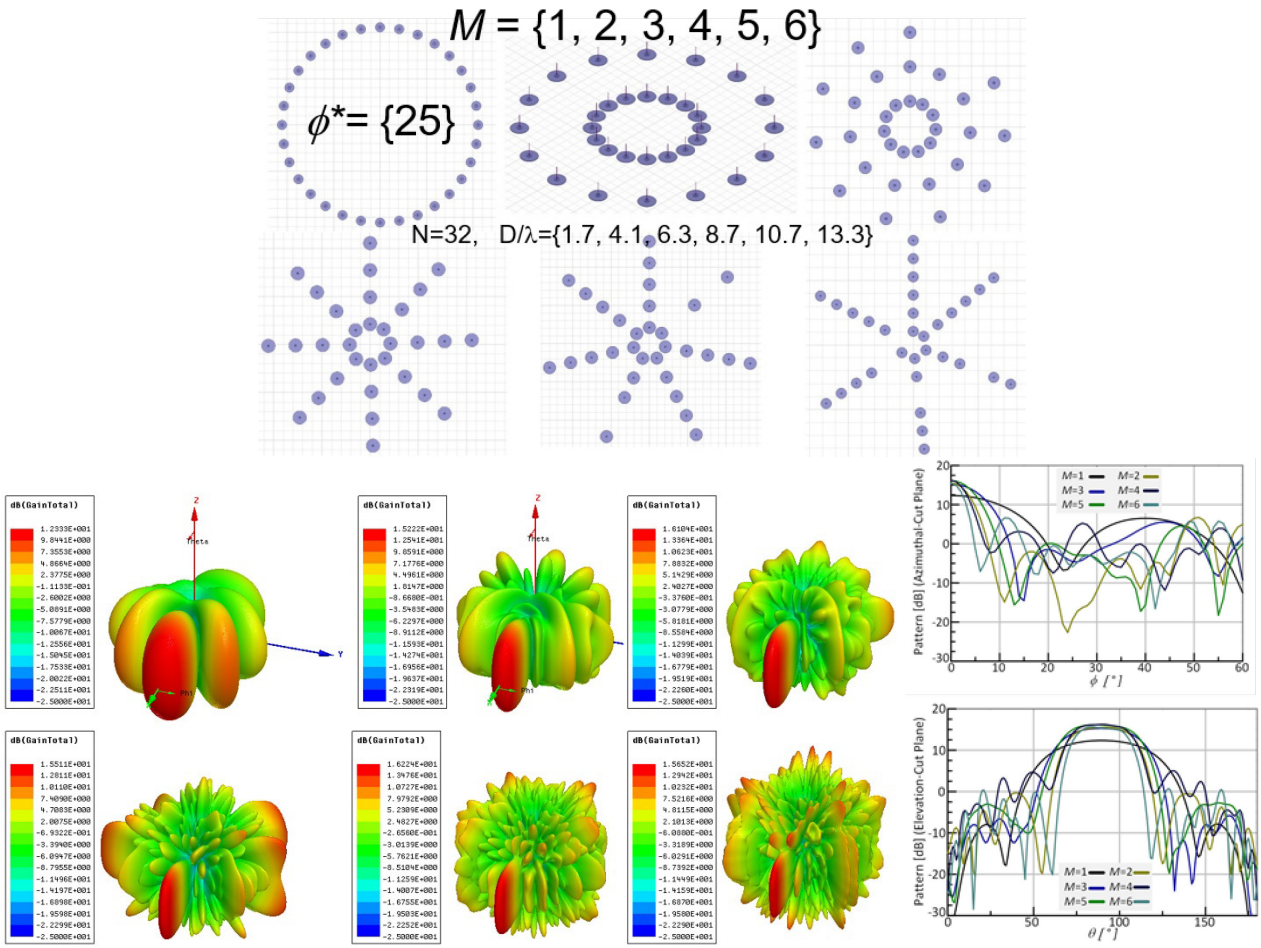

Figure 23. Incremental compound nullsteering (M = 1 – 6) results and comparisons using N=32 monopole element distribution-top row. Computational meridian 3D patterns middle row and ϕ – cut plane bottom row; θ – cut plane second from the bottom row.

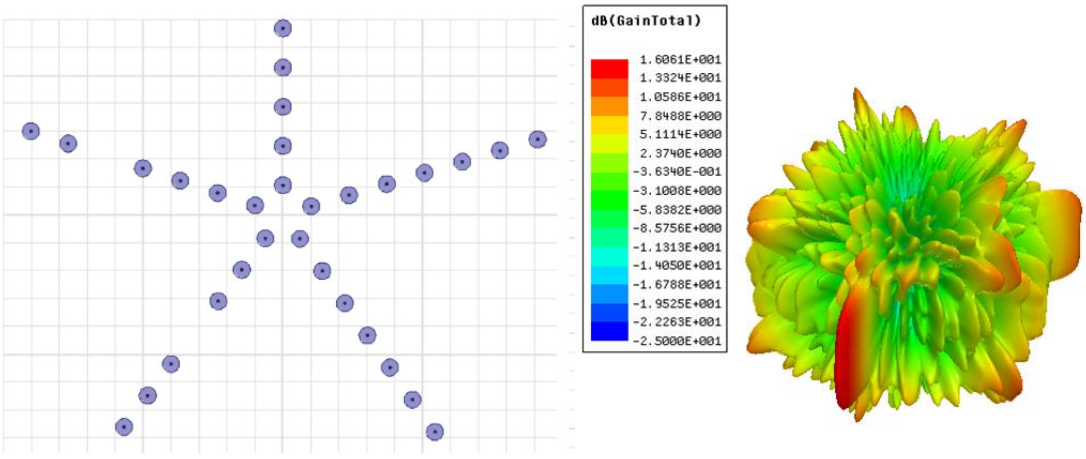

Figure 24. Incremental compound nullsteering (M = 7) designs using N = 32.

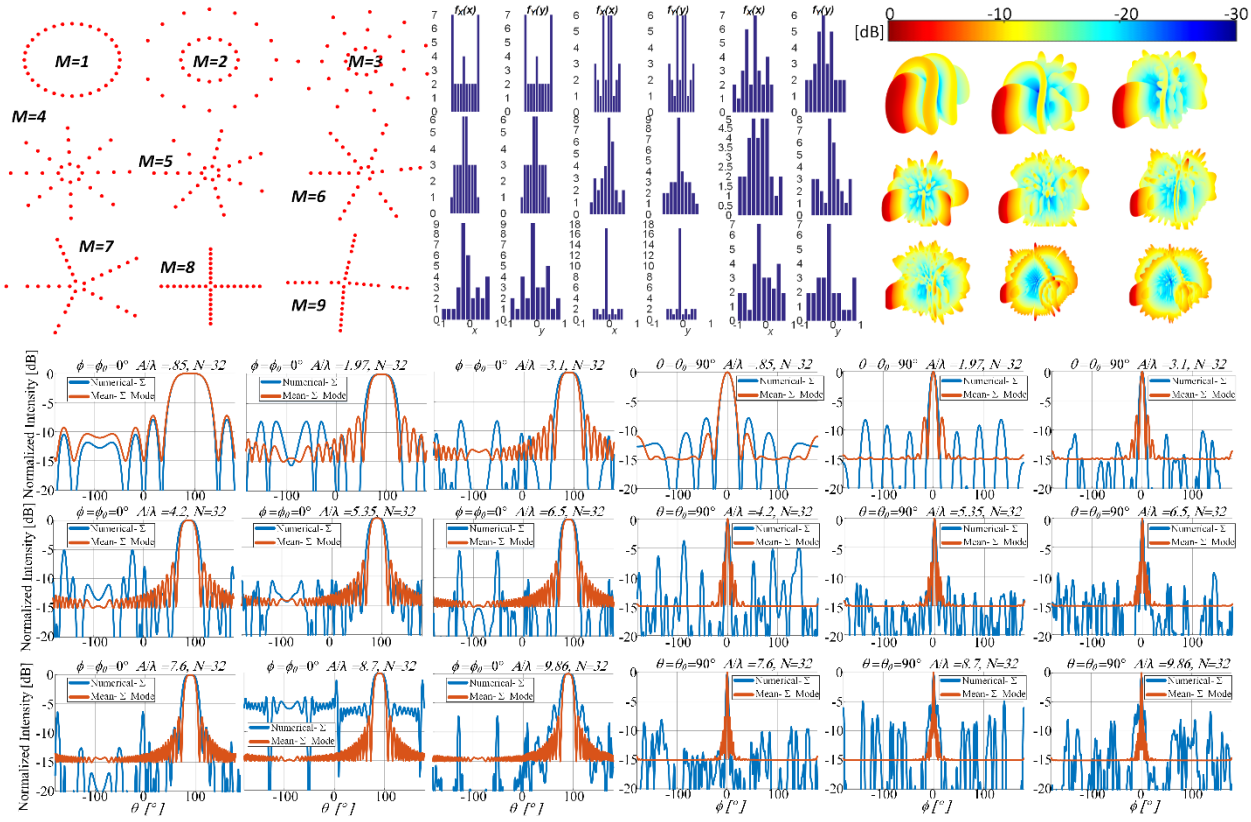

Figure 25. Compound nullsteering (M = 1 – 9) simulated designs with N = 32. Element distributions are provided top – left, probability distributions top – middle, three-dimensional patterns, top – rights. The phi – cut plane (right-side) and theta (left side) cut plane is provided on the bottom three rows.

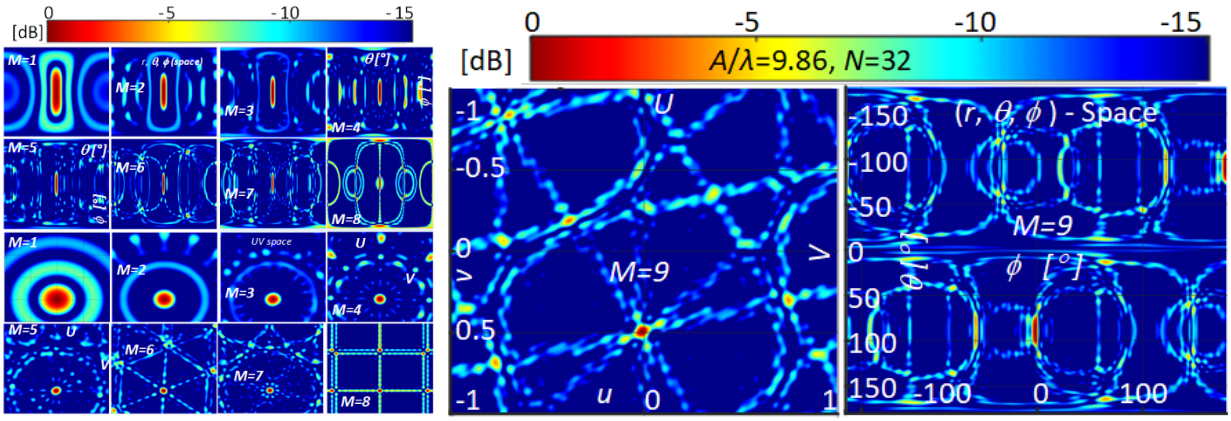

Figure 26. Comparisons of incremental compound nullsteering *CARA* angular (r, θ, ϕ) and UV pattern simulations, M = 1 – 9, with ϕ^* = 25°.

Measured and simulated results are compared in Figure 27 – 28 and validate the feasibility of beamsteering deep, broad nulls at precise locations, as demonstrated in Figure 26. [21] – [22]

Use of a planar thirty-two element CRA (picture not included) populated by microstrip patched operating in the 2.4 GHz ISM band, and its ability to act as a partitioned aperture for simultaneous sum-difference pattern generation. This distribution was investigated experimentally by partitioning a

CRA with A = 35 cm. into a set of interior and exterior (perimeter) groups of sixteen elements. Figure 29 includes measured results for the full set of possible permutations to demonstrate combined even and odd mode behavior. The black and grey color of the inset circular diagram indicates the sum and difference modes of the partition, respectively, where the "+" and " – " illustrates the in-even and odd phasing, respectively, applied to each half of the interior and perimeter sub-arrays. Each sub-array was measured with non-active elements replaced by matched loads except for the full-sum and full-difference modes. It is observed that well-behaved sum and difference beam patterns may be obtained by either even or odd (anti-modal) types of distributions, which demonstrates the applicability and the use of the CRA as a partitioned aperture for simultaneous sum-difference pattern generation.

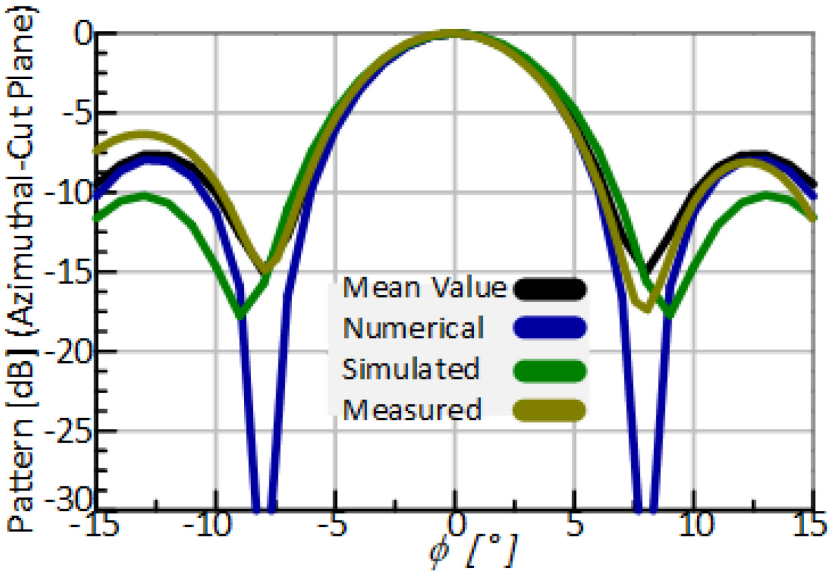

Figure 27. Ring distributed monopole array pattern comparison of the theoretical-mean value, numerical-MATLAB, simulated-HFSS and measured results (A/λ = 2.77, ϕ^*= 7.74, N = 18 and M = 1).

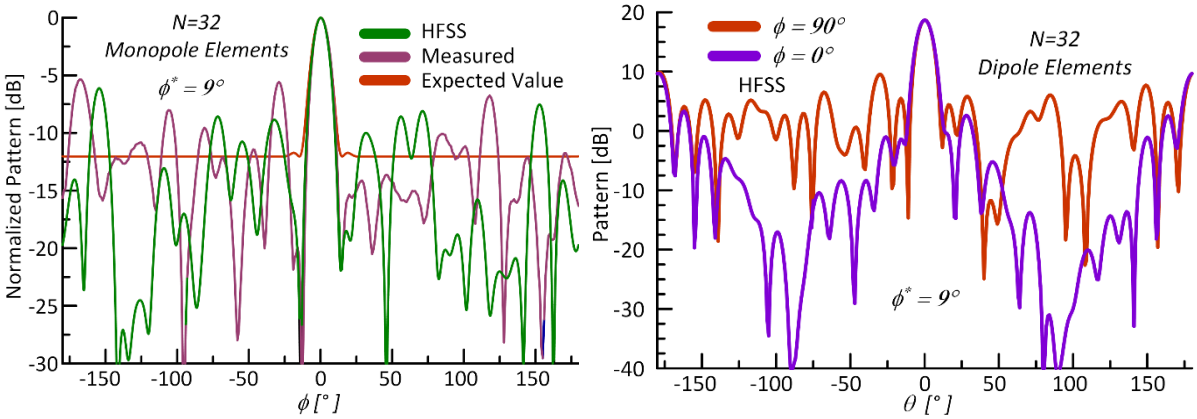

Figure 28. SARA steered at the meridian elevation angle θ_0 = 90°, ϕ_0 = 0° (ϕ^*=9.0°, 16 monopoles, A / λ = 2.77 and M=1); test setup (left), and SARA steered at the zenith elevation angle θ_0 = 0°, ϕ_0 = 0° (ϕ^* = 9.0°, 32 dipoles, A / λ = 2.77 and M = 1), right.

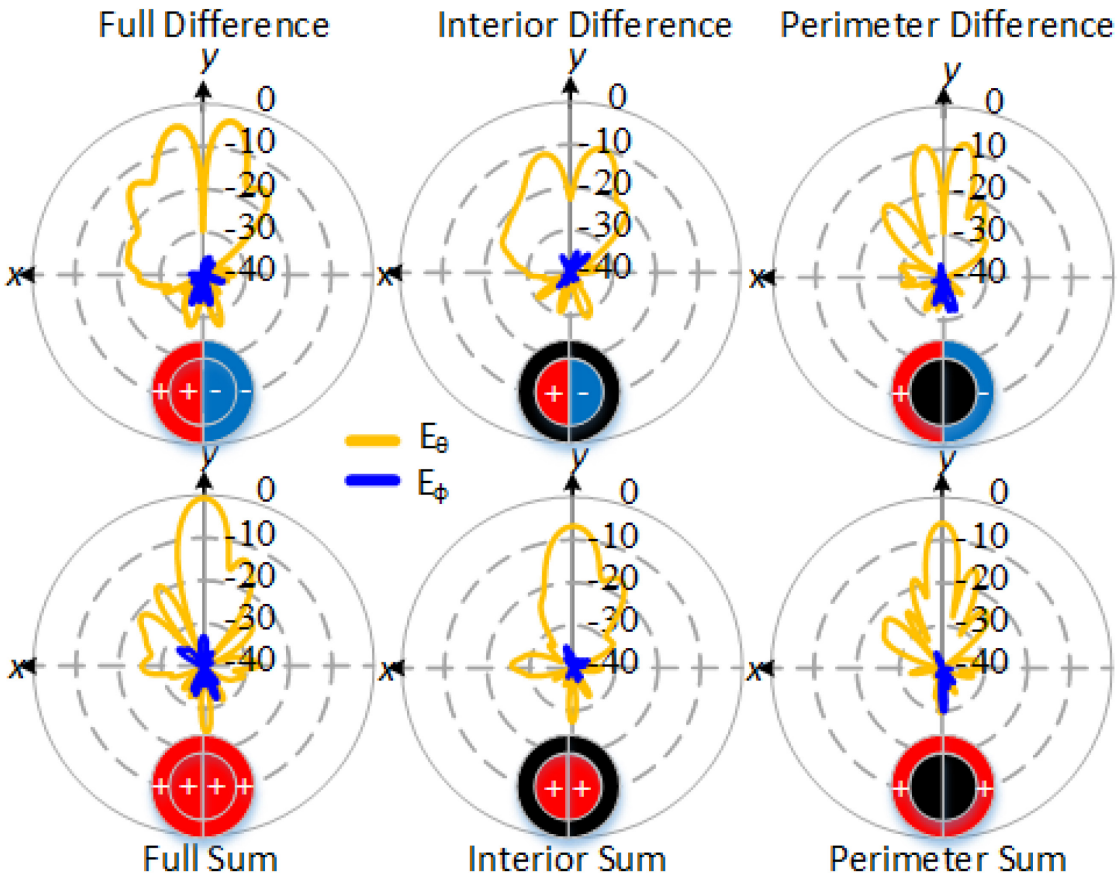

Figure 29. Measured CRA aperture in four phasing scenarios: full sum (lower-left), full difference (top-left), interior sum (lower-middle) with exterior difference (top-middle), exterior sum (lower-right) with interior difference (top-right).

2.9 DIRECTIVITY IN PSI SPACE

In ψ - space, a linear, circular, and spherical random array all look and provides an effective aperture size $D = 2A$. This result is not the case in (r, θ, ϕ) – space where results are provided at the end of chapter III, section l.

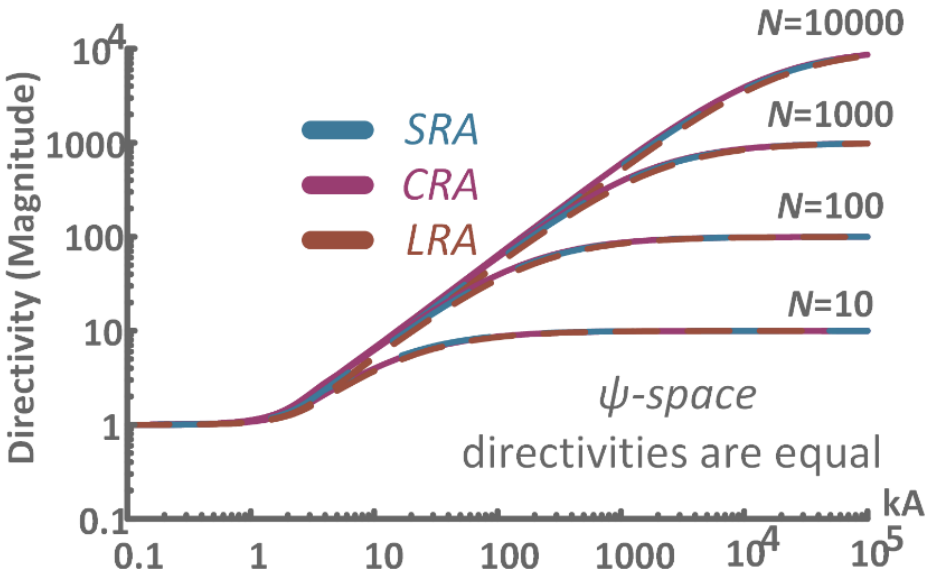

Figure 30. Directivity in Ψ-space is approximately equal for all *n*.

$$\bar{D}_0(kA;n) \triangleq 2\frac{1}{\frac{2}{N}+\left(1-\frac{1}{N}\right)\int_{-1}^{1}\mathrm{Sinc}(kA\psi;n)^2\,d\psi} = \frac{N}{1+(N-1)\,{}_2F_3\left(\left\{\frac{1}{2};\frac{n+1}{2}\right\},\left\{\frac{3}{2};\frac{n+1}{2};n+1\right\};(-kA)^2\right)} \quad (48)$$

The maximum radiation intensity corresponding to the isotropically radiated power is equal to the power accepted (input) by the antenna divided by 2 (i.e., the normalization from the range of ψ). Moreover, the subtrahend hypergeometric function in the denominator of (48) transcendentally decays to 0 as $kA \to \infty$. Hence, the directivity is generally less than N but approaches N as kA increases. This result coincides with the previous statement that the main beam narrows, and directivity increases with increasing aperture size.

This page is intentionally blank

3. STATISTICAL ANALYSIS

3.1.1 Explanation of the Physical Process

Another way of picturing the results of (26) can be illustrated using Huygens principle. For example, the superposition of sources along a continuous aperture can be thought of as a continuous number of sources that create the wavefront some distance away. Analogously the aperiodic array is to be a discrete number of sources, as illustrated in Figure 31. For instance, when $N \to \infty$ in the discrete solution converges of (26) converges to a continuous aperture solution. Hence, the difference in relations exists within the pedestal ($1/N$) and will differ from the continuous aperture distribution because of the element's physical size constraints.

Antenna arrays are nothing more than an aperture excited at points of localized zones. These spaces consist of discrete radiators or receivers called elements, and the strength amplitudes are I at the located positions x. Moreover, the general aperture excitation may be written as

$$I(x) = \sum I_n \delta(x - x_n) \tag{49}$$

One may take the fast Fourier transform of the common distributions of a ring, line, circle, and sphere and even compare it to the expected value, as illustrated in Figure 32.

3.2 PROBABILITY MOMENTS OF THE MEAN VALUED ARRAY FACTOR AND MEAN VALUED RADIATION PATTERN

3.2.1 Array Factor Moments

In probability theory, four moments can generalize the array factor being the mean (25), variance (50), skew (51), and kurtosis (52) or excess kurtosis (53).[3] Moreover, an example of these moments (54) is shown in Figure 35 for n =0 – 3, representing the pattern behavior of a ring, line, circle, and spherical distribution.

[3] A proof of the variance relations of (50) is provided in [13] and [18].

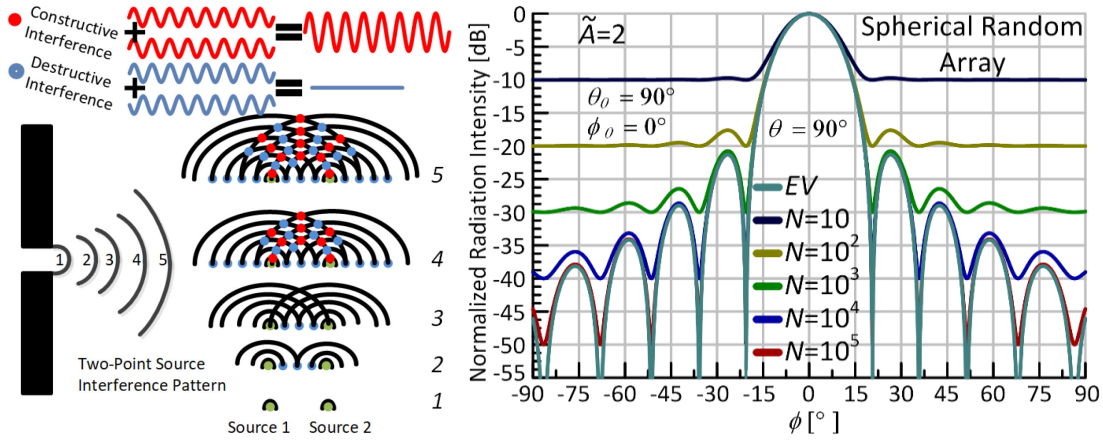

Figure 31. Superposition diagram (left) converges to a continuous aperture distribution as $N \to \infty$ (right).

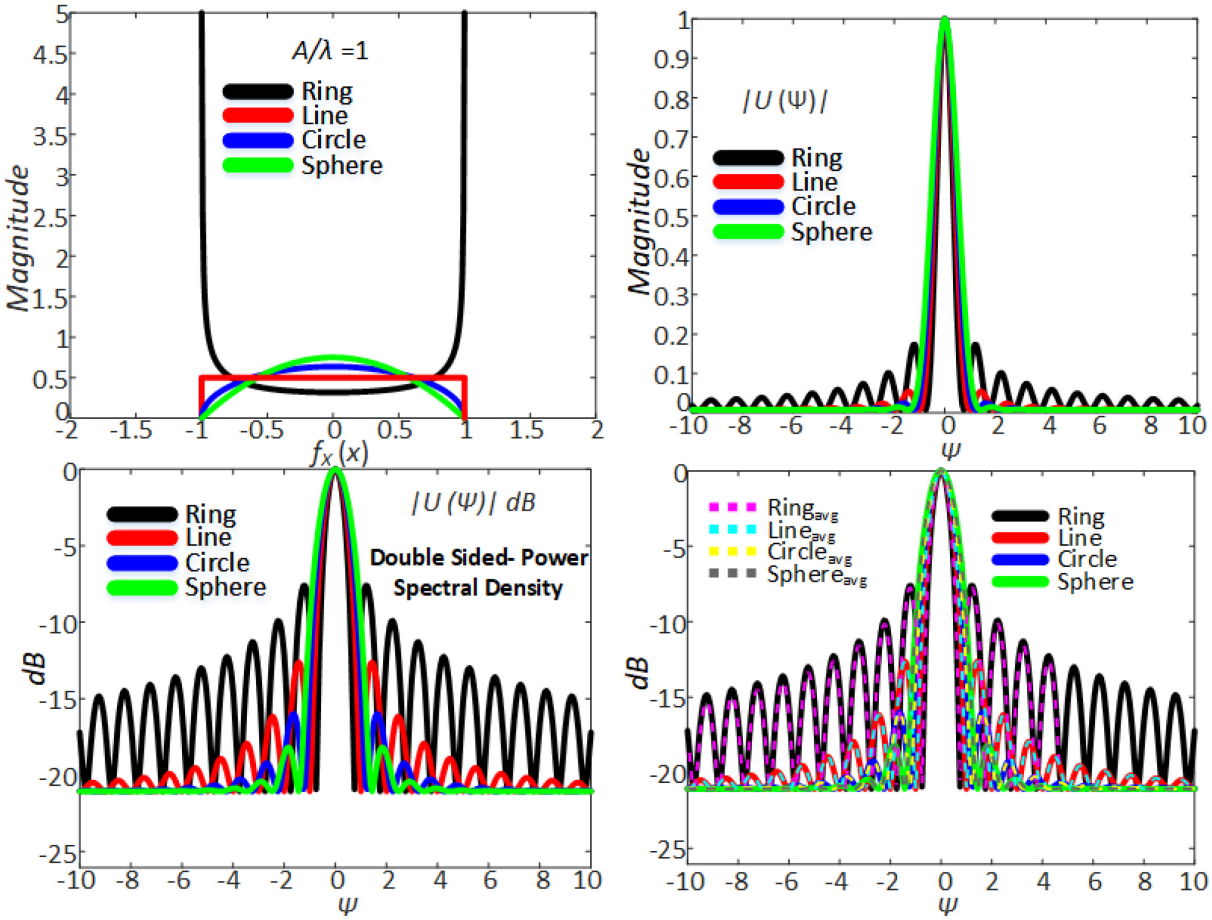

Figure 32. Comparison of the Fast Fourier Transform and Expected value of the common distributions, n = 0 ring, n = 1 line, n = 2 circle, and n = 3 sphere.

$$\bar{\sigma}_S^2 = 1/2\left[1+\Lambda(2\Psi)\right]-\Lambda(\Psi)^2, \qquad \bar{\sigma}_D^2 = 1/2\left[1-\Lambda(2\Psi)\right], \qquad \bar{\sigma}_{F=S+D}^2 = 1/N\left[1-\left|\Lambda(\Psi)\right|^2\right] \tag{50}$$

$$\mu'_{3,\mathrm{S}} = 1/4\left[\Lambda(3\Psi)+3\Lambda(\Psi)\right] \tag{51}$$

$$\mu'_{4,\mathrm{S}} = \left[3+\Lambda(4\Psi)\right] \tag{52}$$

$$\mu'_{4,\mathrm{S}} = 1/4\left[\Lambda(4\Psi)\right] \tag{53}$$

$$\begin{aligned}
&\mu'_{N,\mathrm{S}} = \int_{-1}^{1}\cos x^N f_S(x;n)\,dx, \mu'_{N,\mathrm{D}} = \int_{-1}^{1}\sin x^N f_D(x;n)\,dx, \mu'_{1,\mathrm{S}} = \Lambda(\Psi), \mu'_{1,\mathrm{D}} = 0, \mu'_{1,F} = \mu'_{1,\mathrm{S}} + \mu'_{1,\mathrm{D}} = \Lambda(\Psi),\\
&\mu'_{2,\mathrm{S}} = \frac{1}{2}\left(1+\Lambda(2\Psi)\right), \mu'_{2,\mathrm{D}} = \frac{1}{2}\left(1-\Lambda(2\Psi)\right), \mu'_{2,F} = 1, \mu'_{3,\mathrm{S}} = \frac{1}{4}\left[\Lambda(3\Psi)+3\Lambda(\Psi)\right], \mu'_{3,\mathrm{D}} = 0,\\
&\mu'_{4,\mathrm{S}} = \frac{3+4\Lambda(2\Psi)+\Lambda(4\Psi)}{8}, \mu'_{4,\mathrm{D}} = \frac{3-4\Lambda(2\Psi)+\Lambda(4\Psi)}{8}, \mu'_{3,F} = \frac{1}{4}\left[\Lambda(3\Psi)+3\Lambda(\Psi)\right], \mu'_{4,\mathrm{F}} = \frac{1}{4}\left(3+\Lambda(4\Psi)\right)
\end{aligned} \tag{54}$$

It is not illustrated here, but the kurtosis diverges to infinity near the origin. The sharp peak indicates the mainlobe region; otherwise, there is a settlement of the kurtosis outside of this region (similar to a uniform distribution). This result describes the peak sidelobe level (PSLL) settlement, average sidelobe level (ASLL), and gain. On the other hand, the skew of the characteristic function is conversely defined as the expected array factor. E.g., when the mean array factor is positive, the skew is negative and vice versa. Thus, this describes positively and negatively charged lobes.

Re-observing the variance of the even and odd modes of the array factor, one can observe that the random array pattern may be broken up into three regions as illustrated in;

I. The first region is to the controlled or mainlobe region and equals $1/N$ in its neighborhood

II. The second region is the transition region, in which the sidelobe pattern degenerates but yet closely matches the design pattern (i.e., the first sidelobe, sometimes second, and on occasion tertiary lobes).

III. The third and final portion is the random portion (three dB sidelobe region), in which the sidelobe statistics applied in this section closely approximate to those of the random array.

Accordingly, it is key for the array designer to predict the maximum peaking sidelobe behavior but should always consider the main beam deterministic (and the first sidelobe). Also, this validates that the addition of two random variables gives the mean-variance of the radiation pattern. This type of method to find the variance is similar to applications such as *I-Q* modulation, the study of noise, and radar imaging where the joint pdf is given. Lastly, a notional example of the radiation pattern statistics is shown in Figure 33 for completeness.

In the 3dB sidelobe region far from the mainbeam $\Psi >> \Psi_0$, the variance converges to one meaning, the target is in the total random region of the beam pattern and cannot be fully resolved or tracked. An illustration is provided in Figure 34, defined by equations (55) and (56). It is also worth noting that the variance of the capture region is independent of *N,* where the capture angle Ψ is equal to the inverse $\mathrm{CoTanc}^{-1}(\mathrm{CoTanc}(\Psi))$ (57).

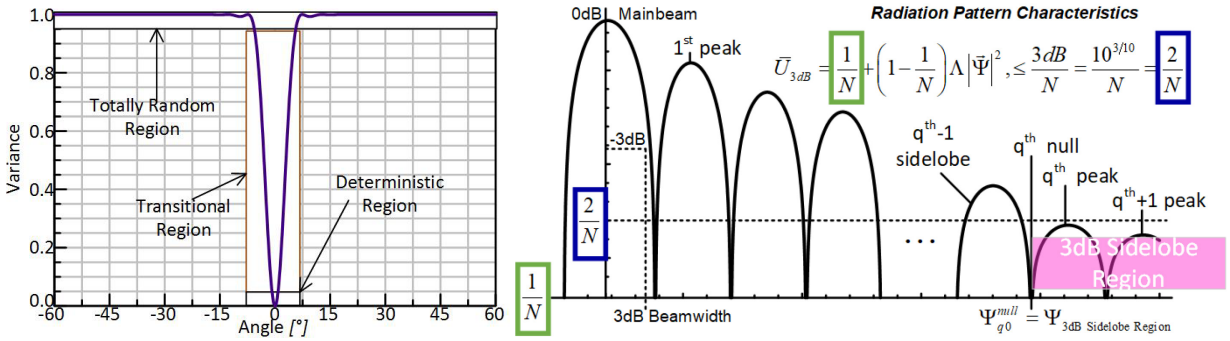

Figure 33. Probability moments of the array factors of a ring, line, circle, and spherical distributions, (left) and notional example of the monotonically decaying radiation pattern (right) [3].

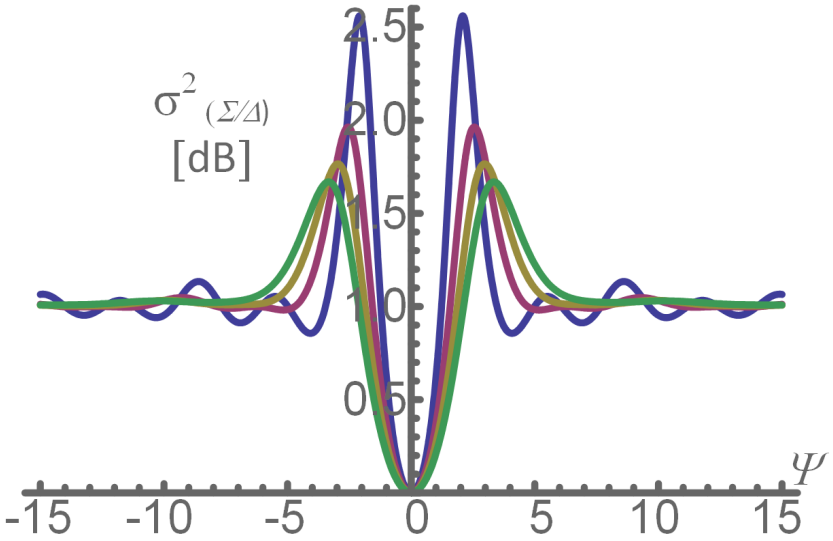

Figure 34. Total even / odd variance. Variance =0 at $\Psi_0 = \delta_0 = 0°$ [31], which means the target is fully resolved and deterministically tracked.

$$\sigma_S^2(\Psi)/\sigma_D^2(\Psi) = \left(1-\mathrm{Sinc}_n^2(\Psi)\right)/\left(1-\mathrm{CoSinc}_n^2(\Psi)\right) = \mathrm{CoTanc}_n^2(\Psi) \tag{55}$$

$$\mathrm{CoTanc}_n(\Psi) = \Delta/\Sigma = \mathrm{CoSinc}_n(\Psi)/\mathrm{Sinc}_n(\Psi) = H_{n/2}(\Psi)/J_{n/2}(\Psi) \tag{56}$$

$$\Psi = \mathrm{CoTanc}_n^{-1}\left(\mathrm{CoTanc}_n(\Psi)\right) \tag{57}$$

3.2.2 Power Pattern Moments

The variance of the mean power pattern (58) of the received signal power is shown below as $N \to \infty$ of Figure 35.

$$\begin{aligned}\sigma_U^2 &= Var[U] = 4\sigma_S^2\Lambda_S^2 + 2\sigma_S^4 + 2\sigma_D^4 \\ &= 2\Lambda(\Psi)\left(\Lambda(\Psi)+2\Lambda(\Psi)\right)/N + \left(\Lambda(\Psi)+\Lambda(2\Psi)\right)/N^2\end{aligned} \tag{58}$$

Finally, higher-order moments (skew and kurtosis) are not shown, and no loss in generality occurs here either due to their complexity in the calculation. However, they are likely to resemble closely to the statistics of the array factor shown previously.

IV.

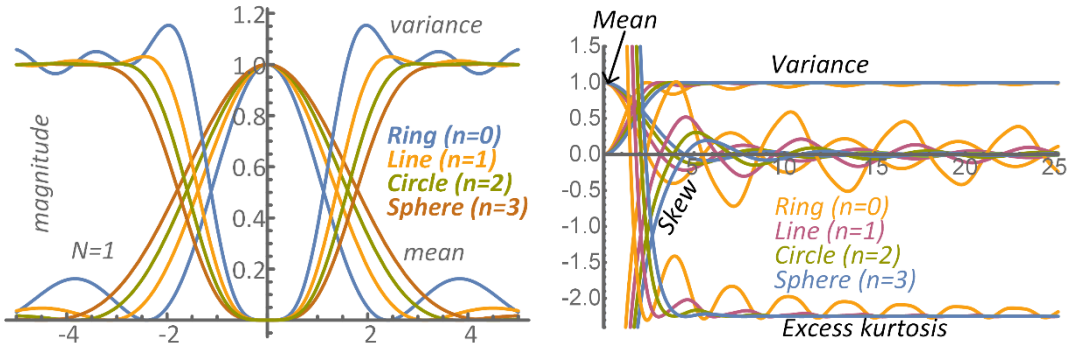

Figure 35. Comparisons of the radiation pattern variance and mean power (left) and probability moments of the array factor (right).

3.3 ARRAY FACTOR PROBABILITY AND JOINT DENSITY FUNCTIONS

3.3.1 Joint Distribution Function of the Array Factor Amplitude and Phase

When analyzing the array factor outside of the main beam region, it is understood that the even and odd modes' variances (50) must be equal $\sigma_S^2=\sigma_D^2=1/(2N)$, for otherwise, the mean square deviations would be functions of the arbitrary choice of coordinates. Thus, the pdf for the real component is

$$w_1(\mathrm{S};\Psi)=\left(1/\sqrt{2\pi}\sigma_S\right)e^{\left(-(S-\bar{S})^2/(2\sigma_S^2)\right)} \tag{59}$$

where the imaginary component has the same form replacing the variable S with D. The joint probability density function is their product because the quadrature Gaussian components are uncorrelated

$$f_{\mathrm{S,D}}(\mathrm{S},\mathrm{D};\Psi)=\frac{1}{2\pi\sigma_S\sigma_D}\exp\left[-\frac{1}{2}\left[\left(\frac{S-\bar{S}}{\sigma_S^2}\right)^2+\left(\frac{D-\bar{D}}{\sigma_D^2}\right)^2\right]\right] \tag{60}$$

3.3.2 Probability Distribution Function of the Array Factor Amplitude

To obtain the pdf of the array factor $w_1(|F|;\Psi)$, one begins by simplifying (60) by assuming the region of interest resides in the 3dB sidelobe region. Hence, an equal variance of S and D's quadrature components can be made similar to [32 – 37]. Next, one converts (60) to polar coordinates (61) such that $|\mathrm{F}|=\sqrt{(S^2+D^2)}$ and $\vartheta=\tan^{-1}(D/S)$ and are the amplitude and phase of the array factor, respectively. Finally, one integrates with respect to ϑ to yield $w_1(|F|)$ of (62).

$$\Pr\left[U(\Psi)\geq U_0\right]=\Pr\left[\left(\left(S^2+D^2\right)/N\right)\geq U_0\right]=\Pr\left[\sqrt{S^2+D^2}\geq\sqrt{NU_0}\right]$$
$$=\int_{\sqrt{NU_0}}^{\infty}\int_{-\pi}^{\pi}\frac{1}{2\pi\sigma_S\sigma_D}\exp\left[-\left|F\cos\theta-\bar{S}\right|/2\sigma_S^2-F^2\sin^2\theta/2\sigma_D^2\right]FdFd\theta \tag{61}$$

$$w_1\left(|F|\right)=\left(\frac{2|F(\Psi)|}{\sigma^2}\right)e^{\left(-\frac{|F(\Psi)|^2+|\bar{F}(\Psi)|^2}{\sigma^2}\right)}I_0\left(\frac{2F(\Psi)\bar{F}(\Psi)}{\sigma^2}\right)$$
$$=Q\left(2|F(\Psi)|/\sigma^2,2|F(\Psi)|/\sigma^2\right)\neg\sigma^2=\sigma_S^2+\sigma_D^2 \tag{62}$$

The special function I_0 in (62) is the modified Bessel function of the first kind of zero order. This result is known as the complementary cumulative distribution function (CCDF). Moreover, at angles sufficiently far from the main beam such that $|\bar{F}(\Psi)| \ll 1/N$ (3dB sidelobe region), the angular dependency is eliminated and reduces to the Rayleigh distribution [3 – 4], and [19 – 20] of (63) and (64) far away from the main beam such that $\sigma^2 = 1/N$. An illustration of (62) – (64) is provided in Figure 36.

$$w_1\left(|F|\right)=2|F|/\sigma^2\,e^{\left(-|F|^2/(\sigma)\right)}. \tag{63}$$

$$w_1\left(|F|\right)=2N|F|e^{\left(-N|F|^2\right)}. \tag{64}$$

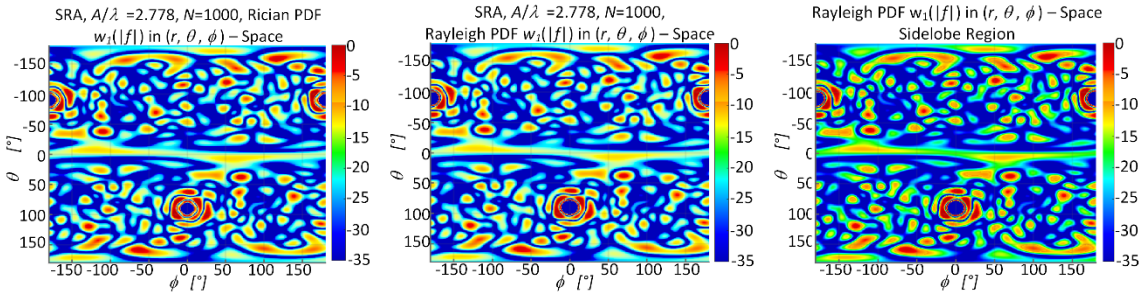

Figure 36. Comparison of the probability distribution of (62)– left and (63) – middle and (64) – right in angular space of an SRA, N=32, A/λ = 2.778.

The most noticeable differences in Figure 36 display a slight deviation in the peak sidelobe behavior in the region of the main beam ($\theta_0 = 90°$, $\phi_0 = 0°$) of (62) versus (63) – (64). Results of (63) – (64) show less deviation amongst its pattern behavior, showing that no loss in generality is considered from approximating (63) to (64).

An alternate form is also useful. We let f be the unnormalized amplitude of the complex radiation pattern of an N-element array. Then $f = N|F|$ and for large Ψ, $\sigma^2 = 1/N$. Hence, the pdf of f in the sidelobe region is found from the relation

$$w_1(f)=2f/N\,e^{-\left(f^2/N\right)}\left[\text{since }\left(dA/d|F|\right)^{-1}=1/N\right] \tag{65}$$

The RMS value of f is $\sqrt{N}$. The modal point of the distribution occurs at $f=\sqrt{(N/2)}$ shown by the sketch of Figure 37.

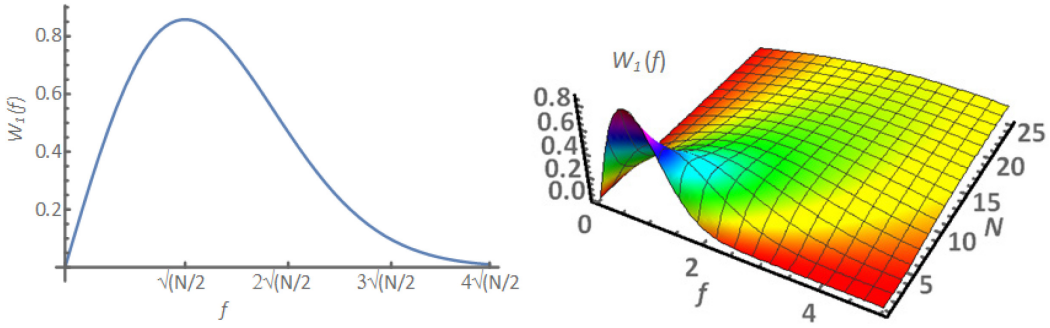

Figure 37. The probability distribution function of the N – element unnormalized complex radiation pattern amplitude.

Moreover, this represents the initial step in the development of a statistical sidelobe theory similar to the approach of historical work done in [20], [26], and [32 – 37]. It is the pdf of the amplitude of a random sample of an array's side radiation pattern with randomly selected element locations.[4] However, at angles close to the main lobe, this result no longer pertains; instead, $w_1(f)$ becomes a function of $\bar{F}(\Psi)$ and its joint distribution function (60).

Also, a result free of the element location distribution is highly desirable for its generality; strictly speaking; however, $w_1(f)$ pertains only in the restricted region that $|\bar{F}(\Psi)| \ll 1/N$. It is useful over a far more extensive angular region. This result is because the most important statistic of the sidelobe region is the peak value. It is shown later that the peak sidelobe is the order of 10 dB larger than the average sidelobe. Hence the design pattern $|\bar{F}(\Psi)|$ tends to become confused with the random pattern when $|\bar{F}(\Psi)|^2$ approaches $10/N$ and is submerged within it when it is several decibels smaller. For a 100-element array, this occurs by the second sidelobe of a uniform distribution of elements and by the first sidelobe of most spatial tapers. More comprehensive examples of the three dB sidelobe region in angular space can be found in [3 – 4]

[4] Note that the pdf of the element location does not affect the pdf of the amplitude of the array factor. This surprising result is due entirely to the assumption that Ψ is sufficiently large for the design pattern, which is the Fourier transform of the pdf of element location, to become submerged in the random pattern.

This page is intentionally blank.

4. PEAK SIDELOBE ESTIMATOR B

To prove a random array is free of grating lobes(given a sufficient number of radiators), one must find a distribution relating to the sidelobes' maximum output power. This type of work is provided in papers from [3 – 4] for planar *CRA's* and dates back to a very classic paper from Donovito [32 – 33] for linear random arrays. Additional classical texts discussing the distribution of peak sidelobes for *LRA's* have arisen from these earlier works and can be found in [19 – 20], [26], and [32 – 36], which include situations of non-isotropic elements or non-stationarity [37 – 38]. Moreover, for clarity, this section follows similarly to work presented by [3 – 4], [14 – 15], and [32] ends by setting up the fundamental limits of a uniformly distributed *SRA* with isotropic elements, behaving stationary.

4.1 3DB SIDELOBE REGION

The simplified distribution becomes readily tractable for the spatial region in which the mean value of the array factor is assumed zero. This result is greatly dependent upon the number of antennas present, and if N increases, the mean value increases, and the mean-variance goes to zero. Ideally, this would be the case, but a low number of elements might persist in practice. Since this may very well hold true, the *3dB sidelobe region* is re-examined to redefine the necessary confidence interval.

In [3 – 4] – [14 – 15], the *3dB sidelobe region* is defined to satisfy the condition (66). This term can be rewritten (67) by adding the variance of the corresponding random variables S and D.

$$NU_{av}\left(\Psi\right) \le 2 \tag{66}$$

$$Var\left(S\right)+Var\left(D\right)+\left|E\left[S\right]\right|^2+\left|E\left[D\right]\right|^2 \le N\bar{U}\left(\Psi\right) \le 2 \tag{67}$$

Given the inequality of (67) the average power pattern is bounded to that of (68). This result shows that the mean 3dB sidelobe region's square is bounded by unity when N is large. Additionally, the result also shows that the mean does not grow unbounded with the number of antenna N, similar to [3].

$$\left|E\left[U\right]\right|^2 \le 1/\left(1-1/N\right) \tag{68}$$

4.2 AUTO-COVARIANCE

The goal is to calculate the autocovariance of Σ_{SS} and Σ_{DD}. This result provides characteristics of peaking sidelobe behavior of random arrays. Far from the main beam region, we determined a region called the 3dB sidelobe region. The autocorrelation (autocovariance) function is applied

$$E\left[S\left(\Psi_1\right)-\Lambda\left(\Psi_1\right)\right]E\left[S\left(\Psi_2\right)-\Lambda\left(\Psi_2\right)\right]=\left(1-\frac{1}{N}\right)\Lambda\left(\Psi_1\right)\Lambda\left(-\Psi_2\right)+\frac{1}{N}\Lambda\left(\Psi_1-\Psi_2\right) \tag{69}$$

Assuming the overall process is wide-sense stationary (large Ψ_1 and Ψ_2) this simplifies as

$$\approx \Lambda\left(\Psi_1-\Psi_2\right)/2N \tag{70}$$

Mathematical results of this provide a probability bound for all angles within the 3dB non-peaking sidelobe region rather than at a single angle. Hence, the spacing for independence between samples is $\Psi = \Psi_c$ for which the correlation is zero. Hence, $\Psi_c = \lambda / 2A$ and $n = 2A/\lambda\,(1+|\Psi_0|)$. It should be noted that the number of independent samples in the pattern varies from $4A/\lambda$ at the main beam region to $2A/\lambda$ in the sidelobe region. The length of the array is the dominant factor in units of wavelength. The beam steering angle only secondarily influences the array parameter.

4.3 CROSS-COVARIANCE, JOINT MEAN AND PATTERN COVARIANCE

For completeness in analysis, the cross-covariance is easily shown to equal zero below

$$\begin{aligned} &E\left[S(\Psi_1)-\Lambda(\Psi_1)\right]E\left[D(\Psi_2)-\Lambda(\Psi_2)\right] \\ &=\left(1-\frac{1}{N}\right)\Lambda_E(\Psi_1)\Lambda_D(-\Psi_2)+\frac{1}{N}\Lambda_{SD}(\Psi_1-\Psi_2) \\ &\neg\Lambda_{SD}(\Psi)=E[SD]=\frac{1}{N}\int_{-1}^{1}\int_{-1}^{1}\cos(\mathrm{X}\Psi)\sin(\mathrm{X}\Psi)d\mathrm{X}d\mathrm{X} \\ &=E[SD]=E[DS]=E[S]E[D]=0 \end{aligned} \tag{71}$$

For even distributions of $E\,[\,D\,] = 0$. Hence, this completes the joint mean and covariance matrix

$$\left(\vec{U}_{\mathrm{S,D}}=\begin{bmatrix}\vec{S}\\ \vec{D}\end{bmatrix},\sum\nolimits_{S,\mathrm{D}}\begin{bmatrix}\Sigma_{SS} & \Sigma_{SD}\\ \Sigma_{DS} & \Sigma_{DD}\end{bmatrix}\right) \tag{72}$$

Where variance trace (Σ_{SS}) = var ($\vec{S}$), (Σ_{DD}) = var ($\vec{D}$), and $\Sigma_{SD} = \Sigma^{T}_{DS}$ = CrossCov ($\vec{S}$, $\vec{D}$).

4.4 PDF OF THE PROBABILITY NO SIDELOBE EXCEEDS THE THRESHOLD

The probability that a sample of the sidelobe pattern, taken at an arbitrary angle $\Psi = \cos^{-1}(\cos\bar{\psi})$ away from the neighborhood of the main lobe, falls between f_0 and $f_0 + \delta f$ is

$$\alpha = \int_{f_0}^{f_0+\delta f} w_1(U)\,dU \tag{73}$$

And converges to (74) when the upper limit is made infinite.

$$\alpha = \int_{f_0}^{\infty} w_1(U)\,dU = e^{-f_0^2/N} = e^{-NU_0} \tag{74}$$

Now the probability that no sidelobe exceed a power level U_0 is provided such that

$$\begin{aligned} &\beta=(1-\alpha)^n=\left[1-e^{\left(-f_0^2/N\right)}\right]^n,\ n=\frac{2A}{\lambda}\left(1+|\Psi_0|\right) \\ &B=f_0^2/N=-\ln\left(1-\beta^{1/n}\right) \end{aligned} \tag{75}$$

where the value of n is determined from [3] and the autocovariance of (69). Likewise, B's value is defined as the power ratio of the threshold level to the theoretical sidelobe level, and β is the probability that no sidelobe exceeds a power level $U_0=(f_0/N)^2$.

4.5 PDF, MEAN AND VARIANCE OF B (THRESHOLD POWER LEVEL TO THE THEORETICAL SIDELOBE LEVEL)

The confidence level β = Prob no sidelobe exceeds B and is the probability of B's distribution function. Its derivative with respect to B is the pdf of it. Thus

$$W(B) = \frac{d\beta}{dB} = n\left(1 - e^{-B}\right)^{n-1} e^{-B} \tag{76}$$

Where $\overline{B}$, $\overline{B^2}$,…, $\overline{B^k}$ are the moments of B. The first two moments are the ones of most significant interest, for these give the average value and a measure of the variability about the average. The average is the first moment $\overline{B}$. Hence, the expected value of B is provided as

$$\overline{B} = \sum_{k=1}^{n} \frac{1}{k} \sim \ln n \lim_{n\to\infty} \tag{77}$$

And therefore, the comparison (77) shows that $B \approx \overline{B}$ - ln (1 - β). I.e., B differs from its mean value by a small constant or, more formally, by its confidence level β. The variance of B is $\overline{B^2}$ - $\overline{B}^2$ or

$$\sigma_B^2 = \sum_{k=1}^{n} \frac{1}{k^2} \to \frac{\pi^2}{6} \lim_{n\to\infty} \cdot \tag{78}$$

Therefore, it verifies that the peak sidelobe level (PSLL) is insignificantly affected by aperture size, distribution, and topology.

4.6 PEAK SIDELOBE ESTIMATOR B_P

A better estimator of the peak sidelobe level may be found by adding the expected value of ΔB and is not limited to the 3dB sidelobe region. Moreover, the analysis for this can be done by Taylor expanding the complex array factor, thereby taking its autocorrelation function, and for brevity, only the final result of this will be shown herein as a detailed derivation of this is found in [19].

$$\frac{\text{Peak Sidelobe}}{\text{Main Lobe}} = \frac{\text{Peak Sidelobe}}{\text{AverageSidelobe}} \frac{\text{AverageSidelobe}}{\text{MainLobe}} = \frac{B_p}{N}, \left\{ B_p = \frac{\text{PeakSidelobe}}{\text{AverageSidelobe}} = \frac{B + 1 + 2/B}{N} \right\} \tag{79}$$

As a result, B_p is defined as the peak sidelobe of a given power pattern of any geometrically defined random array cluster of isotropic elements divided by its theoretical average sidelobe power level. An illustration of the peak sidelobe estimator B is provided in Figure 38 for a SRA.

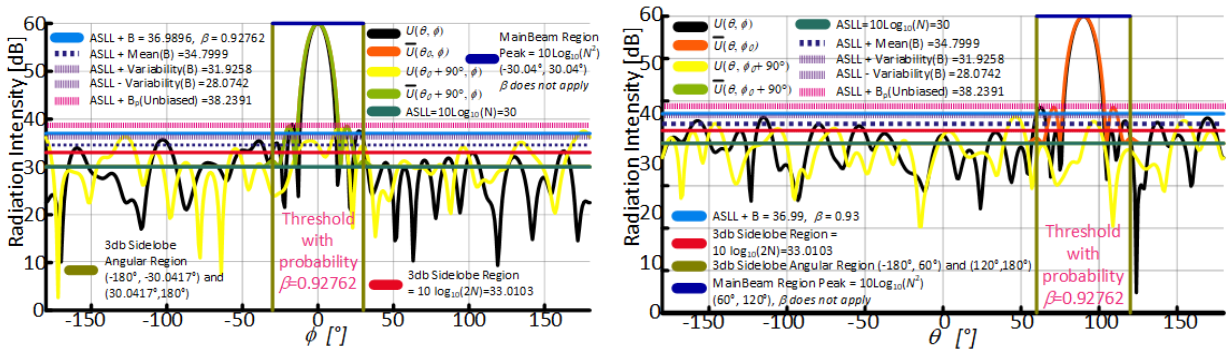

Figure 38. SRA statistics with N = 1000, and A / λ = 1; ϕ – cut plane, left and θ – cut plane right.

4.7 MINIMUM NUMBER OF ELEMENTS

Like the previous analysis, a derivation of the minimum number of elements (80) and sidelobe estimator B (81) in a random array for acceptable performance of this theory is found to satisfy the results of [50].

$$N_{\min} \approx \max\left(15, 2B\right) \tag{80}$$

$$B = -\ln\left(1-\beta^{1/n}\right) \simeq \ln n - \ln\left(1-\beta\right), \neg\beta \geq .5 \tag{81}$$

Experimental results are provided in [14] and provide validity (80) – (81) up to the present time.

4.8 MEAN VALUE OF THE PEAKING SIDELOBE IN THE 3DB SIDELOBE REGION IN ANGULAR SPACE

The average representation of the number of upward crossings at a given power level, say $v\ (f_{out})$ ([3 – 4] and [19]), is prepared under the assumption S and D are uncorrelated zero-mean Gaussian processes with variance $\sigma^2_S = \sigma^2_D = ½$.

$$E\left[v\left(f_{Out}\right)\right] = e^{-f_{Out}^2/N}\left(1-\left(2\tilde{A}\right)^{-1}\right)2\tilde{A}f_{Out}\sqrt{\pi/3N} \tag{82}$$

An illustration of the $v\ (f_{out})$ applied to the *CRA* and *SRA* is shown in Figure 192 of [14] as a function of the aperture size for a given number of elements and in angular space. This result is useful since the maximum peaking sidelobe appears to be no greater than 12 dB above the average sidelobe level for aperture sizes less than A/λ=100. Also, this is done outside of Ψ-space to verify the conclusiveness of previous works of [32] – [38]. Finally, the results appear to be tightly bound regardless of distribution or topology and validated by the results of Figure 39 – Figure 41.

4.9 MEAN STATISTICS ANGULAR SPACE

In angular space, comparisons of the periodic and random array are provided in Figure 39 – Figure 41.

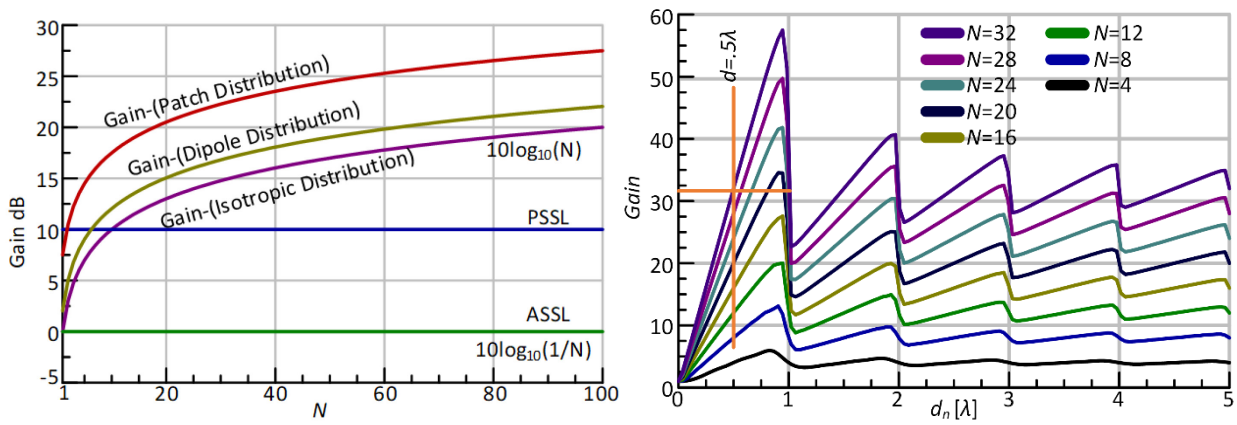

Figure 39. Ideal statistics for a sparse random array (invariant to distribution or topology – left) and gain of a periodic linear array (meridian scan – right). [39].

Thus, maximum directivity (or gain assuming no loss) of a random antenna array is seen to converge for sparse distributions to a directivity of N. Nevertheless, for discrete distributions, it is seen the gain of the array can grow to approximately $2N$ for spacing just under $.5\lambda$ in endfire scans or just under 1λ for broadside scans [39]. This behavior occurs right before grating lobes are introduced into the pattern and can further be interpreted as a fluctuation in the mutual coupling between elements varying as the spacing is varied. For large spacing, however, this type of discrete distribution also convergences with the directivity of N and illustrated in Figure 39

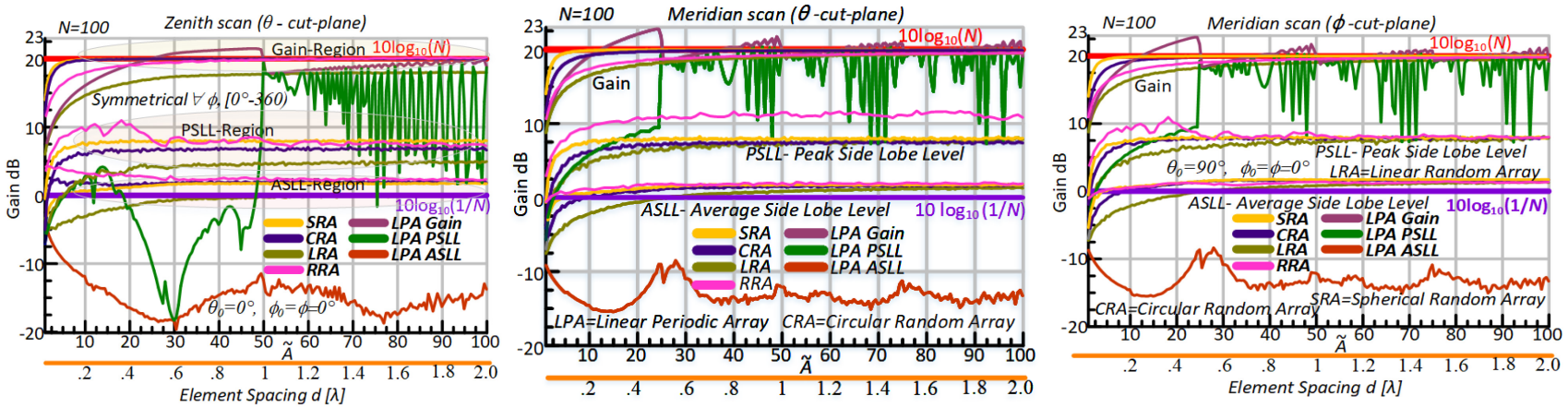

Figure 40. Statistics of 1, 2, and 3 dimensional random arrays (zenith – left, meridian theta cut plane – middle & phi cut plane – right).

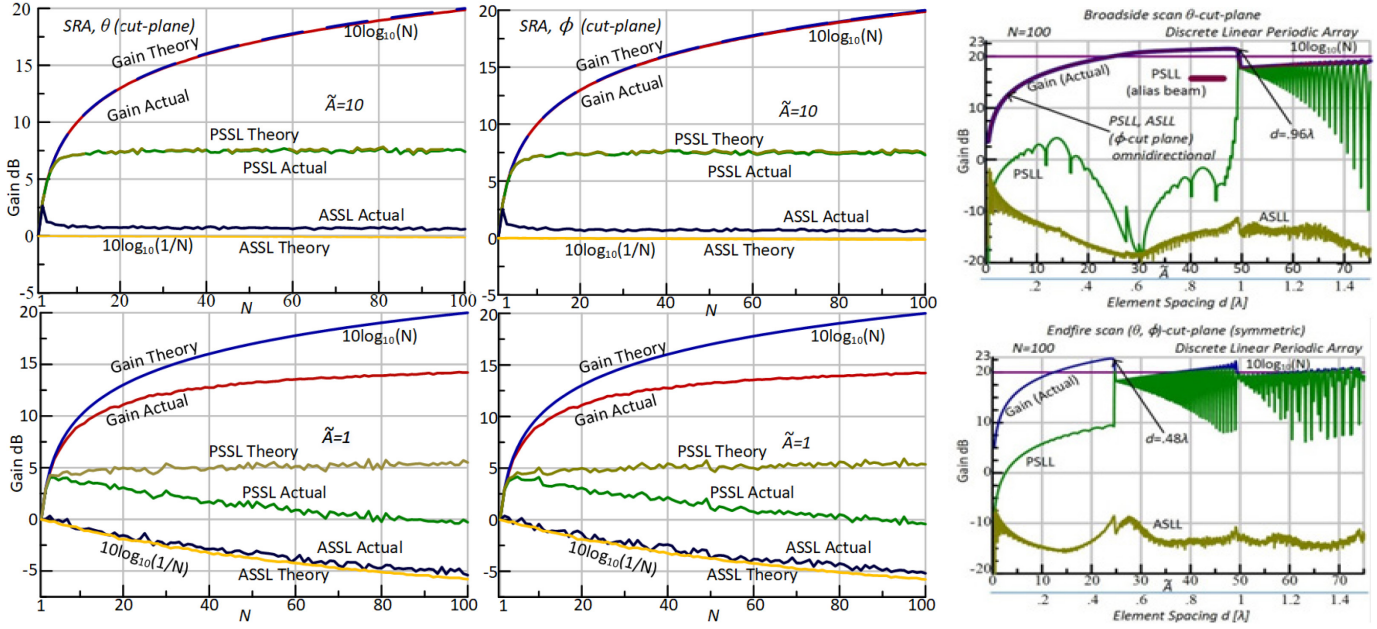

Figure 41. Statistics of a spherical array with fixed aperture size in ϕ and θ – cut planes versus element population *N* and statistics of a linear periodic array scanned at broadside and meridian.

4.10 NON-ISOTROPIC ELEMENTS

A simple antenna pattern approximates a dipole with a peak gain of about 2dB greater than an isotropic radiator. As array gain is a function of element gain and the number of elements, increasing element gain efficiently improves array gain while shrinking element beamwidth. This result restricts the array's nominal angular scanning range to the elements' beamwidth, though gains between 5 and 10dB are common.

For a single source element oriented in the *Cartesian*-axis, we rewrite our potential function in terms of the vector effective length:

$$n \simeq (2A/\lambda)\left(|\Psi_0| + \lambda \Big/ \left(4\left(\pi B_{Isotropic}\right)^{1/2} I\right)\right)$$
$$I = \sqrt{\frac{\int x^2 i(x)\,dx}{\int i(x)\,dx}}, B_{Isotropic} = \left[\ln\left(2\tilde{A}\left(1+\cos\Psi_0\right)\right) - \ln\ln(\beta)\right] \quad (83)$$

In the idealized case, each element of the array has a rectangular beamwidth $\Delta\Psi_E$, as sketched in Figure 42 and only the sidelobes of the array factor within the interval $|\Psi| < \Delta\Psi_E/2$ would be counted in the calculation of the array factor parameter n. Thus, the number of independent sample points would change to $n = 2A/\lambda\,(\Delta\Psi/2 + |\Psi_0|)$.

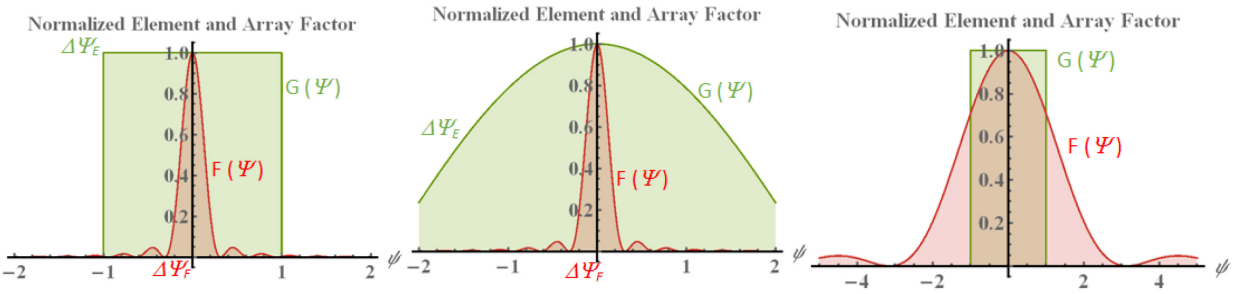

Figure 42. Ideal rectangular element pattern *G* (Ψ) - left. Non-ideal smoothly varying element pattern – middle and non- ideal smoothly varying element pattern right.

Within the beamwidth of the element pattern, the effect of beamsteering in n also may be calculated as:

$$n \simeq (2A/\lambda)\left(|\Psi_0| + \lambda \Big/ \left(4\left(\pi B_{Isotropic}\right)^{1/2} I\right)\right),\ I = \sqrt{\frac{\int x^2 i(x)\,dx}{\int i(x)\,dx}},\qquad B_{Isotropic} = \left[\ln\left(2\tilde{A}\left(1+\cos\Psi_0\right)\right) - \ln\ln(\beta)\right] \quad (84)$$

Experimental results of the mean sidelobe level of the measured, simulated, and expected value (EV) results of a patch array of $N = 32$ elements are also to investigate the validity of previous results for both SRA and CRA distributions. Results of each distribution are illustrated in Figure 43 and examined as 30.65 dB, 19.35 dB, and 22.51 dB down from the mainbeam, respectively for the CRA, and 23.59, 21.77, and 21.49 dB down for the SRA. It is seen that all methods provide commensurate agreement, which validates the theoretical basis of this work.

4.11 WIDEBAND SIGNALS

A wider band of operational frequencies further reduces *n*. The qualitative effect becomes apparent when the Fourier transform relation between the far-field array factor *F* (Ψ), and aperture excitation *i* (x) is written as (85) where the composite mean pattern Λ (Ψ) = q_1 Λ (Ψ, ω_1) + q_n Λ (Ψ, ω_2) and *q* is the relative strength of the frequency components of (86).

$$\Lambda(\Psi) = \oint s(\omega) F(\Psi, \omega)\, d\omega \tag{85}$$

$$\Delta\Psi_1 - \Delta\Psi_2 = \frac{\lambda_1}{2A} - \frac{\lambda_2}{2A} = \frac{\Delta\lambda}{2A} = \frac{\Delta\lambda}{\lambda}\frac{1}{\tilde{D}} = \frac{\Delta\Psi}{Q}, \quad Q = \lambda/\Delta\lambda,\ \tilde{D} = 1/2\tilde{A} \tag{86}$$

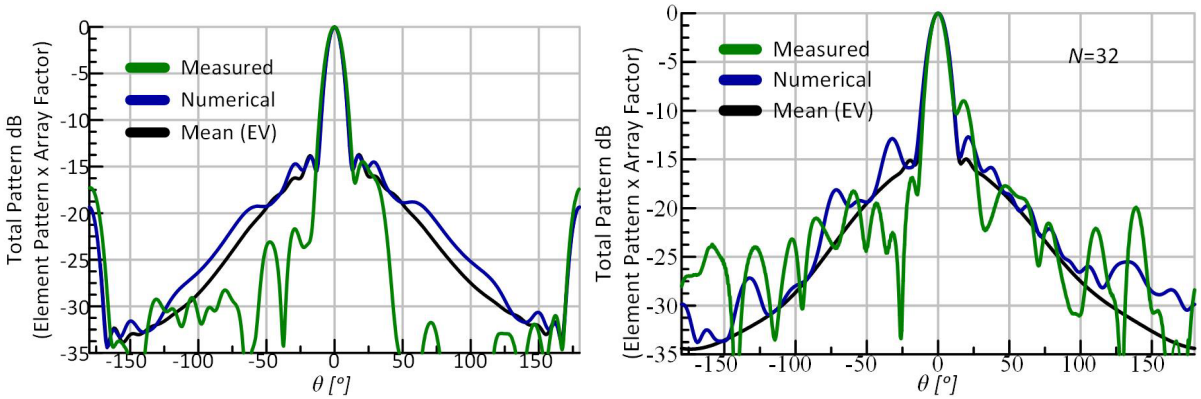

Figure 43. Statistical comparisons of a circular (left) and spherical (right) distributed array in zenith scan with patch element factor.

An example of array factors of slightly varying wavelengths is provided in Figure 44, and from [19], the array parameter (87) is found to be the smaller of the preceding isotropic value of *n*.

$$n \simeq \min\left\{2\tilde{A}, \omega_0 \Big/ \Delta\omega\left(B_{Isotropic}\right)^{1/2}\right\} + 2\tilde{A}\left|\Psi_0\right| \tag{87}$$

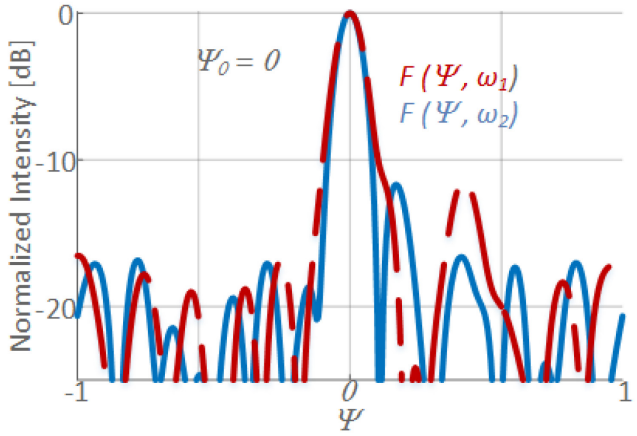

Figure 44. Array factors at two slightly different, slightly different wavelengths.

4.12 PERIODIC VS. CONFORMAL, PLANAR AND VOLUMETRIC ARRAY NUMBER OF ELEMENT COMPARISON

The three dB sidelobe region is described such that it forms an envelope 3dB larger than that of the characteristic pedestal.

$$\mathrm{ENV}\left\{\left|\Lambda\left(\Psi_1\right)\right|^2\left[1-1/N\right]\right\}=\left[1-1/N\right]\left(\Psi_1/2\right)^n=2/N \tag{88}$$

where ENV means "envelope of." The envelope of the radiation pattern is the denominator of the characteristic function. [19] Secondly, its square is the envelope of the power pattern such that

$$\mathrm{N}=2^{1-n}/\Psi_1\ +1 \tag{89}$$

E.g. for $\Psi_1 = kA\Delta\Psi$ with kA=20, $\Delta\Psi = 1° = \pi / 180$ rad and $n = 1 – 3$ for a linear (line), planar (circle) and volumetric (spherical) distribution respectively one obtains

$$\mathrm{N}=\frac{2^{1-n}}{\Psi_1}+1=\left(\frac{2^{1-n}}{20}\frac{180}{\pi}+1\right)\approx\left(3,5,\ 9\right)_{n=1,2,3} \tag{90}$$

For the periodic array, the number of elements for a linear, planar, and volumetric distribution is calculated such that

$$\mathrm{N}=\left(D/d_{x|y|z}\ +1\right)^n=\left(2D/\lambda\ \ +1\right)^n=\left(41,441,9261\right) \tag{91}$$

One could thin the random array by approximately three orders of magnitude, offering considerable cost savings.

This page is intentionally blank

5. MUTUAL COUPLING

The last statistical measure to be added to this analysis is the coupling coefficient, and for simplicity, this is to be taken as a uniform amplitude distribution [34] such that

$$AF\left(r_n,\psi_n,r_m,\psi_m,\theta,\phi\right)=\frac{1}{N}\sum_{n=1}^{N}e^{jkr_n\left(\cos\psi_n-\cos\psi_{n0}\right)}-C_{mn},\quad C_{mn}=\frac{1}{N^2}\sum_{n=1}^{N}\sum_{\substack{m=1,\\ m\neq n}}^{N}e^{jk\left[r_n\left(\cos\psi_n-\cos\psi_{n0}\right)-r_m\left(\cos\psi_m-\cos\psi_{m0}\right)\right]} \tag{92}$$

Now assume $r_n\ cos\ \psi_n$ - $r_m\ cos\ \psi_m$=$r_{nm}\ cos\ \psi_{mn}$ is such that $\overline{r_{nm}cos\psi_{nm}}=r_{nm}\ cos\psi_{nm}/\bar{d}$ where $\overline{r_{nm}}=r_{nm}\ /\bar{d}$ and is the average spacing between the elements

$$C_{mn}=\frac{1}{N}\sum_{n=1}^{N}\sum_{\substack{m=1,\\ m\neq n}}^{N}e^{j\left(\overline{r_{nm}\cos\psi_{nm}}\bar{d}_{nm}\right)} \tag{93}$$

Hence, the mean value of the coupling coefficient is hence

$$\begin{aligned}\overline{C_{mn}}&=\left(1-\frac{1}{N}\right)\overline{e^{jk\left[r_n\left(\cos\psi_n-\cos\psi_{n0}\right)-r_m\left(\cos\psi_m-\cos\psi_{m0}\right)\right]}}\\&=\left(1-\frac{1}{N}\right)\overline{e^{j\bar{d}\,\bar{d}_{nm}}}=\left(1-\frac{1}{N}\right)\Lambda\left(\bar{d}\right)\qquad\left\{\neg\overline{d_{nm}}=\frac{\left[r_n\left(\cos\psi_n-\cos\psi_{n0}\right)-r_m\left(\cos\psi_m-\cos\psi_{m0}\right)\right]}{d_{nm}}\right\},\bar{d}=kd_{nm}\end{aligned} \tag{94}$$

Where $\bar{d}$ represents the average distance amongst the elements. If $\overline{c_{nm}}$=0, then the mean of the array factor is (25) as expected. Similarly, for large mean value spacing $\bar{d}$ the coupling coefficient goes to zero. Otherwise one obtains

$$\bar{U}\left(\Psi;n\right)=1/N+\left(1-1/N\right)\left[\left|\mathrm{Sinc}\left(\Psi;n\right)+\mathrm{Sinc}\left(k\,\bar{d};n\right)\right|^2\right], \tag{95}$$

5.1 GRAPH THEORY

The characteristic polynomial is the polynomial left-hand side of the characteristic equation

$$\det\left(U-\lambda I\right)=0 \tag{96}$$

where U is a square matrix, and I is the identity matrix of identical dimension. This result provides an alternative graphical representation for coupling such that all nodes in the graph are illustrated in matrix form.

$$\underset{k_1}{(0)},\qquad \underset{k_2}{\begin{pmatrix}0&1\\1&0\end{pmatrix}},\underset{k_3}{\begin{pmatrix}0&1&1\\1&0&1\\1&1&0\end{pmatrix}},\underset{k_4}{\begin{pmatrix}0&1&1&1\\1&0&1&1\\1&1&0&1\\1&1&1&0\end{pmatrix}},\underset{k_5}{\begin{pmatrix}0&1&1&1&1\\1&0&1&1&1\\1&1&0&1&1\\1&1&1&0&1\\1&1&1&1&0\end{pmatrix}} \tag{97}$$

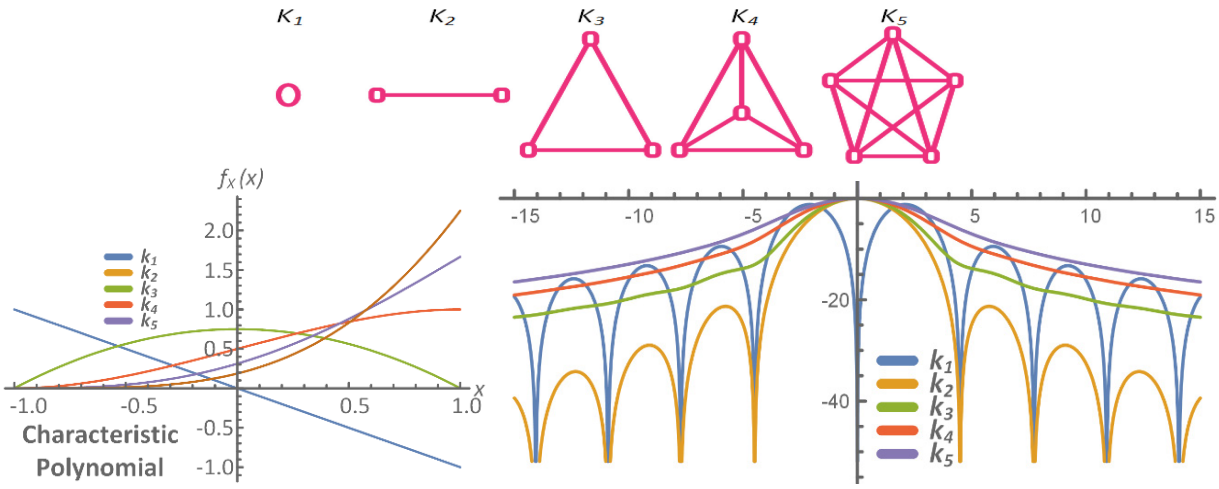

Figure 45. Relation to the characteristic polynomial.

Moreover, for uniform coupling amongst 2 source nodes as illustrated by the distribution of k_2, one ends up obtaining the parabolic distribution function ¾ (1–x) of which provides the *Sinc* (Ψ; n = 3) characteristic mode.

6. ORTHOGONAL SETS AND AMPLITUDE DISTRIBUTIONS

6.1 N-SPHERE AMPLITUDE TAPERS USING THE JACOBI AND GEGENBAUER POLYNOMIALS (HYPERGEOMETRIC POLYNOMIALS)

The Jacobi polynomials are orthogonal with respect to $(1-x)^{\alpha}(1+x)^{\beta}$ on the interval [–1, 1] and produce special cases of the Gegenbauer, Legendre, Zernike, and Chebyshev polynomials. For example, the Gegenbauer (Ultraspherical) Polynomials are shown below and will be utilized in the following section for their unique ability to orthogonalize circular topologies.

$$f_X(x)\alpha\left(1-x^2\right)^{\lambda-1/2} C_n^{\lambda}(x) \tag{98}$$

The amplitude tapers of both the even and odd modes of the Sinc and Cosinc [18] kernels are further generalized to the *N*-dimension by (99) and (100), respectively.

$$\Lambda(\Psi) = \text{Ultra Sinc}_n^m(\Psi) \tag{99}$$

$$\Lambda(\Psi) = \text{Ultra Cosinc}_n^m(\Psi) \tag{100}$$

The argument n is taken to be the probability distribution of the element population and is provided by the n^{th} mode of the Sinc kernel. I.e., the $n = 0$, $n = 1$, $n = 2$, and $n = 3$ modes respectively represent the horocycle (ring), infinite circle (line), circle, and spherical distributions. The m modes of operation are generated close to the Gegenbauer or ultraspherical harmonics of alternating and increasing order of Chebyshev and Legendre polynomials. [18] Examples of (99) are provided in Figure 46 – Figure 48 for $n = 0 – 2$.

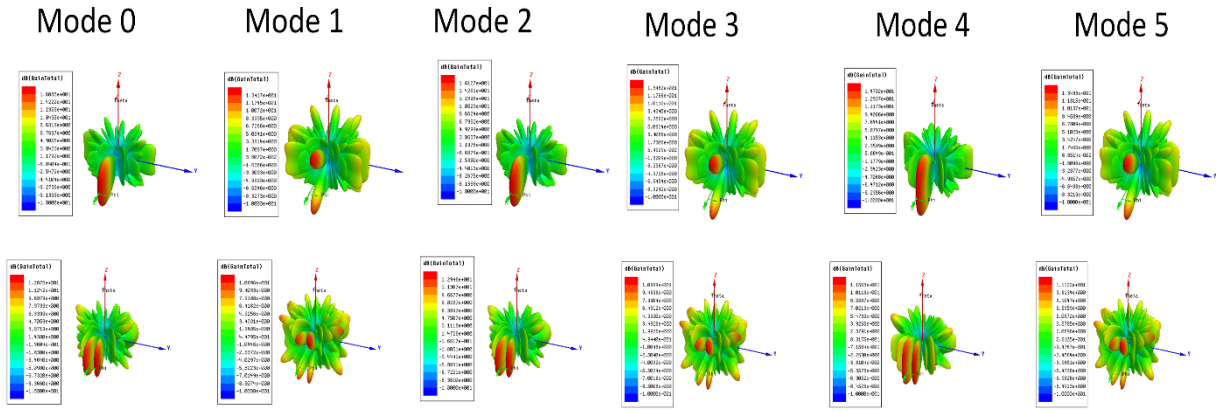

Figure 46. Characteristic amplitude modes ($n = 0 – 5$) for a ring random array steered at endfire; Bessel modes (top); Weber modes (bottom).

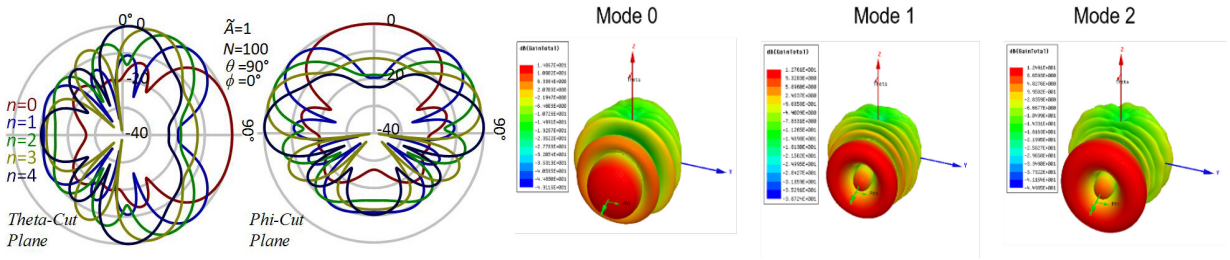

Figure 47. Characteristic amplitude modes (n =1) for a linear random array steered at endfire; theta cut plane shown in the two charts left; phi cut plane middle; HFSS simulations of modes 0 – 2 right.

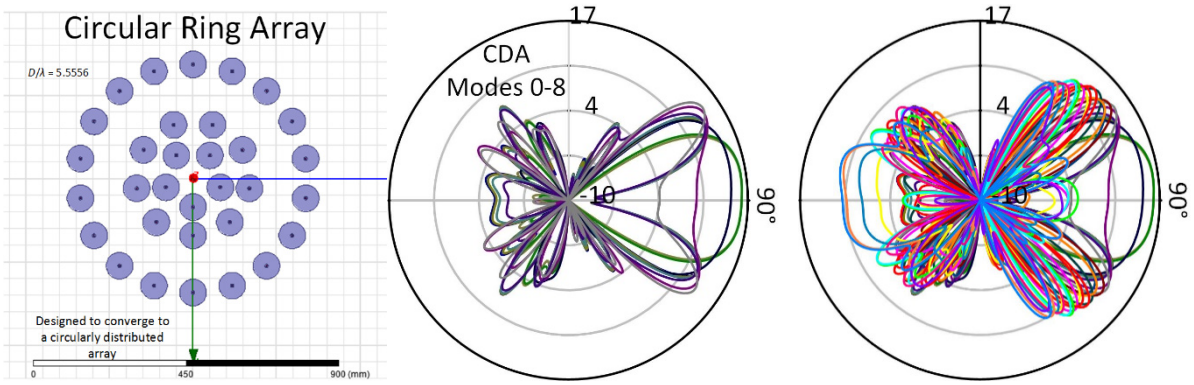

Figure 48. Characteristic amplitude modes (n = 2) for a circular random array steered at endfire (left); Bessel modes 0 – 8 (middle) and modal analysis 0 – 25 (right).

6.2 HARDY DISTRIBUTION

The Hardy space $H^2(\Psi)$ consists of the even (Sinc) and odd (Cosinc) modes on L^2. This space has unique properties as it causes the negative spatial Fourier coefficients to vanish. An example of the first n=12 modes are provided, and it is seen that the peak of the odd modes approximates beamwidth. Moreover, these modes are similar to Euler's identity when added and are denoted the EulerSinc modes of (101) and illustrated in Figure 49. Similarly, Bessel – Weber modes are provided illustratively in Figure 50.

$$\mathrm{EulerSinc}_n(\Psi) = \mathrm{Sinc}_n(\Psi) + j\,\mathrm{Cosinc}_n(\Psi) \tag{101}$$

$$\mathrm{BesselWeberSinc}_{nm}(\Psi) = \mathrm{Sinc}_n(\Psi) + j\mathrm{Weber}_n(\Psi) \tag{102}$$

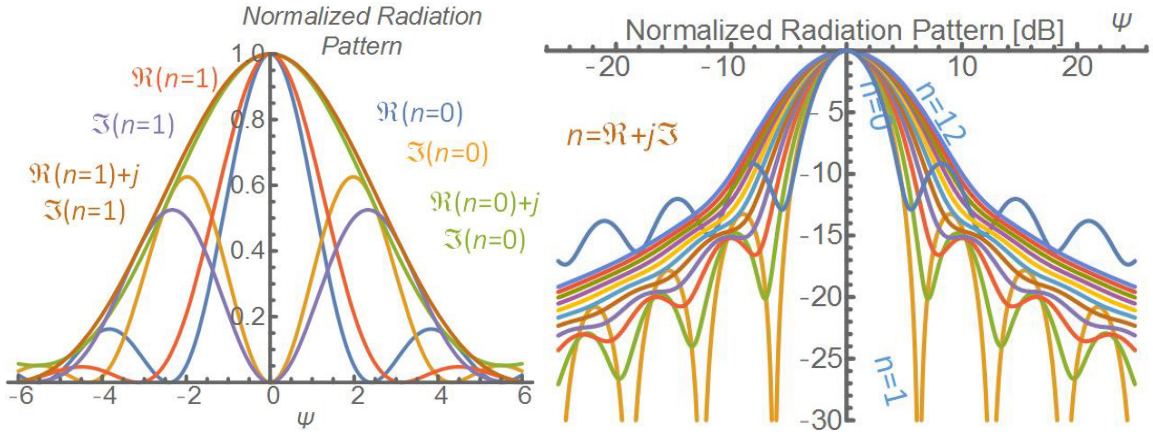

Figure 49. EulerSinc, Sinc, and Cosinc modes comparison (left). First n = 12 EulerSinc modes (right).

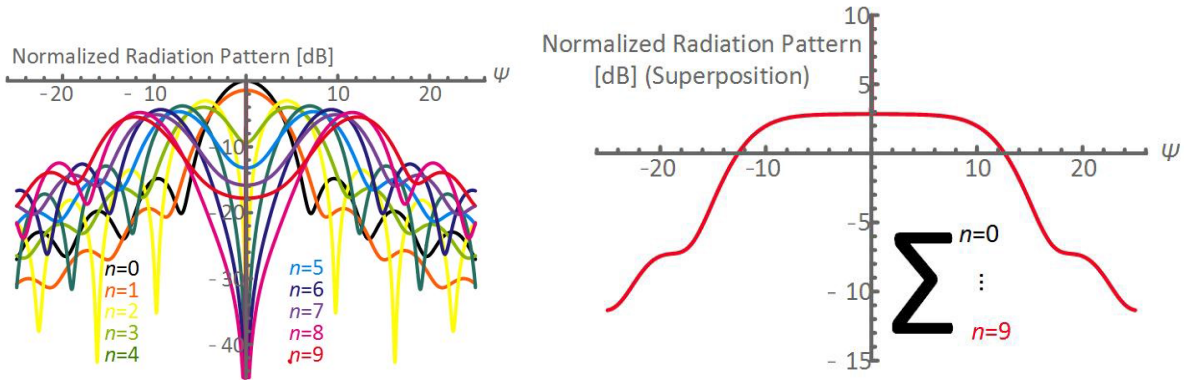

Figure 50. Bessel-Weber modal comparison, (left) and first ten modes superimposed (right).

6.3 BABINET'S PRINCIPLE

6.3.1 Green's Function of an Infinite Planar Screen

In free space, the Dirichlet Green's function is provided by the well-known green's function of (103) and by that of (104) when placed over an infinite planar screen:

$$G(\vec{r},\vec{r}') = \exp\left(jk\left|\vec{r}-\vec{r}'\right|\right)/\left|\vec{r}-\vec{r}'\right|, \tag{103}$$

$$G(\vec{r},\vec{r}') = \frac{e^{jk|\vec{r}-\vec{r}_2'|}}{|\vec{r}-\vec{r}_2'|} - \frac{e^{jk|\vec{r}-\vec{r}_1|}}{|\vec{r}-\vec{r}_1|}, \vec{r}_2 = (x',y',+z'), \vec{r}_1 = (x',y',-z') \tag{104}$$

Illustrated in Figure 1, the location $\vec{r}'_2$ is in V, and generated from a monochromatic point source S (the image point at $\vec{r}_1$ is not in V). This result satisfies the homogenous wave equation ($\nabla^2 + k^2$) $G(\vec{r},\vec{r}') = -4\,\pi\delta(\vec{r}-\vec{r}')$ in V, such that it vanishes at infinity ($r' \to \infty$ since $1/r'^2 \to 0$) and the boundary plane z'=0.

The characteristic amplitude $\varphi(\vec{r})$ for a monochromatic point source S, observed at the observation point O on the opposite side of the screen becomes the Kirchhoff integral such that:

$$\varphi(\vec{r}) = -1/(4\pi)\int_S d^2r'\vec{n}'\cdot\left(\varphi(\vec{r}')\nabla' G(\vec{r},\vec{r}')\right). \tag{105}$$

6.3.2 Radiation from a Finite Source

If a slit of Figure 51 is cut into the screen, the wave amplitude $\varphi(\vec{r}') = 0$ on the screen as well as on the boundary of the screen results in a nonzero contribution from the opening of the screen:

$$\varphi(\vec{r}) = -1/(4\pi)\int_{Opening} d^2r'\vec{n}'\cdot\left(\varphi(\vec{r}')\nabla' G(\vec{r},\vec{r}')\right), \tag{106}$$

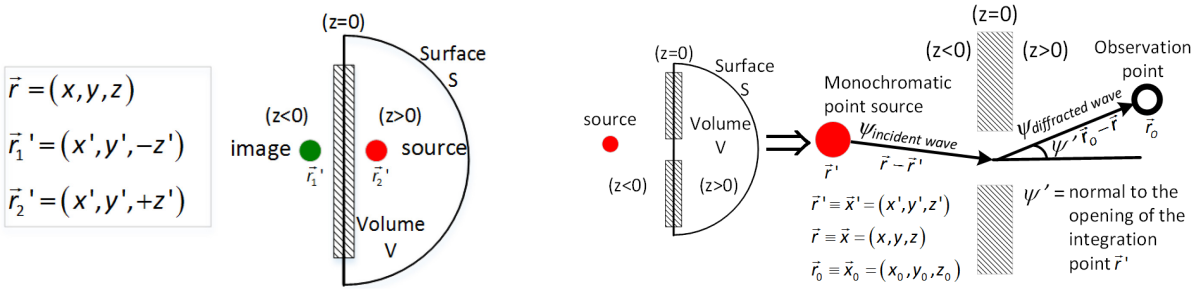

Figure 51. The volume of a source and infinite planar screen (left) and aperture excitation from an isotropic point source (right).

where $\vec{n}'$ is the direction in the opening of the slit of the volume V. Thus, $\nabla' G(\vec{r},\vec{r}')$ in the $\vec{n}'$ or outward normal direction becomes:

$$-\frac{d}{dz'}G(\vec{r},\vec{r}') \approx \frac{jk(z-z')}{|\vec{r}-\vec{r}_2'|}\frac{e^{jk|\vec{r}-\vec{r}_2'|}}{|\vec{r}-\vec{r}_2'|} + \frac{jk(z+z')}{|\vec{r}-\vec{r}_1'|}\frac{e^{jk|\vec{r}-\vec{r}_1'|}}{|\vec{r}-\vec{r}_1'|} \tag{107}$$
$$\neg d|\vec{r}-\vec{r}_2'|^{-1}/dz \wedge d|\vec{r}-\vec{r}_1'|^{-1}/dz \approx 0\,(\text{denominator } \textit{neglible}),\ \vec{r}'_{Isotropic} = \vec{r}_1',\ \vec{r}'_{Finite\ Source} = \vec{r}_2'.$$

Equation (106) further reduces at the plane of the screen to:

$$-\frac{d}{dz'}G(\vec{r},\vec{r}')\Big|_{z=0} \approx \frac{2jkz}{|\vec{r}-\vec{r}'|}\frac{e^{jk|\vec{r}-\vec{r}'|}}{|\vec{r}-\vec{r}'|},\ \neg\,\vec{r}_2 = \vec{r}_1 \text{ at } z = 0\,. \tag{108}$$

Hence, the Kirchhoff approximation yields the following expression for the wave amplitude of the field observed at $\vec{r}$:

$$\begin{aligned}\varphi(\vec{r}) &= -1/(4\pi)\int_\sigma d^2r'\vec{n}'\cdot\left(\varphi(\vec{r}')\nabla' G(\vec{r},\vec{r}')\right)\\ &= -jk/(2\pi)\int_{opening} d^2r\, e^{jk|\vec{r}_1'-\vec{r}_2'|}e^{jk|\vec{r}-\vec{r}_2'|}/\left|\vec{r}_1'-\vec{r}_2'\right|\left|\vec{r}-\vec{r}_2'\right|\cos(\psi_2'),\quad \ni\ \cos(\psi_2') = \hat{r}_2'\cdot\hat{r} = z/|\vec{r}-\vec{r}_2'|.\end{aligned} \tag{109}$$

This integral demonstrates the Huygens-Fresnel principle of which is composed of three distinct terms. The first term represents field strength received at the point $\vec{r}'_2$ transmitted the point source located at the and reradiated from the slit. The second term represents the field received generated from the aperture excitation at $\vec{r}'_2$ and received at the observation point $\vec{r}$. The third and final term is the inclination factor.

Moreover, it can be easily shown that the Fraunhofer region's characteristic function becomes (109), which is nothing more than pattern multiplication of a point source and sinc function generated from a uniform aperture excitation. Finally, the aperture reaches a maximum if $\hat{\psi}_{IncWave} - \hat{\psi}_{DiffWave} = 0$, and similar to phased array analysis,

$$\Lambda(r,\Psi)_{N\to\infty} = (-jk/(2\pi))\left(e^{jkr_1}/r_1\right)\left(\mathrm{sinc}\left(kA\vec{\Psi}\right)e^{jkr_2}/r_2\right) \overset{Normalized}{\approx} \left(e^{jkr}/r\right)\left(\mathrm{sinc}\left(kA\vec{\Psi}\right)\right), \vec{\Psi} = \left(\hat{\psi}_{Inc\,Wave} - \hat{\psi}_{Diff\,Wave}\right)$$
$$\neg\frac{e^{jk|\vec{r}_1\,'-\vec{r}_2\,'|}}{|\vec{r}_1\,'-\vec{r}_2\,'|}\frac{e^{jk|\vec{r}-\vec{r}_2\,'|}}{|\vec{r}-\vec{r}_2\,'|} \approx \frac{e^{jk(r+\vec{r}_1\,')}}{|r|}e^{jk(\vec{\Psi})\vec{r}_2\,'}, \cos(\psi)\approx 1. \tag{110}$$

6.4 COMPLEMENTARY SCREENS

First, consider two different screens that are complementary, as illustrated in Figure 52 [40].

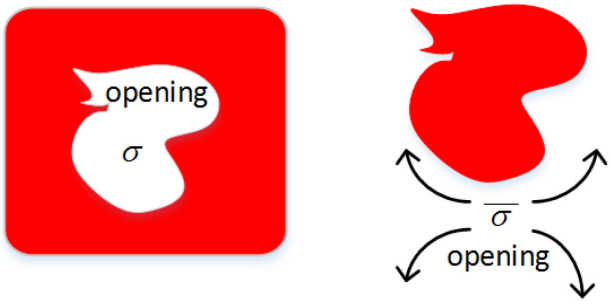

Figure 52. Complimentary screens.

Figure 52, labeled σ has an opening through the center, while the complementary image is just a disk with the entire $z = 0$ plane as its opening, denoted $\bar{\sigma}$. Hence the characteristic amplitude of two complementary cases becomes:

$$\begin{aligned}\varphi(\vec{r}) &= -1/(4\pi)\int_{\sigma} d^2r'\vec{n}'\cdot\left(\varphi(\vec{r}\,')\nabla G(\vec{r},\vec{r}\,')\right)\\ \overline{\varphi(\vec{r})} &= -1/(4\pi)\int_{\bar{\sigma}} d^2r'\vec{n}'\cdot\left(\varphi(\vec{r}\,')\nabla G(\vec{r},\vec{r}\,')\right)\end{aligned}, \tag{111}$$

where $\sigma + \bar{\sigma}$ represents the entire plane $z = 0$ and its characteristic function, $\varphi(\vec{r}) + \overline{\varphi(\vec{r})}$ at the observation point $\vec{r}$ includes no diffraction. To interpret this, note that $\varphi(\vec{r})$ may be written as:

$$\varphi(\vec{r}) = f\exp\left(jk|\vec{r}-\vec{r}_1\,'|\right)/|\vec{r}-\vec{r}_1\,'| + \psi_{diff}(\vec{r}), \tag{112}$$

where f is denoted as its ray optic amplitude. If f=1, line-of-sight exists from the observer to the source, and if f = 0, no line-of-sight exists. The second term represents the diffraction of the wave. Moreover, the sum for f=0 and f = 1 includes the term $\exp(jk|\vec{r}-\vec{r}\,'|)/|\vec{r}-\vec{r}\,'|$ representing Babinet's principle: solving one diffraction problem is tantamount to solving its complement [40].

6.5 BABINET'S PRINCIPLE USING COMPLEMENTARY TOPOLOGY

The superposition of a triangular distribution $f(x)$ in (113) and complementary inverted triangular distribution $f(\bar{x})$ represents a square distribution in the entire plane $z = 0$ plane and illustrated in Figure 53. Thus $\Lambda(\Psi) + \overline{\Lambda(\Psi)}$ represents the aggregated Fourier transform pair of (114) and (115),

which provides the well-known sinc (Ψ) (116). Accordingly, this is Babinet's Principle as solving for one characteristic function solves its complement,

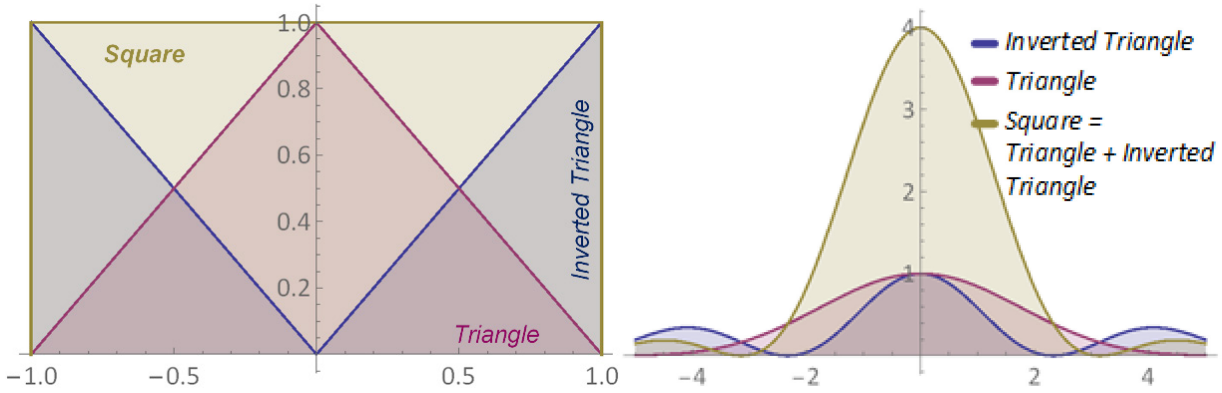

Figure 53. Complementary triangular topologies (left) and characteristic functions (right).

$$f(x)=1-|x|,\quad \overline{f(x)}=1+|x|, \tag{113}$$

$$\Lambda(\Psi)_{Triangle}=\int_{-1}^{1}f(x)e^{j\Psi x}=2\mathrm{h}_0(\Psi)/\Psi, \tag{114}$$

$$\Lambda(\Psi)_{Triangle}^{Inverted}=\overline{\Lambda(\Psi)}_{Triangle}=\int_{-1}^{1}\overline{f(x)}e^{j\Psi x}=-2\mathrm{h}_1(\Psi)+1, \tag{115}$$

$$\overset{Square}{\Lambda}(\Psi)=\Lambda(\Psi)_{Triangle}+\overline{\Lambda(\Psi)}_{Triangle}=2j_0(\Psi)=2\mathrm{sinc}(\Psi). \tag{116}$$

7. FREQUENCY-RANGE BEAMSTEERING

Diversity beamsteering utilizes techniques for unique beamsteering capabilities dependent on spatial range characteristics. E.g., each element is assigned a unique frequency f_n of which applies an offset (Δf_n) of the operating frequency f_0. Also, we assume $\Delta f_n << f_0$ such that we can steer the array by taking applying the phase difference between the n^{th} element Ψ_n and the reference element Ψ_0 (117) – (118). An example of this is applied to a CRA in Figure 54 using the approach used in [41].

$$\begin{aligned}\Psi_0 &= kR_0 \approx 2\pi f_0 r_0 / c \\ \Psi_n &= kR_n \approx 2\pi f_n \left(r_0 - r_n\left(\cos\psi_{n0}\right)\right)/c, f_n = \left(f_0 + \Delta f_n\right)\end{aligned} \tag{117}$$

$$\Delta\Psi = \frac{2\pi}{c}\left(\left\{f_0 r_n\left(\cos\psi_n\right)\right\} + \Delta f_n r_n\left(\cos\psi_{n0}\right) - \Delta f_n r_0\right) = 0 \tag{118}$$

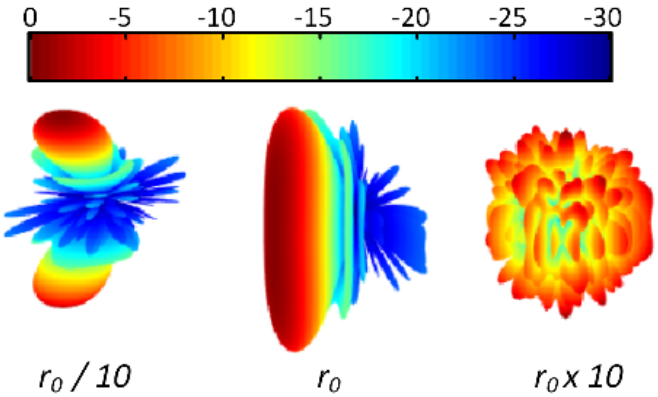

Figure 54. CRA steered at r_0 / 10 (left); r_0 (middle) and r_0 x 10 (right).

This page is intentionally blank

8. MOBILE DISTRIBUTION (RANGE-DOPPLER)

8.1 STATIONARY DISTRIBUTION

The ensemble average of the array factor is shown by assuming the overbar representation (122). This result is recognized as the characteristic function of $r_n \cos \Psi_n$ in angular space and can then be integrated against a given probability element distribution function (pdf) $f(x)$, yielding its associated characteristic function $\Lambda(\Psi)$ in closed form (123):

$$F(\theta,\phi|R_n) = \sum_{n=1}^{N} \frac{e^{jkR_n}}{N} = \frac{1}{N}\sum_{n=1}^{N} e^{jkr\sqrt{1+x^2-2x\cos\psi_n}}, \quad \begin{matrix} x = r_n / r, \\ \cos\psi_n = \hat{r}\cdot\hat{r}_n \end{matrix} \tag{119}$$

$$R_n = r\sqrt{1+x^2-2x\cos\psi_n} \approx \sum_{n=0}^{N} r\binom{1/2}{n}\left(x^2-2x\cos\psi_n\right)^n. \tag{120}$$

$$\begin{aligned} &x = \left(r_n + t_n V\right)/\left(r+tV\right),\ \tilde{r}_n = r_n/A, \tilde{t}_n = t_n/T_{PRI}\ , \Delta A = VT_{PRI} \\ &R_n \approx r + tV - \left(\tilde{r}_n A + \tilde{t}_n \Delta A\right)\cos\psi_n + \left(r_n + t_n V\right)^2 \Big/ \left(2\left(r+tV\right)\right) \end{aligned} \tag{121}$$

$$\bar{F}(\theta,\phi) = \sum\nolimits_1^N e^{jkr_n\cos\Psi_n}/N \tag{122}$$

$$\Lambda(\Psi) = \bar{F}(\Psi) = \bar{S}(\Psi) + \bar{D}(\Psi) = \oint f(x) e^{j\Psi x} dx \tag{123}$$

The ensemble average of the two-way array factor (on receive) is shown by assuming the overbar representation of

$$\bar{F}(\theta,\phi) = \sum_{n=1}^{N} \mathrm{A}\left(\delta\left(t_n - 2R_n/c\right)\right)\exp\left(A\left(2kR_n - w_n t_n\right)/A\right) \Big/ N \tag{124}$$

where A is a function of the amplitude response of the given return pulse arriving at $(t_n - 2R_n / c)$, and A is the aperture radius.

8.2 MOBILE DISTRIBUTION

8.2.1 First-order phase variations

For a mobile distribution, the provided array factor may be rewritten as (125). This result includes complexity since the intended frequency component is shifted by the Doppler coefficient $f_{d,n}$ and embedded into its phase term:

$$2kR_n - \omega t = \left(2kR_n - 2\pi\left(f_{0,n} + f_{d,n}\right)t\right) = \left(2k\left(R_n + v_n t_n\right) - \omega_0 t\right) \tag{125}$$

The respective Doppler shift of the nth element radiator is $f_{d,n} = 2\ Vn\ /\ \lambda\ (1 + \beta_{v,n}\ )$ where $\beta_{v,n} = V_n / c$ is used for completeness, but is traditionally assumed negligible when Vn / c. [42] Hence, the array factor in (124) for circular distributions of radius A becomes (10):

$$\bar{F}(\theta,\phi) = \sum_{n=1}^{N} A\left(t - 2R_n/c\right)\mathrm{e}^{\left(2kA\left(\tilde{R}_n + \tilde{R}_n v_n/c + v_n\tilde{t}_n\right) - \omega_{0,n}t_n\right)} \Big/ N,\ \ \tilde{R}_n = R_n/A,\ \tilde{t}_n = t_n/A \tag{126}$$

where kA, $\tilde{R}_n, \tilde{R}_n\, V/c$ and $V\tilde{t}_n/A$ are unit-less in the phase term for mathematical convenience. As a result, the pulse echoed from a constant velocity target approximates a Doppler shift of 2 V/λ and a phase shift of 2 $k\,R$ (1+ β_v) radians. Finally, when the target's return is off-axis, Figure 55, then the associated down-range Doppler shift becomes a function of angle such that fd,n= co ψ.

8.3 STOP AND HOP APPROXIMATION

In equation (124) simplification of the constant phase shift, 2 $k\,R$ (1+ β_v) to 2 $k\,R$ provides no difference in the magnitude or Doppler shift of the echo and can be ignored reducing (124) to (127).

$$\bar{F}(\theta,\phi) = \sum_{n=1}^{N} \mathrm{A}\left(\delta\left(t_n - 2R_n/c\right)\right) \mathrm{e}^{\left(2kA\left(\tilde{R}_n + v_n\tilde{t}_n\right) - \omega_{0,n}t_n\right)} \Big/ N \tag{127}$$

For example, a constant radial velocity means $R\,(t) = R_0 + vt$, where negative v corresponds to an approaching target is illustrated in Figure 55 given m pulses. Moreover, on pulse # m, the range of a constant-velocity approaching target is $R_0 + vmt$ such that the measured pulse $y\,[m]$ in the rage bin at R_0 of the circularly distributed array is

$$\bar{F}\left(\theta,\phi\middle|[m]\right) = \sum_{n=1}^{N} \mathrm{A}\, \underbrace{\mathrm{e}^{\left(2kA\tilde{R}_{n0}\right)}}_{\text{constant}}\, \underbrace{\mathrm{e}^{\left(2kAv_n m\tilde{t}_n\right)}}_{\text{Doppler Sinusoid}} \Big/ N\,. \tag{128}$$

This result assumes the target stays in the same range bin over M pulse repetition intervals implying the stop and hop assumption [42] of Figure 55. Hence, any constant-velocity target has a sinusoidal slot-time phase history and is represented by its slow-time sequence of phase measurements.

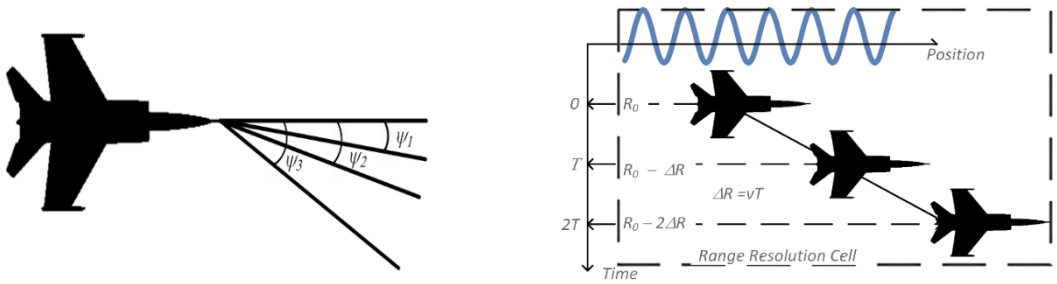

Figure 55. Doppler shift becomes a function of the scan angle. [43] (top) and an illustration of an approaching target (bottom) [43].

8.4 HIGHER ORDER PHASE VARIATIONS

Higher-order phase variations of $f_{d,n}$ relating to acceleration, jerk, and higher-order moments can also be expanded from (125) such that f_r and f_t relate respectively to the received and transmitted frequency components.

$$f_r = \left(1 + v/c\right)\left(1 - v/c\right)^{-1} f_t \tag{129}$$

Also, since v/c is routinely small, this approximates as

$$f_r = (1+v/c)\left[1+(v/c)+(v/c)^2+\ldots\right] f_t \,. \tag{130}$$

where it is seen its first two series truncations provide the intended result of $f_r = (1 + 2\ v / \lambda)\ f_t$.

8.4.1 Expansion of the range-velocity kernel

8.4.1.1 Single element

The range kernel R (t) can be also be expanded such that

$$R(t) = R_0\sqrt{1+x^2} \approx R_0\left[1+x^2/2-3x^4/8+\ldots\right], \mathrm{x} = vt/R_0 \tag{131}$$

Truncating this series gives $R_0 + (v^2 / 2R_0)\ t^2$. Hence, the array factor of (124) becomes

$$\overline{F}(\theta,\phi) = \sum_{n=1}^{N} A(t-2R_n/c)\,\mathrm{e}^{\left(2kA\left(\tilde{R}_n+\left(v_n^2\tilde{t}_n^2\right)/(2R_n)\right)-\omega_{0,n}t_n\right)} \Big/ N \tag{132}$$

This result produces a quadratic phase function and, in essence, represents a Doppler frequency shift that varies linearly with time due to the changing radar-target geometry.

$$f_{d,n}(t) = d\left(-\left(v_n^2/R_n\lambda\right)t^2\right)\Big/dt = -2v_n^2 t/R_n\lambda \,. \tag{133}$$

For an approaching target, the instantaneous Doppler shift is positive. Moreover, this quadratic range case is important in synthetics aperture radar.

This page is intentionally blank.

9. RADAR CROSS SECTION

The relative RCS of a target with N point scatterers can be computed as a function of Ψ and λ using a generalization of the array factor provided in (134):

$$\bar{y}(t) = e^{j2\pi ft} \sum_{i=1}^{N} \sqrt{\sigma_i} e^{-j2R_i(\Psi)/c} \,. \tag{134}$$

The resultant RCS σ is then proportional to $|\bar{y}|^2$ and yields the same form as the mean-valued radiation pattern. However, the aperture size increases from kA to $2kA$.

A physical explanation of the mean-valued radiation pattern can be observed from scanning an antenna amongst a distribution of scatterers. Its resultant RCS σ then becomes the angular convolution of the range-averaged effective reflectivity $\hat{p}(\theta, \phi; R_0)$, evaluated at the range R_0 with a two-way voltage pattern $E^2(\theta, \phi) = EF(\theta,\phi)F(\theta_0,\phi_0)$, where $EF(\theta,\phi)$ is the element factor. [42]

In mathematical notation, the mean value of (135) converges to (124) when scanned over a topology and summed over a main-beam direction at a fixed distance R_0. An example of the RCS of $N = 1000$ – point scatterers is shown in Figure 56 for a uniformly distributed circular distribution with the mean-valued pattern in (136).

$$y(\theta,\phi;R_0) = \hat{\rho}(\theta,\phi;R_0) * \theta * \phi E^2(\theta,\phi) \,. \tag{135}$$

$$\bar{U}(\theta,\phi) \overset{Cir}{=} \begin{matrix} 1/N + (1-1/N)2^2 \\ \neg \mathrm{jinc}(x) = J_1(x)/x \end{matrix} \left[|\mathrm{jinc}(u)|^2 |\mathrm{jinc}(v)|^2 \right] \tag{136}$$

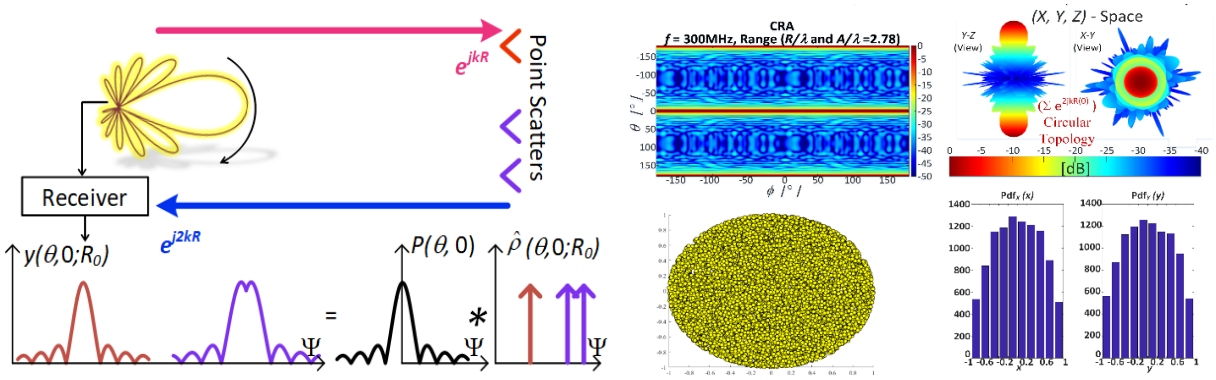

Figure 56. Beampattern of the circular distributed antenna array two-way array factor. Demonstration of the point scatters – left, and mean valued radiation formulation, right.

9.1 EXPERIMENTAL RESULTS

Characteristic function derivations of a circular annular random array (CARA or ring) and multiple rings compounded as a function of M (the number of rings) are thoroughly derived in [21] – [22]. Each aperture radius factor can also be designed to null steer where broadening of the effective null depth is achieved by compounding the subarray factor of its total pattern. A comparison of mean and numerical radiation patterns steered at the meridian elevation and designed to null at 25° for $M = 1$ and $M = 8$ were provided in Figure 21. A multiple ring topology moving radially outward with constant velocity (V) is provided in (137). Its experimental setup is illustrated in Figure 57, an

example of the resulting mean-valued power pattern for M = 2, provided in Figure 58. This solution experiences a degradation factor of Δu and Δv due to the increasing aperture size over time. However, this solution is also seen to enhance resolution when averaged over N_p pulses and reduces to previous works of [21] – [22] for V=0.

$$\bar{U}(\theta,\phi) = \begin{matrix} 1/N + (1-1/N) \\ \neg\mathrm{rinc}(x) = J_0(x) \end{matrix} \left| \frac{1}{N_p M} \sum_{m=1}^{M} \sum_{n_p=1}^{N_p} \mathrm{rinc}\, u_m \, \mathrm{rinc}\, n_p \Delta u \right|^2 \quad \begin{matrix} u_m = 2kA_m\, \hat{\mathrm{x}}\cdot\hat{\Psi}, \;\; \Delta u = 2k\Delta A\, \hat{\mathrm{x}}\cdot\hat{\Psi}, \;\; \Delta A = VT_{PRI} \\ v_m = 2kA_m\, \hat{y}\cdot\bar{\Psi}, \;\; \Delta v = 2k\Delta A\, \hat{y}\cdot\hat{\Psi}, \;\; \hat{\Psi} = \hat{\mathrm{r}}(\theta,\phi) - \hat{\mathrm{r}}(\theta_0,\phi_0), \end{matrix}$$

$$\bar{U}(\Psi) \approx 1/N + (1-1/N)\left|\mathrm{arinc}(2kA\Psi, 2k\Delta A\Psi; m\lambda/d)\right|^2, \mathrm{arinc} = \mathrm{rinc}(2kA\Psi)\,\mathrm{rinc}(2k\Delta A\Psi) * \sum_{m=-\infty}^{\infty} (\Psi - m\lambda/d)$$

(137)

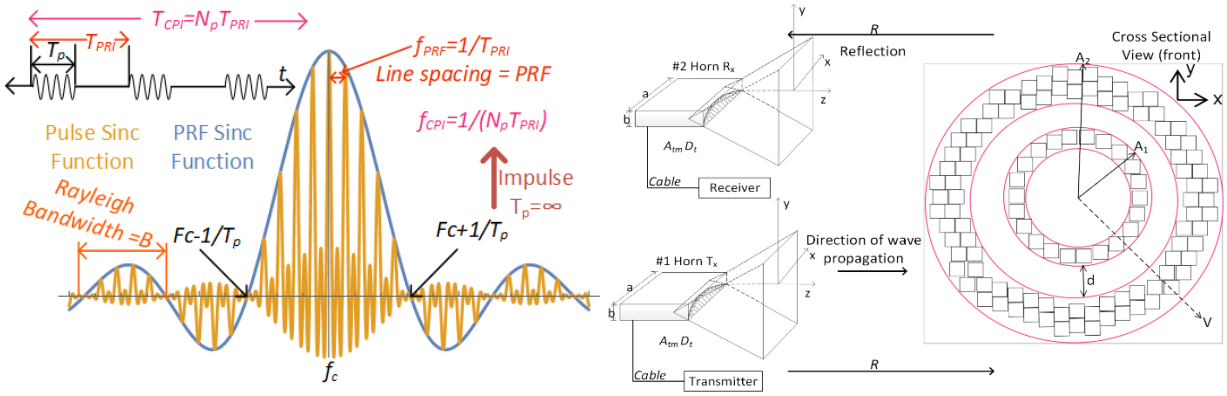

Figure 57. Pulse behavior with N = 5, d = 5 (left) and experimental diagram (right).

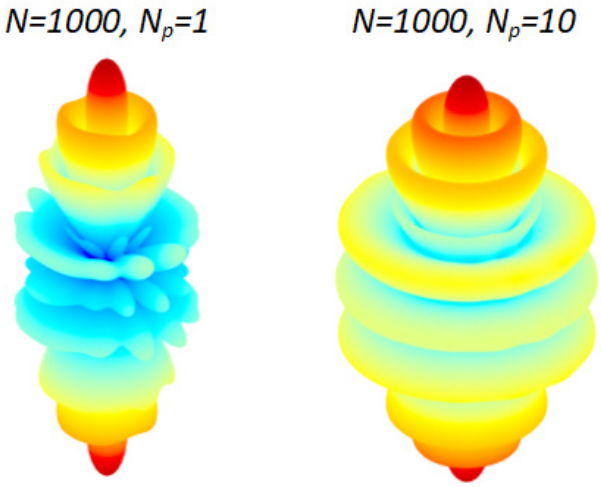

Figure 58. Mean and numerical pattern comparisons of two rings moving radially and outward with constant velocity.

10. POINT SPREAD FUNCTION

A synthetic aperture radar (SAR) imaging problem in nature is solved using Fourier analysis. For example, a nominal Fourier transformer is a *lens* and the "method of stationary phase" is the central analytical tool used for the asymptotic expansion of Fourier integrals. Its analysis is rooted in the Huygens-Fresnel principle and involves linear operations of sinusoidal basis functions transformed from the original function. The original concepts of Fourier analysis have been extended over time to apply to more abstract and general field situations, often known as harmonic analysis.

In application, (SAR) algorithms involve Fourier analysis, either explicitly or implicitly. However, solutions cannot be applied to the SAR Fourier integral by means of traditional residue theory, as the integrand function has no singularities and is not meromorphic. It takes the form of exp(z), implying holomorphic and analytic everywhere. Hence, it termed an entire function and was confirmed by Cauchy-Riemann equations. We solve the SAR Fourier problem in a role comparable to optics and vision science techniques in application. [44]

10.1 PROBLEM FORMULATION

The SAR Fourier integral is provided in (138) and approximated by the method of stationary phase. Asymptotic expansion as k_x approaches infinity of the slant-plane Fourier integral (hyperbolic chirp signal) is often called the range migration algorithm or $\omega - k$ algorithm.

$$\int_{-\infty}^{\infty} \exp\left[-j2k_r\sqrt{x_n^2+(y_n-u)^2}-k_x u\right]du \approx \exp\left[-j\sqrt{4k_r^2-k_x^2}\,x_n - jk_x y_n\right] \tag{138}$$

In two dimensions, the asymptotic expansion may be written as (139) where the target informative part k_z, k_x is the range spatial frequency, and k_y is the cross-range spatial frequency. This result is traditionally computed using the fast Fourier transform (FFT). The identity $k_z = \sqrt{4k_r^2 - k_x^2 - k_y^2}$ is known as a stolt transformation. The inverse Fourier transform is provided (140) with an ideal response of (141).

$$\begin{aligned} &SS(\omega,k_x,k_y) = \int_{-\infty}^{\infty}\int_{-\infty}^{\infty}\sigma_n \exp\left[-j2k_r\sqrt{(x_n-u)^2+(y_n-v)^2+z_n^2}-k_x u-k_y v\right]dudv \\ &\approx \exp[-jk_z z_n]\sum_n F(k_x,k_y),\ \ F(k_x,k_y) = \sum_n \sigma_n \exp\left[-jk_x x_n - jk_y y_n\right] \\ &k_z = \sqrt{4k_r^2-k_x^2-k_y^2} \rightarrow \sqrt{k_x^2+k_y^2} \le 2k_r \end{aligned} \tag{139}$$

$$f(x,y) = \frac{1}{2\pi^2}\int_{-\infty}^{\infty}\int_{-\infty}^{\infty}\exp(-jk_x x_n - jk_v y_n)\exp(jk_x x + jk_y y)\,dk_x dk_y \tag{140}$$

$$f(x,y) = 1/(2\pi^2)\sum_n \sigma_n \delta(x-x_n)\delta(y-y_n) \tag{141}$$

The stationary point target in the imaging scene of Figure 59 is located at (x_n, y_n, 0), and the coordinates of the center of the target area are at (x_n, y_n, 0) such that $x_n = y_n = 0$ for broadside (nadir) imaging. The ideal target function in the $x - y$ plane may then be defined as (142) with ideal spatial Fourier transform of the ideal target function of (143). Parameters k_x and k_y are the Fourier domain's spatial frequency corresponding to x range and y cross-range, respectively.

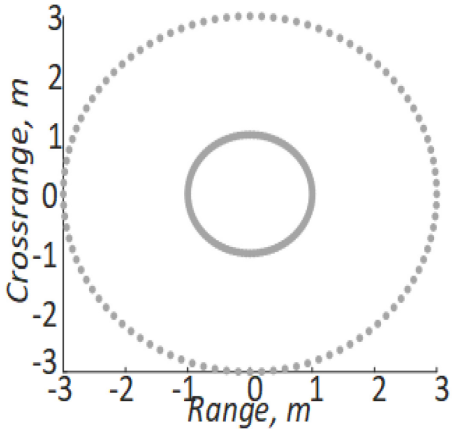

Figure 59. The distribution of 200-point scatters is uniformly distributed and split equally amongst each ring.

$$f_0(x,y) = \sum_n \sigma_n \delta(x - x_n)\delta(y - y_n) \tag{142}$$

$$F_0(k_x,k_y) = \sum_n \sigma_n \exp(-jk_x x_n - jk_y y_n) \tag{143}$$

This result implies a point target x_n and y_n has a Fourier transform that creates a complex sinusoid with a frequency proportional to the shift. "Images of point scatterers provide insight into the achievable effectiveness of exploitation algorithms given a variety of operating parameters such as elevation angle, azimuth or synthetic aperture extent, and frequency bandwidth." [47]

$$\underset{\text{Infinitely localized}}{\delta(x - x_n)} \leftrightarrow \underset{\text{Infinitely Broadband}}{\exp(-jx_n k_x)} \tag{144}$$

However, the condition $(k_x^2+k_y^2)^{1/2} \le 2k_r$ and zero otherwise signifies a disk-shaped limited spatial Fourier support for k_x and k_y. Therefore we derive its joint density function as (145) and marginal distributions of (146).

$$f(k_x,k_y) = \int_0^{2\pi}\int_0^{2k_\omega} k_\rho dk_\rho d_\phi = 2\pi k_\omega^2 \tag{145}$$

$$f(k_x) = \int_{-\sqrt{2k_\omega^2-k_x^2}}^{\sqrt{2k_\omega^2-k_x^2}} f(k_x,k_y)dk_x = \frac{1}{2\pi k_\omega^2}\sqrt{2k_\omega^2 - k_x^2} \tag{146}$$

It is easy to show that the resulting point spread function is provided (147).

$$\begin{aligned} \Lambda &= \int_{-\infty}^{\infty}\int_{-\infty}^{\infty} \exp\left[-jk_x(x_n - x) - jk_y(y_n - y)\right] f(k_x) f(k_y) dk_x dk_y \\ f_n(x,y) &= \frac{1}{K} + \left(1 - \frac{1}{K}\right) 4 \left| \frac{J_1(2k_\omega(x_n - x))}{k_\omega(x_n - x)} \frac{J_1(2k_\omega(y_n - y))}{k_\omega(y_n - y)} \right|^2, \sqrt{k_x^2 + k_y^2} \le 2k_\omega \end{aligned} \tag{147}$$

If the point reflector's bandwidth is limited in the fast-time frequency domain with a constant donut-shaped band of frequency spectral support $\omega \in \omega_{min}, \omega_{max}$ its point spread function in the spatial domain becomes (148).

$$f_n(x,y)=\frac{1}{K}+\left(1-\frac{1}{K}\right)\left|\begin{matrix}2\left(\left(\tilde{A}_o k_{\omega\max}J_1\left(\tilde{A}_o k_{\omega\max}\left(x_n-x\right)\right)-\tilde{A}_i k_{\omega\min}J_1\left(\tilde{A}_{i,s} k_{\omega\min}\left(x_n-x\right)\right)\right)\Big/\left(\tilde{A}_o^2 k_{\omega\max}-\tilde{A}_i^2 k_{\omega\min}\right)\right)\\ 2\left(\left(\tilde{A}_o k_{\omega\max}J_1\left(\tilde{A}_o k_{\omega\max}\left(y_n-y\right)\right)-\tilde{A}_i k_{\omega\min}J_1\left(\tilde{A}_{i,s} k_{\omega\min}\left(y_n-y\right)\right)\right)\Big/\left(\tilde{A}_o^2 k_{\omega\max}-\tilde{A}_i^2 k_{\omega\min}\right)\right)\end{matrix}\right|^2 \tag{148}$$

$$f_n(x,y)=\frac{1}{K}+\left(1-\frac{1}{K}\right)\left|J_0\left(k_{\omega\max}\left(x_n-x\right)\right)J_0\left(k_{\omega\max}\left(y_n-y\right)\right)\right|^2 \tag{149}$$

Solutions to (147) and (148) are also known as Sombrero, Besinc, or Jinc functions. The solution (148) is similar to the results provided in [46] but provides pattern multiplication amongst the x and y distributions. [14] – [15]. Examples of the band-limited spectral support of two circularly distributed ring distributions are illustrated in Figure 60.

The mean valued radiation pattern of (147) – (149) is demonstrated in Figure 61 with and uniform amplitude in two different distributions, a common linear distribution amongst the x-axis ($x_n \in [-1,1]$ and $y_n=0$) with the analytical solution of (150) and a parabolic amplitude distribution. A comparison of Figure 56 shows its tapering capability, similar to tapered aperture distributions.

$$f(x,y)=\frac{1}{k_r}\left(-\frac{1}{2}k_r(-1+x)\,{}_1F_2\left(\frac{1}{2};\frac{3}{2},2;-\frac{1}{4}k_r^2(-1+x)^2\right)+\frac{1}{2}k_r(1+x)\,{}_1F_2\left(\frac{1}{2};\frac{3}{2},2;-\frac{1}{4}k_r^2(1+x)^2\right)\right) \tag{150}$$

10.2 CONCLUSION

This paper derives the point spread function for the n^{th} target using circularly distributed spectral support. Results display similarities to expected radiation patterns of randomly distributed antenna arrays of [3] – [15].

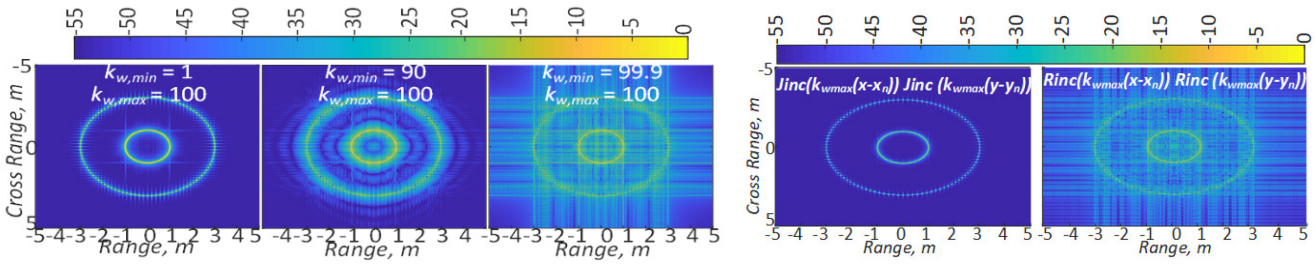

Figure 60. Imaging of two circularly distributed rings of variable radii, A_1 = 1 and A_2 =3. Equation (148) – left three images and equations (147) – the second image from the right and (150) – right.

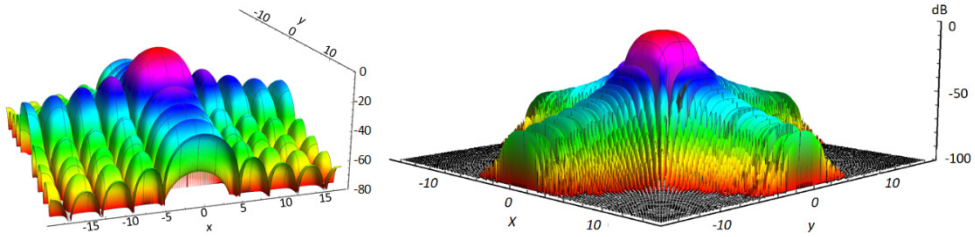

Figure 61. Uniform amplitude distribution, top, and parabolic amplitude distribution, bottom.

This page is intentionally blank.

11. TURNTABLE ISAR

Turntable inverse synthetic aperture radar (ISAR) has a rich history with many significant connections recognized in antenna theory, Fourier analysis, sampling theory, remote sensing inverse problems, medical tomography, imaging, synthetic apertures, radar signals, range and doppler, and signal processing. Most ISAR and synthetic aperture radar (SAR) theory has been derived from perspectives of approximations imposed upon the signal models. Consequently, most literature focuses on overcoming these artificial limitations that are inherently due to imposed approximations. Our work analyzes these approximations differently with the use of statistical characterization. In doing so, we create expected patterns of the ISAR data.

11.1 INTRODUCTION

Imaging, visualizing, and analyzing moving targets is considerably more challenging in comparison to stationary targets. Inverse synthetic aperture radar (ISAR) is a traditional imaging technique. The conventional approach begins by removing the target's radial motion via motion compensation (MoCo) techniques. Next, the same methods are applied for ISAR imaging or turntable radar imaging. The technique provides high cross-range resolution and wide signal bandwidth due to the rotational motion but fails to improve imaging performance. [49] The limitation arises from the convolution of target scattering and the point spread function (PSF). In general, the composite resolution of most algorithms is aimed at locating bright light targets. [50] – [66]

Image processing with a stepped-frequency waveform is a simple 2D direct Fourier transform (DFT). Returns from dominant scatterers are processed and coherently integrated to provide the high-resolution range (HRR) profile, whereas the cross-range resolution is imaged due to the turntable's rotational motion.

11.2 PROBLEM FORMULATION

In stepped radar imaging, the l^{th} pulse frequency is given by (151) , and the ideal range resolution of the cell is given by (152) where τ is the pulse width.

$$f_k = f_c + (l-1)\Delta F \tag{151}$$

$$\Delta r_{orig} = c\tau/2 \tag{152}$$

Instantaneous bandwidth (153) is determined by the product of the number of pulses N and the frequency step size ΔF.

$$\Delta r = \left(c/B_{eff}\right), \qquad B_{eff} = N\Delta F \tag{153}$$

Thus, an increase in bandwidth results in finer range resolution. Standard design parameters of frequency-stepped waveform imaging are provided in [49], Table 3.1.

11.3 TURNTABLE ISAR IMAGING

Consider a traditional monostatic radar measurement setup in Figure 62, which consists of a transmitting and receiving antenna and is used to measure a turntable target that rotates uniformly in

time by steps of $\Delta\phi$. The echo, reflected from the target of a stepped frequency waveform can be represented as [67]

$$y(l,m)=\sigma(x_n,y_n)\exp\left(-j4\pi f_l R(n)/c\right),\ f_l=f_0+l\Delta f$$
$$R(n)=R(l+mP) \tag{154}$$

Where frequencies are increasing by $l=\{0, 1, \ldots, L\}$ of total bandwidth $L\Delta f$. Sample bursts are recorded as $(l+mP)T_s$, of index m (L frequencies plus dead time), P steps, and T_s is the time between frequency samples.

For simplicity, we assume a uniformly distributed scattering surface such that $\sigma(x_n, y_n)=1$. Then the Euclidean distance of the phase factor (154) for every scattering coefficient of the target on the imaging grid (x_n, y_n, and $z\approx z_n=0$) is written as:

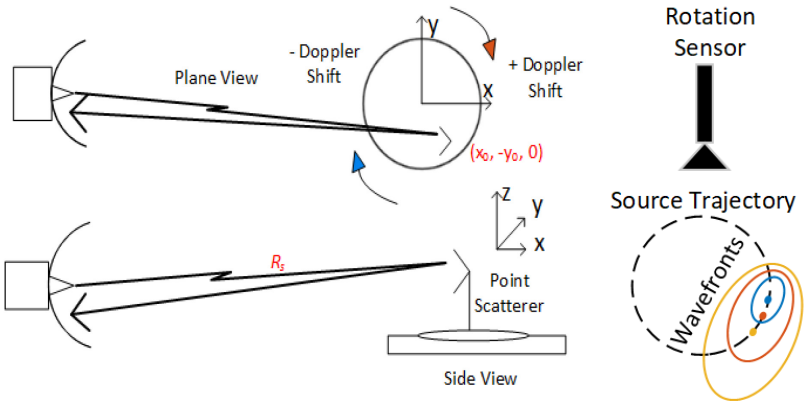

Figure 62. Turntable inverse synthetic aperture radar scanning system.

$$R(n)=R_s\sqrt{1+\left(r_n/R_s\right)^2+2r_n\cos\psi_n/R_s},\cos\psi_n=\hat{r}\cdot\hat{r}_n\ . \tag{155}$$

This result can be expanded by traditional means of the binomial expansion (156) where R_s is the distance to center scatterer and adjusted from the multiplication of the turntable's rotation (157). The resulting distance is rewritten in common the common u, v notation of (158) and further simplified for overall compactness and simplicity in primed coordinates (159).

$$R(n)=R_s\sqrt{1+\mathrm{X}^2-2\mathrm{X}\cos\psi_n}\approx\sum_{m=0}^{N}r\binom{1/2}{m}R_s\left(\mathrm{X}^2-2\mathrm{X}\cos\psi_n\right)^n$$
$$\mathrm{X}=r_n'/R_s,R_n\big|_{N=1}=R_s-r_n'\cos\psi_n+r_n'^2/2R_x \tag{156}$$

$$R(n)\approx R_s-r_n\cos\psi_n$$
$$r_n\cos\psi_n=r_n\left(\hat{r}^T R(n\Delta\phi)\hat{r}_n\right),\quad \cos\psi_n\equiv\left(\hat{r}^T R(n\Delta\phi)\hat{r}_n\right)=r_n\left[\sin\theta\cos\phi\quad\sin\theta\sin\phi\right]\begin{bmatrix}\cos n\Delta\phi & -\sin n\Delta\phi\\ \sin n\Delta\phi & \cos n\Delta\phi\end{bmatrix}\begin{bmatrix}\sin\theta_n\cos\phi_n\\ \sin\theta_n\sin\phi_n\end{bmatrix} \tag{157}$$

$$R(n)\approx R_s-x_n\left(\cos n\Delta\phi+\sin n\Delta\phi\right)u-y_n\left(\cos n\Delta\phi-\sin n\Delta\phi\right)v$$
$$u=\sin\theta\cos\phi, v=\sin\theta\sin\phi \tag{158}$$

$$R(n)=\left(R_s-\begin{pmatrix}x_n^{'}\cos(l+mP)\Delta\phi+\\ y_n^{'}\sin(l+mP)\Delta\phi\end{pmatrix}\right),\ \begin{matrix}x_n^{'}=\left(x_n\cos(l+mP)\Delta\phi-y_n\sin(l+mP)\Delta\phi\right)\sin\theta\cos\phi\\ y_n^{'}=\left(x_n\cos(l+mP)\Delta\phi+y_n\sin(l+mP)\Delta\phi\right)\sin\theta\sin\phi\end{matrix} \tag{159}$$

We can shift the focus to the turntable center by multiplying the data by the reference phase delay to produce (160), revealing that these are samples of the Fourier transform of an impulse on a polar grid upon the imaging plane (161).

$$y_{x_0=0,y_0=0}(l,m)=\exp\left(j\frac{4\pi}{c}(f_0+l\Delta f)R_s\right) \tag{160}$$

$$\begin{gathered}y(l,m)=\exp\left(-j\begin{pmatrix}\left(x_nk_x-y_nk_y\right)\sin\theta\cos\phi+\\ \left(x_nk_y+y_nk_x\right)\sin\theta\sin\phi\end{pmatrix}\right)\\ f_x=f_l\cos\left(\Delta\phi(t)\right),f_y=f_l\sin\left(\Delta\phi(t)\right),\ k_x=4\pi f_x/c,\ k_y=4\pi f_y/c,\Delta\phi(t)=(l+mP)\Delta\phi\end{gathered} \tag{161}$$

Equation (161) is known as the projection-slice formulation from tomography and used to justify PFA (polar formatting algorithm). The result of (161) is also expanded from its primed coordinates as

$$\begin{gathered}y(l,m)=\exp\left(-j\frac{4\pi}{c}(f_0+l\Delta f)\begin{pmatrix}x_n^{'}\sin\theta\cos\phi+\\ y_n^{'}\sin\theta\sin\phi\end{pmatrix}\right)\\ y(l,m)=\exp\left\{-jx_n^{'}k_x\sin\theta\cos\phi\right\}\exp\left\{-jy_n^{'}k_y\sin\theta\sin\phi\right\}\end{gathered}\ . \tag{162}$$

We use the first-order trigonometric approximations to reduce (162) to (163) implying turntable rotation $l\Delta\phi$ is negligible during each burst.

$$y(l,m)=\exp\left\{\frac{-j4\pi(f_0+l\Delta f)}{c}\left((x_n-y_nmP\Delta\phi)\sin\theta\cos\phi\right)\right\}\exp\left\{\frac{-j4\pi(f_0+l\Delta f)}{c}\left((x_nmP\Delta\phi+y_n)\sin\theta\sin\phi\right)\right\} \tag{163}$$

The cross-terms in l and m are ignored, and the 2D DFT is expanded as several terms below and normalized to the largest dimension of the turntables aperture A,

$$\begin{gathered}y(l,m)=\exp\left\{-j\frac{4\pi}{c}Af_0\tilde{x}_n\sin\theta\cos\phi\right\}\exp\left\{-j\frac{4\pi}{c}Af_0\tilde{y}_n\sin\theta\sin\phi\right\}\\ \exp\left\{\underbrace{-j\frac{4\pi}{c}Al\Delta f\tilde{x}_n\sin\theta\cos\phi}_{Downrange}\right\}\exp\left\{\underbrace{+j\frac{4\pi}{c}Af_0\tilde{y}_nmP\Delta\phi\sin\theta\cos\phi}_{Crossrange}\right\}\\ \exp\left\{\underbrace{-j\frac{4\pi}{c}Al\Delta f\tilde{y}_n\sin\theta\sin\phi}_{Downrange}\right\}\exp\left\{\underbrace{-j\frac{4\pi}{c}Af_0\tilde{x}_nmP\Delta\phi\sin\theta\sin\phi}_{Crossrange}\right\}\\ \tilde{x}_n=x_n/A,\quad \tilde{y}_n=y_n/A\end{gathered} \tag{164}$$

11.4 TURNTABLE BEAMSTEERING

The expected value of the frequency spectrum echo (164) is thereby written as (165) for a ring distribution uniformly distributed on the turntable [14]:

$$\bar{F}(l,m,\theta,\phi)=\begin{pmatrix} Rinc(2kAu)\,Rinc(2kAv) \\ Rinc(2\Delta kAu(l))\,Rinc(2\Delta kAv(l)) \\ Rinc(2kAu(mP\Delta\phi))\,Rinc(2kAv(mP\Delta\phi)) \end{pmatrix} \Big/ N, \begin{Bmatrix} \Delta k = 2\pi\Delta f/c \\ u=\sin\theta\cos\phi-\sin\theta_0\cos\phi_0 \\ v=\sin\theta\sin\phi-\sin\theta_0\sin\phi_0 \end{Bmatrix} \quad (165)$$

where u, v space is modified in post-processing to steer the ISAR main beam behavior in the direction θ_0, ϕ_0. This result can also be applied to (164) in a traditional beamforming sense if one multiplies by the phase compensation factor, $\exp(-jk\, r_n \cos(\psi_{n0}))$.

12. CONCLUSION

The random array's general statistics are seen to converge such that ideal statistical values of sparse random array populations can be generalized, regardless of distribution or topology, similar to what is described in [19]. Second, this work has analyzed the maximum peaking sidelobe in a rigorous statistical sense for beamsteering in either the meridian elevation angle (endfire) or zenith elevation angle (broadside). This method's results appear to be very accurate when applied far enough away from the main beam such that characteristic function has monotonically decayed into the 3dB sidelobe region. Moreover, this theory provides greater accuracy than the popular Rayleigh approximation since inaccuracy occurs for large element populations.

This work has also provided a limiting bound for the maximum peaking sidelobe (no greater than 12 dB above the average sidelobe level out to aperture sizes spanning A/λ=100). Third, the gain of a periodic array was shown to be capable of reaching values of $2N$ but provides limited scan capability. By contrast, sparse aperiodic arrays converge to N with scan capability. This result also makes the random array invariant to element spacing as well as frequency independent, thus providing greater bandwidth capability. Finally, the probability moments are shown to completely describe the array factor of a random distribution such that ideal statistics were generalized for any random array type regardless of distribution or geometrical bound.

This page is intentionally blank.

REFERENCES

1. A. Panicali, and L. Yuen, 1969, “A probabilistic approach to large circular and spherical arrays,” *IEEE Transactions on Antennas and Propagation*, vol. 17, pp. 514–522.
2. T. A. Dzekov, and R. S. Berkowitz, 1978 “Parameters of a spherical random antenna array,” in *Electronics Letters.*, vol. 14, no. 16, pp. 495–496.
3. H. Ochiai, 2005 “Collaborative beamforming for distributed wireless ad hoc sensor networks,” *IEEE Transactions on Signal Processing.*, vol. 53, pp. 4110, November.
4. M. F. A. Ahmed, and S. A. Vorobyov, 2009 “Collaborative beamforming for wireless sensor networks with Gaussian distributed sensor nodes,” *IEEE Transactions on Wireless Communications*, vol. 8, pp. 638–643.
5. P. Nelson, F. Fazi, K. Holland, and T. Takeuchi, 2010 “Inverse problems and sound reproduction,” in *ISVR Abisonics Symposium*, Paris FR, March, 2010.
6. K. Buchanan, O. Sternberg, S. Wheeland, and J. Rockway, 2017 “Examination of the near field response of circular antenna arrays,” in *United States National Committee of URSI National Radio Science Meeting* (USNC-URSI NRSM), Boulder, CO, January. 2017, pp. 1(2.
7. K. Buchanan, C. Flores-Molina, O. Sternberg, D. Overturf, S. Wheeland, and N. Johnson, 2017 “Near-field receive beamforming analysis using circularly distributed random arrays,” in *IEEE International Symposium on Antennas and Propagation.*, San Diego, pp. 1591.
8. C. A. Balanis, 2005 “Antenna Theory: Analysis and Design” 3rd edition, New York: John Wiley & Sons, Inc.
9. N. Peccarelli, B. James, R. Irazoqui, J. Metcalf, C. Fulton and M. Yeary, 2019 “Survey: Characterization and Mitigation of Spatial/Spectral Interferers and Transceiver Nonlinearities for 5G MIMO Systems,” *IEEE Transactions on Microwave Theory and Techniques*.
10. G. Galati, S. Perna, and M. Abbati, 1992 “Quasibistatic random arrays,” in *IEEE Proc. F Radar and Signal Process.*, vol.139, pp.193, June
11. W.J. Hendricks, 1991 “The totally random versus the bin approach for random arrays,” *IEEE Transactions on Antennas and Propagation,* vol.39, pp.1757–1762.
12. D. Overturf, K. Buchanan, J. Jensen, C. Flores-Molina, S. Wheeland and G. H. Huff, 2017 “Investigation of beamforming patterns from volumetrically distributed phased arrays,” in *IEEE Military Communications Conference* (MILCOM), Baltimore, MD, October 2017, pp. 817–822.
13. K. Buchanan and G. Huff, 2011, “A comparison of geometrically bound random arrays in Euclidean space,” in *IEEE Antennas and Propagation. Society International Symposium*, Spokane, WA, pp. 3–8.
14. K. R. Buchanan, 2014 “Theory and applications of aperiodic (random) phased arrays,” Ph.D. dissertation, Department of Electrical and Computer Engineering, Texas A&M University.
15. K. Buchanan and G. Huff, 2014, “A stochastic mathematical framework for the analysis of spherically bound random arrays,” *IEEE Transactions on Antennas and Propagation,* vol. 62, pp. 3002–3011.
16. D. Yavuz, 1979 “Frequency response and bandwidth of a spherical random array,” in *Electronics Letters*, vol. 15, no. 11, pp. 314–315.
17. L. Lewin, 1979 “Comment Analytic expression for the frequency response and bandwidth of a spherical random array,” in *Electronics Letters* vol 15. no. 19, pp. 585–586

18. K. Buchanan, C. Flores, S. Wheeland, J. Jensen, D. Grayson, and G. Huff, 2017 “Transmit beamforming for radar applications using circularly tapered random arrays,” in *IEEE Radar Conference* (RadarConf), Seattle, WA, 2017, pp. 0112–0117.
19. B. D. Steinberg, Principles of Aperture & Array System Design. New York: Wiley, 1976.
20. Y. Lo, 1964 “A mathematical theory of antenna arrays with randomly spaced elements,” *IEEE IEEE Transactions on Antennas and Propagation*, vol. 12, pp. 257–268, May 1964.
21. K. Zarifi, A. Ghrayeb, and S. Affes, 2010 “Distributed beamforming for wireless sensor networks with improved graph connectivity and energy efficiency,” *IEEE Transactions on Signal Processing*, vol., 58, pp. 1904–1921, March 2010.
22. K. Buchanan and C. Flores-Molina, 2016 “Investigation of a novel subarray nullsteering technique for distributed random arrays,” in *IEEE Antennas and Propag. Int. Symp.*, Fajardo, Puerto Rico, 2016, pp. 1677–1678.
23. W. Feller, 1971 “An Introduction to Probability Theory and Its Applications,” 2nd Ed, New York: John Wiley & Sons.
24. F. W. J. Olver, D. W. Lozier, R. F. Boisvert, and C. W. Clark, 2010 editors, NIST Handbook of Mathematical Functions, New York: Cambridge University Press.
25. L. Leemis and J. McQueston, 2008 “Univariate distribution relationships,” American Statistician, vol. 62, pp. 45–53, February 2008.
26. Y. Lo and R. Simcoe, 1967 “An experiment on antenna arrays with randomly spaced elements,” *IEEE Transactions on Antennas and Propagation*, vol. 15, pp. 231–235, March 1967.
27. K. R. Buchanan, 2011 “A study of aperiodic (random) arrays of various geometries” M.S. thesis, Department Electrical and Computer Engineering, Texas A&M University, TX, 2011.
28. M. F. A. Ahmed and S. A. Vorobyov, “Beampattern random behavior in wireless sensor networks with Gaussian distributed sensor nodes,” *in IEEE Canadian Conference on Electrical and Computer Engineering*, Niagara Falls, ON, 2008, pp. 257–260.
29. R. E. Blahut, 2004 “Theory of Remote Image Formation.” New York: Cambridge University Press,
30. B. McKellar, M. Box, and E. Love, 1983 “Inversion of the Struve transform of half-integer order,” *Journal of the Australian Mathematical Society*, vol. 25, pp. 161–174.
31. K. Buchanan, J. Rockway, O. Sternberg and N. N. Mai, 2016 “Sum-difference beamforming for radar applications using circularly tapered random arrays,” in *IEEE Radar Conference*, Philadelphia, PA, pp. 1–5.
32. M. Donvito and S. Kassam, 1979 “Characterization of the random array peak sidelobe,” *IEEE Transactions on Antennas and Propagation*, vol. 27, pp. 379-385, May 1979.
33. V. Agrawal, and Y. T. Lo, 1980 “Comments on “Characterization of the random array peak sidelobe,” IEEE Transactions on Antennas and Propagation, vol.28, pp.946, 948, November 1980.
34. V. Agrawal and L. Yuen, 1972, “Mutual coupling in phased arrays of randomly spaced antennas,” *IEEE Transactions on Antennas and Propagation*, vol. 20, pp. 288–295, May 1972.
35. B. D. Steinberg, 1973 “Comparison between the peak sidelobe of the random array and algorithmically designed aperiodic arrays,” *IEEE Transactions on Antennas and Propagation*, vol.21, pp.366-370, May 1973.
36. V. D. Agrawal and Y. T. Lo, 1969 “Distribution of sidelobe level in random arrays,” in *Proceedings of the IEEE*, vol. 57, no. 10, pp. 1764–1765, October 1969.

37. B. D. Steinberg, 1983 “Sidelobe reduction of random arrays by element position and frequency diversity,” *IEEE Transactions on Antennas and Propagation*, vol. 31, pg. 922–931, November 1983.
38. B. D. Steinberg, “The peak sidelobe of the phased array having randomly located elements,” *IEEE Transactions on Antennas and Propagation* vol. 20, pp. 129–136, March 1972.
39. R. Hansen, 1998 “Phased Array Antennas,” New York: Wiley.
40. M. Jarrell. 2001 “Radiation” in Lecture Notes [Online]. Available: http://www.phys.lsu.edu/~jarrell/COURSES/ELECTRODYNAMICS/Chap9/chap9.pdf
41. T. Adeyemi and K. Buchanan, 2016 “Frequency diverse scanning for aperiodic (Random) antenna arrays,” in *IEEE Transactions on Antennas and Propagation International Symposium,* Fajardo, Puerto Rico, 2016, pp. 923-924.
42. M. Richards, 2014 “Fundamentals of Radar Signal Processing,” New York, NY: McGraw-Hill.
43. F16 fighter jet Free Photo [Online], Available: https://www.freepik.com/free-photo/f16-fighter-jet_528952.htm
44. A. B. Watson, 2015 “Computing human optical point spread functions,” *Journal of Vision,* vol. 15, no. 2, pp. 26, 2015.
45. E. G. Zelino, 2010 “Algorithms for Synthetic Aperture Radar Imagery XVII,” in *Proc. SPIE*, vol. 7699, April 2010.
46. M. Soumekh, 1999 “Synthetic aperture radar signal processing with MATLAB algorithms,” Canada, John Wiley & Sons, Inc.
47. L. Moore, and U. Majumder, 2010 “An analytical expression for the three-dimensional response of a point scatterer for circular synthetic aperture radar,” in *Proc. SPIE Algorithms Synthetic Aperture Radar Imagery XIV*, 2010, pp. 1–12
48. M. Soumekh, 1992 “A system model and inversion for synthetic aperture radar,” *IEEE Trans. Image Process*., vol. 1, no. 1, pp. 64–76, January 1992.
49. A. Paulose, 1994 “High Radar Range Resolution with the Step Frequency Waveform,” June 1994.
50. X. Lu, J. Xia, Z. Yin, and W. Chen, 2017 “High-Resolution Turntable Radar Imaging via Two-Dimensional Deconvolution with Matrix Completion. Sensors,” in *Sensors*, vol. 17, 2017.
51. C. F. Barnes, and S. Prasad, 2018 “In Sit Volumetric SAR,” in *IEEE Transactions on Geoscience and Remote Sensing*, vol. 56, no. 10, pp. 6082–6100, October 2018.
52. C. F. Barnes, 2015 “*Synthetic Aperture Radar, Wave Theory Foundations*, *Analysis, and Algorithms.”* Powder Springs, GA, USA: Barnes, 2015.
53. W. G. Carrara, R. S. Goodman, and R. M. Majewski, 1995 “*Spotlight Synthetic Aperture Radar: Signal Process. Algorithms”*. Boston, MA, USA: Artech House, 1995.
54. C. V. Jakowatz, Jr., D. E. Wahl, P. H. Eichel, D. C. Ghiglia, and P. A. Thompson, 1996 “*Spotlight-Mode Synthetic Aperture Radar: A Signal Processing. Approach”*. Boston, MA, USA: Kluwer, 1996.
55. C. Maier, W. Pannert, W. Waidmann, “Localization of Rotating Sound Sources Using Time Domain Beamforming Code,” Engineering Applications of Computational Fluid Dynamics. Advanced Structured Materials, vol 44. Springer Publishing Company.
56. P. Sijtsma, S. Oerlemans, H. Holthusen, “2001Location of rotating sources by phased array measurements,” National Aerospace Laboratory, vol. 6, pp. 2001–2167, 2001.

57. C. Horváth, and B. Tóth, 2016 “Separating Apart the Contributions from Multiple Tonal Noise Sources Which Are Localized to The Mach Radius,” in *Berlin Beamforming Conference*, Berlin, February 2016.
58. M., Nicholas & S., Hao, 2016, “Generalized recovery algorithm for 3D super-resolution microscopy using rotating point spread functions,” *Scientific Reports*, vol. 6.
59. C. Roider, J. Alexander, & S. Bernet and M. Ritsch-Marte, 2014 “Axial super-localization using rotating point spread functions shaped by polarization-dependent phase modulation,” in *Optics express* vol. 22, pp. 4029–4037.
60. H. E. Camargo, 2010 “A frequency-domain beamforming method to locate moving sound source,” dissertation, Virginia Polytechnic Inst. and State University, May 2010, Blacksburg, Virginia.
61. X. Hu, N. Tong, S. Ding, X. He, and X. Zhao, 2016 “ISAR imaging with sparse stepped frequency waveforms via matrix completion,” in. *Remote Sensing Letters*, vol. 7, no. 9, pp. 847–854, June 2016.
62. T. Kempf, M. Peichl, S. Dill, and H. Suess, 2007 “3D tower-turntable ISAR imaging,” in *In Proceedings of European Radar Conference*, October 2007, pp. 114–117.
63. K. Suwa, K. Yamamoto, M. Iwamoto, and T. Kirimoto, 2008 “Reconstruction of 3-D target geometry using radar movie,” in *Proceedings of European Conference on Synthetic Aperture Radar*, 2008, pp. 149–152.
64. T. Cooke, 2003 “Ship 3D model estimation from an ISAR image sequence,” in *Proceedings of IEEE National Radar Conference* September 2003, pp. 36–41.
65. K. Suwa, T. Wakayama, and M. Iwamoto, 2009 “Estimation of target motion and 3D target geometry using multistatic ISAR movies,” in *Proceedings of IEEE International Geoscience and Remote Sensing Symposium*, July 2009, vol. 5, pp. V–429–V–432.
66. Suwa, K., Wakayama, T., Iwamoto, M.: 2011 “Three-dimensional target geometry and target motion estimation method using multistatic ISAR movies and its performance,” *IEEE Transactions on Geoscience and Remote Sensing,* 49, (6), pp. 2361–2373.
67. S. D. Fisher, M. A. Richards, and G. A. Showman, 2004 “An inverse polar format algorithm for turntable spotlight ISAR imaging systems using stepped frequency waveforms,” in *Proceedings of the 2004 IEEE Radar Conference*, Philadelphia, PA, USA, 2004, pp. 212–217.

APPENDIX A
SPHERICAL HARMONIC SOLUTIONS FOR THE HOMOGENOUS HELMHOLTZ EQUATION (REGULAR SPHERICAL EIGENFUNCTIONS OF THE HELMHOLTZ EQUATIONS)

A-1 OVERVIEW

Add in the overview of what is being shown in this Appendix here. Use the same format shown here for Appendices B and C

The inhomogeneous Helmholtz wave equation is conveniently solved using a Green's function, $G(\vec{r}, \vec{r}')$ that satisfies (A-1)

$$\left(\nabla^2 + k^2\right) G\left(\vec{r}, \vec{r}'\right) = -\delta\left(\vec{r} - \vec{r}'\right) = -\frac{\delta(r - r')}{rr' \sin\theta} \delta(\theta - \theta') \delta(\phi - \phi') \tag{A-1}$$

It is possible to use any linear combination of the four radial functions that satisfy the Helmholtz equation. By this means, the Green's function will be bounded everywhere, and one may assume (A-2)

$$\begin{aligned} G\left(\vec{r}, \vec{r}'\right) &= \sum_{l=0}^{\infty} \sum_{m=-l}^{l} A_{lm} j_l(kr') h_l^{(1)}(kr) Y_{lm}(\theta, \phi) Y_{lm}^*(\theta, \phi) \quad for \ r > r' \\ G\left(\vec{r}, \vec{r}'\right) &= \sum_{l=0}^{\infty} \sum_{m=-l}^{l} A_{lm} j_l(kr) h_l^{(1)}(kr') Y_{lm}(\theta, \phi) Y_{lm}^*(\theta, \phi) \quad for \ r < r' \end{aligned} \tag{A-2}$$

where $A_{lm} = jk$ is the expansion coefficient of the (l, m) harmonic, and continuity on the surface $r = r'$ is imposed. Also, the coefficient A_{lm} can be determined by exploiting the discontinuity in the radial derivative. Hence, the desired spherical harmonic expansion of the Green's function is given by (A-3)

$$\begin{aligned} &\frac{e^{jk\left|\vec{r} - \vec{r}'\right|}}{4\pi\left|\vec{r} - \vec{r}'\right|} = jk \sum_{l=0}^{\infty} \begin{Bmatrix} j_l(kr) h_l^{(1)}(kr') & [r < r'] \\ j_l(kr') h_l^{(1)}(kr) & [r > r'] \end{Bmatrix} \sum_{m=-l}^{l} Y_{lm}(\theta, \phi) Y_{lm}^*(\theta', \phi') \\ &= jk \sum_{l=0}^{\infty} \begin{Bmatrix} j_l(kr) h_l^{(1)}(kr') & [r < r'] \\ j_l(kr') h_l^{(1)}(kr) & [r > r'] \end{Bmatrix} (2l+1) P_l(\cos\psi) \ \neg \ P_l(\cos\psi) = \frac{4\pi}{2l+1} \sum_{m=-l}^{l} Y_{lm}^*(\theta, \phi) Y_{lm}(\theta', \phi') \end{aligned} \tag{A-3}$$

Thus, it follows that (A-4)

$$e^{j\vec{k}\cdot\vec{r}} = \sum_{l=0}^{\infty} (j)^l (2l+1) j_l(kr) P_l(\cos\psi) \tag{A-4}$$

And illustrates a plane wave expansion as shown in (A-5),

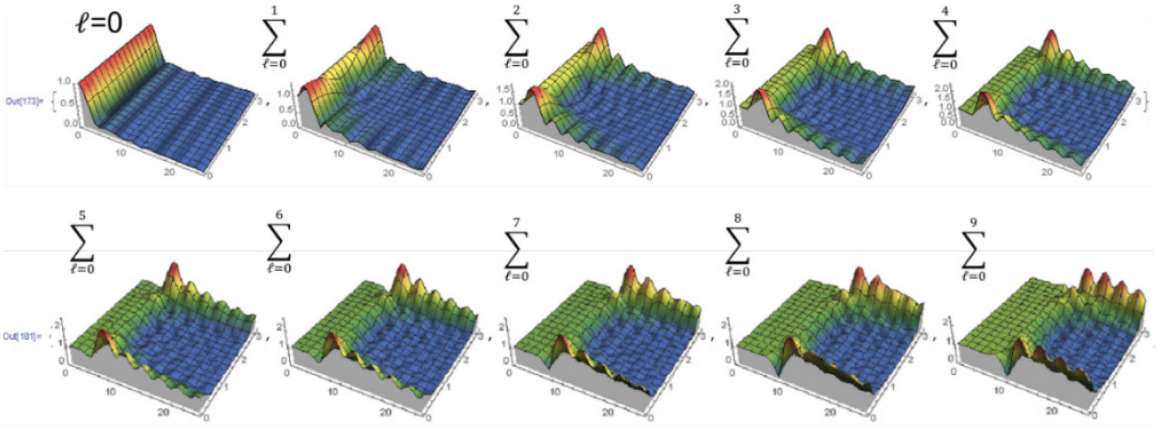

(A-5)

For a static field $k = 0$ (that is $\omega = 0$), and one indeed recovers the solution of the electrostatic multipole expansion (A-6)

$$\frac{1}{4\pi\left|\vec{r}-\vec{r}'\right|}=\begin{cases}\displaystyle\sum_{l=0}^{\infty}\sum_{m=-l}^{l}\frac{1}{2l+1}\frac{(r')^{l}}{r^{l+1}}Y_{lm}(\theta,\phi)Y_{lm}^{*}(\theta',\phi'),=\frac{1}{4\pi}\sum_{l=0}^{\infty}\frac{(r')^{l}}{r^{l+1}}P_{l}(\cos\psi) & r>r' \\ \displaystyle\sum_{l=0}^{\infty}\sum_{m=-l}^{l}\frac{1}{2l+1}\frac{r^{l}}{(r')^{l+1}}Y_{lm}(\theta,\phi)Y_{lm}^{*}(\theta',\phi'),=\frac{1}{4\pi}\sum_{l=0}^{\infty}\frac{r^{l}}{(r')^{l+1}}P_{l}(\cos\psi) & r<r'\end{cases} \qquad \text{(A-6)}$$

$$\neg\ P_{l}(\cos\psi)=\frac{4\pi}{2l+1}\sum_{m=-l}^{l}Y_{lm}^{*}(\theta,\phi)Y_{lm}(\theta',\phi')$$

APPENDIX B
FINITE SPHERICAL POINT SOURCE GREENS FUNCTION

A derivation of the Helmholtz equation is provided here for completeness and begins with

$$\frac{e^{jk|\vec{r}-\vec{r}'|}}{4\pi|\vec{r}-\vec{r}'|} = jk\sum_{l=0,\infty} j_l(kr_<)h_l^{(1)}(kr_>)\sum_{m=-l,+l} Y_{lm}^*(\theta',\phi')Y_{l,m}(\theta,\phi)$$
$$\frac{e^{-jk|\vec{r}-\vec{r}'|}}{|\vec{r}-\vec{r}'|} = jk\sum_{l=0}^{\infty} j_l(kr')h_l^{(1)}(kr)\sum_{m=-l}^{l} Y_l^m(\theta,\phi)Y_l^{m*}(\theta',\phi'),\ [r>r'] \qquad \text{B-1}$$
$$\neg\oint Y_{lm}^*(\theta,\phi)\frac{e^{jk|\vec{r}-\vec{r}'|}}{4\pi|\vec{r}-\vec{r}'|}d\Omega = jkh_l^{(1)}(kr)j_l(kr')Y_{lm}^*(\theta',\phi')$$

For a theoretical point source, the far-field distribution of the dominant term l=0 is (B-2)

$$\frac{e^{-jk|\vec{r}-\vec{r}'|}}{|\vec{r}-\vec{r}'|} = jk\sum_{l=0}^{\infty} j_l(kr')h_l(kr)\sum_{m=-l}^{l} Y_{lm}(\theta,\phi)Y_{lm}^*(\theta',\phi')$$
$$\approx jkj_0(kr')h_0(kr)Y_{00}(\theta,\phi)Y_{00}^*(\theta',\phi') = \frac{jk}{4\pi}\left(\frac{\sin(kr')}{kr'}\left(-j\frac{e^{jkr}}{kr}\right)\right) = \left.\frac{e^{jkr}}{4\pi r}\right|_{r'=0} \{\text{point source}\} \qquad \text{B-2}$$

Where integration provides over a spherical volume provides (B-3)

$$\frac{e^{-jkr}}{4\pi r}\int_0^{2\pi}\int_{-\pi}^{\pi}\sin\theta' d\theta' d\phi' = \frac{e^{-jkr}}{r} \qquad \text{B-3}$$

Differently, it's the far-field pattern for a uniformly distributed sphere provides (B-4)

$$\frac{e^{-jkr}}{4\pi r}\int_0^1\int_0^{2\pi}\int_{-\pi}^{\pi} j_0(kAr')r'^2\sin\theta' d\theta' d\phi' dr' = \frac{j_1(k)}{k}\frac{e^{-jkr}}{r} = Tinc(k)e^{-jkr} \qquad \text{B-4}$$

This result can also be shown as an integration of the sum of spherical waves as the spherical Hankel function of order zero h_0 represents the spherically symmetric wave field. Therefore, upon integrating the zeroth order mode, one obtains (B-5 resulting in B-6)

$$\frac{1}{V}\int_0^1\int_0^{2\pi}\int_0^{\pi} e^{-jkAr(\hat{n}\cdot\hat{r})} = \frac{1}{V}\sum_{l=0}^{\infty}\int_0^1\int_0^{2\pi}\int_0^{\pi}(j)^l(2l+1)j_l(kr)P_l(\cos\psi)r^2\sin\theta d\theta d\phi$$
$$V = f_{X,Y,Z}(x,y,z)\Big|_{A=1}^{n=0} = 3/4\pi, \qquad \cos\psi = (\hat{n}\cdot\hat{r}) \qquad \text{B-5}$$
$$\hat{n} = \hat{r}(\theta_0,\phi_0) = \sin(\theta_0)\cos(\phi_0)\hat{x} + \sin(\theta_0)\sin(\phi_0)\hat{y} + \cos(\theta_0)\hat{z}$$
$$\hat{r}(\theta,\phi) = \sin(\theta)\cos(\phi)\hat{x} + \sin(\theta)\sin(\phi)\hat{y} + \cos(\theta)\hat{z}$$

$$3Tinc(kA) = \frac{3}{4\pi}\int_0^1\int_0^{2\pi}\int_0^{\pi} e^{j\vec{k}\cdot\vec{r}} = \frac{3}{4\pi}\int_0^1\int_0^{2\pi}\int_0^{\pi}(j)^0(2l+1)j_0(kAr)P_0(\cos\psi)r^2\sin\theta d\theta d\phi \qquad \text{B-6}$$

This page is intentionally blank.

APPENDIX C
DIFFERENTIAL EQUATIONS SOLUTION WITH CONTOUR INTEGRALS

A solution to a linear differential equation can be formulated as (C-1)

$$Y(z)=\oint K(z,t)G(t)dt \tag{C-1}$$

A possible solution to the kernel $K(z,t)$ occurs if $K(z,t)=e^{zt}$, providing (C-2),

$$Y=\oint e^{zt}G(t)dt,\ Y'=\oint te^{zt}G(t)dt, \text{ and } Y''=\oint t^2e^{zt}G(t)dt. \tag{C-2}$$

Then integrating by parts, and assuming the initial and final points *P* are equal such that the integrand part is zero provides (C-3 to (C-8),

$$zY=\oint ae^{zt}G(t)dt=e^{zt}G(t)\Big|_P^P-\oint e^{zt}G'(t)dt=-\oint e^{zt}G'(t)dt \tag{C-3}$$

$$(2n+1)Y'=\oint(2n+1)te^{zt}G(t)dt \tag{C-4}$$

$$zY''=\oint zt^2e^{zt}G(t)dt=\oint\left(ze^{zt}\right)\left\{t^2G(t)\right\}dt \tag{C-5}$$

$$=e^{zt}\left\{t^2G(t)\right\}\Big|_P^P-\oint e^{zt}\left\{t^2G(t)\right\}'dt \tag{C-6}$$

$$=-\oint e^{zt}\left\{t^2G(t)\right\}'dt \tag{C-7}$$

$$zY''+(2n+1)Y'+zY=0=\oint e^{zt}\left[-G'(t)+(2n+1)tG(t)-\left\{t^2G(t)\right\}'dt\right] \tag{C-8}$$

Then choosing a solution $G(t)$ so that the integrand is zero, and solving $G(t)=A\left(t^2+1\right)^{n-1/2}$ where *A* is any constant with substitution of t=jx gives a solution(C-9 to (C-12),

$$-G'(t)+(2n+1)tG(t)-\left\{t^2G(t)\right\}'=0 \tag{C-9}$$

$$G'(t)=\frac{(2n-1)t}{t^2+1}G(t) \tag{C-10}$$

$$Y=A\oint e^{zt}\left(t^2+1\right)^{n-1/2}dt$$
$$Y=\frac{A}{2\pi j}\text{Res}\left\{e^{zt}\left(t^2+1\right)^{n-1/2}dt\right\} \tag{C-11}$$

$$Y = Aj\oint e^{jxt}\left(1-x^2\right)^{n-1/2}\,dx$$

$$Y = \frac{A}{2\pi}\mathrm{Res}\left\{e^{zt}\left(1-x^2\right)^{n-1/2}\,dx\right\}$$

C-12

INITIAL DISTRIBUTION

84310	Library	(1)
85300	Archive/Stock	(1)
75260	K, R. Buchanan	(1)
75260	S. Wheeland	(1)
75270	C. Flores-Molina	(1)
71760	T. Adeyemi	(1)
75260	D. Overturf	(1)
75260	O. Sternberg	(1)
75250	M. Rodriguez	(1)
75260	V. P. Acevedo	(1)
Penn State	G. H. Huff	(1)

Defense Technical Information Center
Fort Belvoir, VA 22060–6218 (1)

This page is intentionally blank.

REPORT DOCUMENTATION PAGE

Form Approved
OMB No. 0704-01-0188

PLEASE DO NOT RETURN YOUR FORM TO THE ABOVE ADDRESS.

1. REPORT DATE *(DD-MM-YYYY)*	2. REPORT TYPE	3. DATES COVERED *(From - To)*
November 2020	Technical Report	

4. TITLE AND SUBTITLE

Analysis and Discussion of Circularly Bound Random Antenna Array Distributions

5a. CONTRACT NUMBER

5b. GRANT NUMBER

5c. PROGRAM ELEMENT NUMBER

5d. PROJECT NUMBER

5e. TASK NUMBER

5f. WORK UNIT NUMBER

6. AUTHORS

Kristopher R. Buchanan, Oren Sternberg, Sara Wheeland, Michelle Rodriguez, Carlos Flores-Molina, Vincent P. Acevedo, Timi Adeyemi, Gregory H. Huff, Drew Overturf

NIWC Pacific

7. PERFORMING ORGANIZATION NAME(S) AND ADDRESS(ES)

NIWC Pacific
53560 Hull Street
San Diego, CA 92152–5001

8. PERFORMING ORGANIZATION REPORT NUMBER

TR 3218

9. SPONSORING/MONITORING AGENCY NAME(S) AND ADDRESS(ES)

The NIWC Pacific Naval Innovative Science and Engineering 53560 Hull Street San Diego, CA 92152–5001

US Army Research Office
6901 Farrel Rd,
Fort Rucker, AL 36362

10. SPONSOR/MONITOR'S ACRONYM(S)

NISE, ARO

11. SPONSOR/MONITOR'S REPORT NUMBER(S)

12. DISTRIBUTION/AVAILABILITY STATEMENT

DISTRIBUTION STATEMENT A: Approved for public release.

13. SUPPLEMENTARY NOTES

This is a work of the United States Government and therefore is not copyrighted. This work may be copied and disseminated without restriction. The research in this report is based upon work supported by, or in part by US Army Research Office under agreement number W911NF-09-1-0429 and NISE.

14. ABSTRACT

This report details a theoretical feasibility study to investigate the performance of circular antenna arrays. The radiation performance of circularly bound random arrays with various distributions are analyzed statistically to identify regions of deterministic, transitional, and random behavior. Isotropic radiators are preferred in this analysis in view of the fact that they provide relevant information on the fundamental beamforming behavior and can be applied to provide practical estimates and ideal limitations on the maximum peaking sidelobe located in the stochastically described 3 dB sidelobe region since this regime tends to behave non-deterministically. The mathematical process required for this analysis includes a statistical formulation of the array factor, including the mean, or expected value, and the variance. Rigorous analysis from prior works on random arrays provides the framework for this work and develops into accurate estimates of the maximum peaking sidelobe behavior in a volumetric scan region. Numerical results are included to illustrate scanning from zenith to meridian elevation angles to evaluate the theory and compare the behavior of both planar circular and volumetric spherical arrays.

15. SUBJECT TERMS

Circular antenna arrays; antenna arrays radiation performance of, statistical formulation of the array factor

16. SECURITY CLASSIFICATION OF:			17. LIMITATION OF ABSTRACT	18. NUMBER OF PAGES	19a. NAME OF RESPONSIBLE PERSON
a. REPORT	b. ABSTRACT	c. THIS PAGE			Kristopher Buchanan
U	U	U	SAR	102	19B. TELEPHONE NUMBER *(Include area code)* 619-553-6128

This page is intentionally blank.

This page is intentionally blank.

DISTRIBUTION STATEMENT A:
Approved for public release.

Naval Information Warfare Center Pacific (NIWC Pacific)
San Diego, CA 92152-5001